

OBSERVATIONAL STUDIES OF INTERACTING GALAXIES AND THE DEVELOPMENT OF
THE WIDE INTEGRAL FIELD INFRARED SPECTROGRAPH

by

Richard Chueh-Yi Chou

A thesis submitted in conformity with the requirements
for the degree of Doctor of Philosophy
Graduate Department of Astronomy and Astrophysics
University of Toronto

Copyright © 2013 by Richard Chueh-Yi Chou

Abstract

Observational Studies of Interacting Galaxies and the Development of the Wide Integral Field
Infrared Spectrograph

Richard Chueh-Yi Chou

Doctor of Philosophy

Graduate Department of Astronomy and Astrophysics

University of Toronto

2013

Interacting galaxies are thought to be the essential building blocks of elliptical galaxies under the hierarchical galaxy formation scenario. The goal of my dissertation is to broaden our understanding of galaxy merger evolution through both observational studies and instrument developments. Observationally, I approach the goal photometrically and spectroscopically. The photometric studies better constrain the number density evolution of wet and dry mergers through five CFHTLS broad band photometry up to $z \sim 1$. Meanwhile, by comparing the merger and elliptical galaxy mass density function, I discovered that the most massive mergers are not all formed via merging processes, unless the merging timescale is much longer than the expected value. Spectroscopically, the kinematic properties of close pair galaxies were studied to understand how star formation were quenched at $z \sim 0.5$. I discovered that the number of red-red pairs are rare, which does not support the gravitational quenching mechanism suggested by the hot halo model. In instrumentation, one efficient way to study galaxy mergers is to use the integral field spectroscopic technique, capitalizing its intrinsic capability of obtaining 2-D spectra effectively. However, the currently available integral field spectrographs are inadequate to provide the required combination of integral field size and spectral resolution for merger studies. I, therefore, have developed two optical designs of a wide integral field infrared spectrograph (WIFIS), which I call WIFIS1 and WIFIS2, to satisfy the requirements of merger studies. Both the designs provide an integral field of $12'' \times 5''$ on 10-m telescopes (or equivalently $52'' \times 20''$ on 2.3-m telescopes). WIFIS1 delivers spectral resolving powers of 5,500 covering each of JHK bands in a single exposure; WIFIS2 does a lower power of 3,000 focusing on a shorter wavebands of zJ and H bands. All the WIFIS2 optical components have

either been or being fabricated, and some of the components have been characterized in the laboratory, including its integral field unit, gratings, and mirrors. The expected completion of WIFIS based on WIFIS2 is 2013 summer, which will be followed by WIFIS1-based spectrograph in a few years.

Dedication

To my Parents and my Wife

For your warm support

Acknowledgements

This PhD marathon has almost come to an end. It has been a six-year long pursuit that has taken the efforts, guidance and support of many people. First of all, I would like to thank my supervisors Bob Abraham and Dae-Sik Moon for their guidance, without them I could not have made it this far. I would like to thank Bob for his inspirations and encouragement, it really has been a nice experience to work with you. I will always remember the time in the summer of 2008 that we worked together (with Ivana) on the preparation of the qualifier exam. That was one of the happiest periods in my PhD life. I would also like to thank Dae-Sik for continuously pushing me forward on the optical designs that at the beginning I thought I could never complete.

Besides my supervisors, I also would like to thank Carrie Bridge and Suresh Sivanandam for being my collaborators. I would like to thank Carrie for supporting me in the two merger papers we worked on together. I have learned a lot from you, including how to conduct observations, reduce data and write papers, etc. Suresh, I owe you a big thank for helping me in instrument developments. I have learned basic optics, experimental techniques and trouble shooting from you. I really enjoyed the time that I worked with you on developing WIFIS.

Also I need to thank all my friends for supporting me both academically and emotionally. I appreciate the moments we worked on assignments, group discussions, arguing questions and sharing stories.

In the end I would like to thanks my parents Shu-Chi Lin and Jiun-Fung Chou and my wife Yu-Min Lee. You are the solid background behind me, such that I never had to worry while pursuing my PhD degree. Thank you all and I love you.

Contents

1	Introduction	14
1.1	Scenarios for Galaxy Formation	15
1.1.1	Evolution of Dark Matter Halos	15
1.1.2	Evolution of the Baryonic Component of Galaxies – “Gastrophysical” Aspects of Galaxy Evolution	17
1.1.3	Migration of Galaxies on the Color Magnitude Diagram: Quenching Mechanisms for Star Formation	18
1.1.4	Quenching Mechanisms	20
1.2	The Merger Scenario in Galaxy formation	21
1.2.1	The Growth of Dark Matter Halos & the Merger Tree	21
1.2.2	The Evolution of Stellar Populations: Wet & Dry Mergers	23
1.2.3	Scientific Goals of this Thesis	23
1.3	Galaxy Mergers in Observational Astronomy	25
1.3.1	Merger Rate Evolution	25
1.3.2	Merger Selection Methods	27
1.4	Observations: The CFHTLS - Deep Survey	33
1.4.1	Survey Overview	33
1.4.2	CFHTLS–Deep Survey	34
1.5	Integral Field Spectroscopy	35
1.5.1	NIR Integral Field Spectroscopy	36
1.5.2	Integral Field Units	38
1.5.3	Scientific Applications	39

1.6	Organization of this Thesis	40
2	The Space Density Evolution of Wet and Dry Mergers in the Canada-France-Hawaii Telescope Legacy Survey	43
2.1	INTRODUCTION	43
2.2	OBSERVATIONS	46
2.2.1	Data	46
2.2.2	Merger identifications	46
2.2.3	Galaxy properties	48
2.3	Classification of Wet and Dry Mergers	48
2.3.1	Method I: integrated colors	49
2.3.2	Method II: spatially resolved colors	50
2.4	RESULTS	50
2.4.1	Merger Fractions	50
2.4.2	The Space Density of Merging Galaxies	54
2.4.3	The Role of Stellar Mass	55
2.5	DISCUSSION	55
2.6	CONCLUSION	62
3	A Close-pair Analysis of Damp Mergers at Intermediate Redshifts	63
3.1	INTRODUCTION	63
3.2	OBSERVATIONS	66
3.2.1	Photometry and galaxy Properties	66
3.2.2	Spectroscopy of the photometric sample	67
3.2.3	Color classification	71
3.2.4	Spectroscopic redshifts	72
3.3	RESULTS	75
3.4	DISCUSSION	81
3.4.1	Abundance of physical pairs	81
3.4.2	Comparison with DEEP2 and VVDS Surveys	82

3.4.3	Damp vs. Dry Mergers	83
3.4.4	Implications for the Hot Halo Model	85
3.5	CONCLUSIONS	86
4	Optical Designs of the Wide Integral Field Infrared Spectrograph	87
4.1	INTRODUCTION	87
4.2	WIFIS Optical Designs and Systems	89
4.2.1	Re-imaging Unit and Integral Field Unit	89
4.2.2	Collimator, Dispersing Unit and Spectrograph Camera	96
4.3	Nominal Performance of WIFIS1 and WIFIS2	98
4.3.1	Field of View	98
4.3.2	Spectral Resolving Power	98
4.3.3	Spectral Coverage	102
4.4	Expected System Performance of WIFIS1 and WIFIS2	102
4.4.1	Design Tolerance Analyses	102
4.4.2	Thermal Environmental Effects in WIFIS Designs	108
4.5	Predicted On-sky Characteristics	111
4.6	Comparisons between WIFIS1 and WIFIS2	114
4.7	Summary and Conclusion	116
5	Laboratorial Characterizations of WIFIS Integral Field Unit	117
5.1	INTRODUCTION	117
5.2	FISICA Characterization Configuration	117
5.2.1	Optical System for FISICA Characterization	117
5.2.2	Laboratorial FISICA Characterization Setup	120
5.3	Results of Characterizations	124
5.3.1	Mapping Relation	125
5.3.2	Magnification of FISICA	126
5.3.3	Image Quality of FISICA	126
5.4	Summary and Conclusion	129

6	Conclusions & Future Prospects	130
6.1	Thesis Summary	130
6.2	Future Work	132
6.2.1	Completion of WIFIS	132
6.2.2	A 2-D NIR Spectroscopic Survey of Medium-Redshift Merging Galaxies .	133
	Bibliography	136

List of Tables

1.1	CFHTLS-Deep Survey Field Locations	35
1.2	CFHTLS-Deep Survey: Magnitude Limits	35
3.1	Redshift confidence classes	73
3.2	Summary of three types of close pairs selected using different criteria.	79
4.1	Summary of important specifications of IFSs in NIR on large telescopes.	89
4.2	Summary of important parameters of three diffraction gratings used in WIFIS.	96
4.3	Summary of important system parameters and the theoretically calculated spectral resolving powers	100
4.4	Expected spectral coverage for WIFIS1 and WIFIS2.	102
4.5	Acceptable tolerances in WIFIS optical designs	103
4.6	Summary of tolerance analyses results for WIFIS1 and WIFIS2	104
4.7	Expected spectral resolving power for WIFIS1 and WIFIS2.	108
4.8	HAWAII 2RG Detector Parameters	112
5.1	Centers and 3σ radii of focused and defocused pinhole images	123

List of Figures

1.1	Bimodal galaxy distribution on the color magnitude diagram	16
1.2	Streams in three dimensions	19
1.3	Time sequence of one typical merger simulations taken from Hopkins et al. (2006a) with $V_{\text{vir}} < 160 \text{ km s}^{-1}$ and initial gas fraction 20%.	22
1.4	An example of merger trees	24
1.5	Merger rate as a function of redshift in units of mergers $\text{galaxy}^{-1} \text{ Gyr}^{-1}$, taken from (Bridge et al., 2010).	26
1.6	Left panel: Projected physical separation r_p versus velocity difference δv for 225 close pairs taken from Figure 5 in Patton et al. (2000). Right panel: Mosaic of images for 16 close pairs that satisfy the selection criteria	28
1.7	Graphical representation of how the three parameters, asymmetry (A), clumpiness (S), and concentration (C) are measured.	30
1.8	Geometric interpretation of the Gini coefficient based on the Lorenz curve. The x-axis corresponds to the quantile of the distribution, and the y-axis corresponds to the cumulative proportion. The line of equality is shown as the diagonal line, which represents a perfectly equal distribution. In this figure a schematic Lorenz curve divides the area below the line of equality into two areas, A and B. The Gini coefficient corresponds to the ratio of area A to the total area under the equality line A+B. The greater the deviation of a measured Lorenz curve from the line of equality, the greater the inequality.	32
1.9	Top panel: variation of angular size of an object with a diameter of 50 kpc as a function of redshift. Bottom panel: a montage of i' band image of four medium redshift galaxy mergers taken from CFHTLS.	37
1.10	Three main IFU techniques commonly used in integral field spectroscopy.	39
1.11	Examples of potential scientific applications for the proposed NIR IFS.	41

2.1	A montage of i' -band image of six typical galaxy mergers.	45
2.2	Colors of ~ 2200 field galaxies in the CFHTLS survey	47
2.3	Merger fractions computed using two different methods	51
2.4	Co-moving space densities of wet and dry mergers	52
2.5	Mass density function of mergers in two redshift bins and in wet/dry mergers . .	54
2.6	A comparison of the evolving merger rate density with previous works	56
2.7	Comparison of merger fractions with two different merger selection methods . . .	57
2.8	A comparison of the stellar mass density function for mergers in the present sam- ple with the corresponding stellar mass density function for early-type galaxies presented in Bundy et al. (2005)	58
3.1	Rest frame $g' - i'$ color versus stellar mass for close pair galaxies in D1, D2 and D4 fields.	68
3.2	Spatial selection function of close pairs	70
3.3	Successful redshift ratio versus i' -band apparent magnitude.	74
3.4	Diagram of separation versus velocity difference for close pair galaxies.	76
3.5	Diagram of separation versus velocity difference for close pair galaxies using different stellar to total halo mass ratios taken from Leauthaud et al. (2011). . .	79
4.1	An optical color composite image of a nearby major merger NGC 2623 taken by the Hubble Space Telescope	90
4.2	Etendue times throughput versus spectral resolving powers for major IFSs on large telescopes	91
4.3	Optical layout of two WIFIS designs	92
4.4	Optical layout of the integral field unit FISICA	93
4.5	Fabricated mirror arrays for FISICA	94
4.6	Spot diagrams and encircled energy diagram for WIFIS1 design	99
4.7	An example of degraded projected slit image	101
4.8	Spectral coverage of WIFIS1 and 2 designs	103
4.9	Nominal and average Monte Carlo performance in spot radius as a function of wavelength	106

4.10	Nominal and as-built performance in spot radius as a function of wavelength . . .	107
4.11	Spot diagram at $\lambda = 1.1 \mu\text{m}$ with the environment temperature $T = 30^\circ\text{Celsius}$	109
4.12	Expected photon flux per pixel from thermal radiation as a function of the cut-off wavelength of the thermal blocking filter.	110
4.13	Expected point source continuum sensitivity at the GTC and the Bok telescopes	113
5.1	Block diagram of the FISICA characterization test setup.	118
5.2	Zemax simulation of the illumination assembly used in FISICA characterization test	119
5.3	Performance and aberrations of the illumination assembly	120
5.4	Configuration of the FISICA characterization setup	121
5.5	A schematic diagram illustrating how to measure the marginal ray angle θ	122
5.6	Actual focused and defocused pinhole images	123
5.7	Image of the input integral field of FISICA provided by the illumination assembly	124
5.8	The expected mapping relation between the input integral field and the output pseudo long-slit of FISICA	125
5.9	An example of a single slicer mirror being illuminated	127
5.10	FWHM and EE80 width along the pseudo long-slit	128
6.1	Resolved pixel-by-pixel colors of one typical galaxy merger in our CFHTLS sample	134

Chapter 1

Introduction

The development of contemporary astronomy has broadened the frontier of our knowledge. We realized that the Earth is not the center of the Universe, nor the Sun. The solar system we live in is located on the Orion arm of the Milky Way and ~ 8.3 kpc away from the Galactic center (Reid, 1993; Ghez et al., 2008; Gillessen et al., 2009). Moreover, there exist billions of galaxies in the Universe and they are known to be the fundamental units of the Universe. The striking image from the Hubble Deep Field Survey (Williams et al., 1996) reveals the diversity in galaxy morphologies in the local and early Universe. Back in early twentieth century, Edwin Hubble proposed his famous ‘Hubble tuning fork’ or Hubble’s sequence based on observations of nearby luminous galaxies (Hubble, 1926, 1936). Hubble’s classification mainly divides galaxies into four morphological categories: elliptical (E), lenticular (S0), spiral and irregular (Irr) galaxies. For lenticular and spiral galaxies, there are subclasses associated with normal and barred structure (e.g., normal spiral or barred lenticular galaxies). Although almost 95% of nearby luminous galaxies fall into the Hubble’s sequence (van den Bergh, 1999), there are some additional classification types such as rings, ovals (de Vaucouleurs et al., 1976a), under-luminous dwarfs and super-luminous cDs (Morgan, 1971) galaxies that are not incorporated into Hubble’s system.

Hubble’s main insight was that galaxies can be broadly assigned into two types. One type are known as early type galaxies that have elliptical or spherical morphology. The other type are late type galaxies that have clear spiral arm structures and well defined galactic disks. Although this morphological classification was based on eyeball examination and limited galaxy samples in its early phase, new results based on systematic and statistic analyses derived from large galaxy surveys also support this morphological bimodality (Driver et al., 2006; Coppa et al., 2011). This bimodality not only exists in morphological distinctions, but also presents in other aspects such as optical colors (Strateva et al., 2001; Ball et al., 2006) and spectral indices

(Kauffmann et al., 2003; Balogh et al., 2004). The reader is referred to Blanton et al. (2003) for an excellent review on the bimodal distributions of various galaxy properties. Generally speaking, if dust extinction is neglected, early type galaxies in the local Universe look very red. Their Spectral Energy Distributions (SED) have prominent stellar absorption features and lack emission lines, which is an indication of low star formation activity. In addition, early type galaxies have relatively low visible wavelength color dispersion compared with late type galaxies. On the color magnitude diagram, early type galaxies group together and form a ‘red sequence’ (Visvanathan & Griersmith, 1977). On the other hand, late type galaxies look bluer and their SED have prominent emission features, which indicate active on-going star formation activities. Although their visible wavelength colors are less coherent, the distribution on the color magnitude diagram can be used to define a ‘blue cloud’ (Chester & Roberts, 1964; Visvanathan, 1981; Tully et al., 1982).

The division into the red sequence and blue cloud is shown in Figure 1.1, taken from the well known paper by Baldry et al. (2004). This bimodal galaxy distribution on the color magnitude diagram is shown in Figure 1.1. Moreover, this bimodal distribution on the color magnitude diagram not only exists in the local Universe, but it also applies to galaxies at higher redshifts. Bell et al. (2004) and Willmer et al. (2006) utilized rest-frame optical colors to define a red sequence from galaxy surveys and discovered that the bimodality exists out to a redshift of unity. In recent years, deep galaxy surveys reveal that this bimodal distribution possibly extends up to $z = 2$ or beyond (Pozzetti et al., 2010; Conselice et al., 2011). However, the origin and the evolution of this color bimodality are largely unknown. The traditional view of red systems is that they are early-type galaxies which form monolithically at high redshifts (Eggen et al., 1962) though in modern theories of galaxy evolution ‘nurture’ plays as big a role as ‘nature’, and evolution is driven by several physical mechanisms, including galaxy-galaxy interactions (Blumenthal et al., 1984; Di Matteo et al., 2005; Hopkins et al., 2010; Lambas et al., 2012), infalling cold gas (Dekel & Birnboim, 2006; Dekel et al., 2009; Kereš et al., 2009; Bournaud et al., 2011), and hot halo gas quenching (Birnboim & Dekel, 2003; Birnboim et al., 2007; Panuzzo et al., 2011; Gabor & Davé, 2012).

1.1 Scenarios for Galaxy Formation

1.1.1 Evolution of Dark Matter Halos

The current paradigm for the formation of large-scale structure and galaxy formation is based on the Cold Dark Matter (CDM) model (Blumenthal et al., 1984; Davis et al., 1985). This model describes a Universe dominated by ‘cold’ dark matter particles which decoupled relatively early

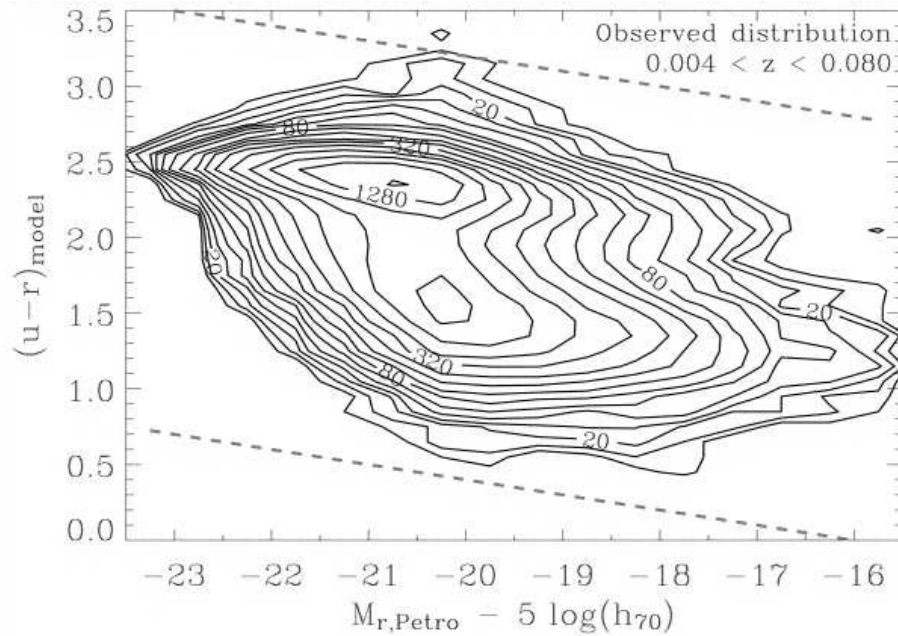


Figure 1.1 Bimodal galaxy distribution on the color magnitude diagram, taken from Baldry et al. (2004). The sample comprises of 66,864 galaxies observed by the Sloan Digital Sky Survey (York et al., 2000; Stoughton et al., 2002). The contours are determined by galaxy number counts in $0.1 \text{ color} \times 0.5 \text{ mag}$ bins. The contour levels are on a logarithmic scale, starting at ten and doubling every two contours. The dashed lines represent the limits used in the double-Gaussian fitting.

after they had already become non-relativistic at $t \sim 10^{-9}$ s after the Big Bang, when the mass within the horizon was very small (much smaller than one solar mass). As soon as the dark matter particles became non-relativistic, free streaming was unimportant and the dark matter perturbations on all scales of astrophysical interest survived from the early Universe. After the recombination era ($z \sim 1100$), the baryonic perturbations on all scales soon were regenerated by collapse into the dark matter perturbations. The Jeans mass M_J right after the recombination era is roughly $7 \times 10^6 M_\odot$, and is of the same order as the mass of globular clusters. Because of the cold dark matter, perturbations of all scales were preserved, especially small scale perturbations. This makes the large structure and galaxy formation a ‘bottom up’ or ‘hierarchical’ process, which means small structures formed first and clustered subsequently to form galaxies and clusters. This prediction from the CDM model is remarkably successful in accounting for the power spectrum of spatial distribution of galaxies and for the spectrum of fluctuations in the cosmic microwave background radiation. Furthermore, because of the preservation of small perturbations, stars and content of galaxies can begin to evolve soon after the end of recombination era. This leads to the re-ionization of the intergalactic medium and early chemical enrichment of gas by the end products of the first generation stars, although the mechanisms by which these processes occur are not presently understood.

Although the CDM model has achieved a remarkable success in describing the formation of large-scale structure and dark matter halo of galaxies, most observables accessible to astronomers are based on the study of the visible part of galaxies (e.g., stars and gas), which are not the main focus of the theory. The “gastrophysical” aspect of galaxy formation are poorly understood.

1.1.2 Evolution of the Baryonic Component of Galaxies – “Gastrophysical” Aspects of Galaxy Evolution

The traditional view of galaxy formation is the so called ‘monolithic collapse’ scenario of Eggen et al. (1962). This pioneering work studied the motions of high velocity stars and discovered that, as metal abundance decreases, orbital energies and eccentricities of stars increases while their orbital angular momenta decrease. Eggen et al. (1962) inferred that metal-poor stars reside in a halo that was created during the rapid collapse of a relatively uniform, isolated protogalactic cloud shortly after it decoupled from the universal expansion. This paper is widely viewed as advocating a smooth monolithic collapse of the protocloud with a timescale of order 10^8 years and its publication triggered numerous of follow up studies.

Recent theoretical work based on observations of massive star forming galaxies (SFGs) at high redshifts ($z > 1$) propose a different gas collapse scenario, which in some ways seems to contradict to the ‘bottom up’ galaxy formation scenario. The observations show that these high

redshift SFGs have stellar masses $\sim 10^{11} M_{\odot}$ and high star formation rate of $\sim 100 M_{\odot}$ per year (Genzel et al., 2006; Förster Schreiber et al., 2006; Elmegreen et al., 2007; Genzel et al., 2008; Stark et al., 2008), which is roughly 100 times higher than the present Galactic star formation rate of $\sim 1 M_{\odot}$ per year (Robitaille & Whitney, 2010). Because of the intense star formation rates, these SFGs are thought to be the main star producers in the cosmic star formation history (Lilly et al., 1996; Madau et al., 1998; Hopkins & Beacom, 2006). However, results from photometric and kinematics observations show that these SFGs might have clumpy but well defined disks similar to our local neighbor spiral galaxies. A unique feature which distinguishes them from low redshift galaxies is that their disks tend to break into several giant clumps. These clumps have a size of ~ 1 kpc and a mass up to a few times $10^9 M_{\odot}$ (Elmegreen et al., 2004; Förster Schreiber et al., 2006; Genzel et al., 2008). The origin of these clumps is unclear and it is difficult to produce such clumps while maintaining a rotating disk through galaxy major mergers because major mergers tend to develop spheroidal bulges rather than flat disks.

To address this issue (and others), a gas accretion scenario called ‘cold flow’ accretion has been proposed to explain the formation of massive SFGs at high redshifts (Dekel et al., 2009; Bouché et al., 2010; Bournaud et al., 2011). The idea is that cold gas accretes onto unstable dense gas-rich disks through streams from the inter-galactic medium. Instability with high turbulence and giant clumps, each of a few percent of the disk mass, is self-regulated by gravitational interactions within the disk. The clumps may coalesce into a bulge-like structure in ≤ 10 dynamical times or ≤ 0.5 Gyr. The cold flow constantly replenishes the draining disk and prolongs the clumpy phase of the disk to a few billion years. Intense star formation is triggered during this clumpy phase and each clump converts into stars in a relatively short period of ~ 0.5 Gyr. While the clumps evolve dissipatively into a spheroidal bulge, the star forming disk is extended because of the steady supply of fresh cold gas from the cosmological stream. The formation and evolution of passive early type galaxies could also be explained by the same scenario but with more clumpy streams. Massive and clumpy external streams merge to form a bulge and stir up the disk kinematics to stabilize the disk and suppress the in situ star formation and clumps. It is claimed that the cold flow accretion could reproduce the galaxy color bimodality up to $z \sim 3$ (Dekel et al., 2009) and other important relationships such as the Tully-Fisher relation (Tully & Fisher, 1977).

1.1.3 Migration of Galaxies on the Color Magnitude Diagram: Quenching Mechanisms for Star Formation

There is now a considerable body of evidence suggesting that the red sequence is populated by galaxies which have somehow ‘migrated’ there from the blue cloud (Bundy et al., 2010; Shapiro

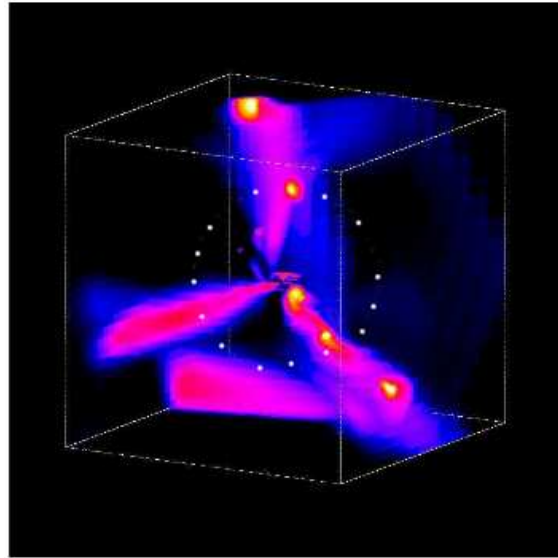


Figure 1.2 Streams in three dimensions, taken from Dekel et al. (2009). The map shows radial fluxes for a galaxy in a box with the length of each side equals to 320 kpc. The colors refer to inflow rate per solid angle of point-like tracers at the centers of cubic-grid cells. The white dot circle marks the halo virial radius. The three fairly radial streams that possess a feature of cosmic web seems to be generic in the massive haloes at high redshifts. Two of the streams show gas clumps of mass on the order of one-tenth of the central galaxy, but most of the stream mass is smoother (Figure 10 in the supplement information, Dekel et al. (2009)). The clumps ($M \gtrsim 10^{10} M_{\odot}$), which involve about one-third of the incoming mass, are also gas rich - in this simulation only 30% of their baryons turn into stars before they merge with the central galaxy.

et al., 2010; Hughes & Cortese, 2009; Martin et al., 2007). Observations have shown that the total stellar mass of red massive galaxies ($M_* \geq 10^{11} M_\odot$) has grown by a factor of two since redshift $z \sim 1$, while that of blue disc galaxies remains more or less the same (Bell et al., 2004; Faber et al., 2007; Abraham et al., 2007). Furthermore, Brammer et al. (2011) show that this mass growth trend can be traced up to $z \sim 2.2$. There is some evidence suggesting that the (visible wavelength) color transformation timescale for migration of a blue galaxy onto the red sequence is fast, ~ 1 Gyr (Bell et al., 2004; Blanton, 2006). Assuming the average gas to total mass ratio of late type galaxies is $\sim 15\%$ (Rubin et al., 1985) and a typical constant star formation rate of a few solar masses per year, it is difficult to consume all the gas content in blue galaxies within a timescale of 1 Gyr. In addition, as mentioned above, cold flows from the intergalactic medium (IGM) can also channel new and fresh gas into galactic halos, continuously feeding galaxies (Brooks et al., 2009; Kereš et al., 2009). Thus, to move a galaxy from the blue cloud onto the red sequence the star formation must be sharply cut off or quenched, instead of being stopped simply by a depleted supply of cold gas. Most mechanisms invoked for quenching star formation involve various forms of feedback which couples star-formation in disks to hot gas in galactic halos.

1.1.4 Quenching Mechanisms

One well-studied mechanism for halting star-formation is the hot halo quenching model, which suggests that as gas falls into galactic dark matter halos it is heated by virial shocks. If the mass of a dark matter halo exceeds $\sim 10^{12} M_\odot$, the rate of gravitational heating by shocks is greater than that of radiative cooling. Hence, a hot virialized gas halo is formed near the virial radius. This hot halo shocks and heats up the in-falling cold gas immediately, which prevents the gas from collapsing and forming new stars (Birnboim & Dekel, 2003; Birnboim et al., 2007). The hot halo quenching model alone cannot quench all star formation within a galaxy since some in-falling gas will still cool down and form stars in the center of the galaxy, but this model provides a simple explanation for the mass-dependent bimodal galaxy distribution (Dekel & Birnboim, 2006; Cattaneo et al., 2006).

Another interesting mechanism for halting star-formation in galaxies is major merger quenching. By definition major mergers refer to galaxy mergers that possess two or more interacting galaxies of roughly comparable stellar mass. In this picture, major merger quenching originates from strong stellar winds generated by the intensely triggered star formations that expel and/or heat the ISM through shocks or feedback from supernovae (Cox et al., 2006; Ceverino & Klypin, 2009). Stellar feedback from supernovae is probably not sufficient to quench the star formation of the entire galaxy (Springel et al., 2005), so some additional energy source is

probably required to supplement this quenching process.

Some semi-analytical models integrate these various ideas into a hybrid picture in which a central super massive black hole (SMBH) is an additional energy supply. In the hot halo quenching model, the in-falling cold gas could accrete onto the SMBH and trigger low luminosity AGN, which is also known as the ‘radio’ mode of the quenching process (Croton et al., 2006; Hopkins & Hernquist, 2006). Similarly, major mergers can induce more violent material accretion and generate large amounts of energy feedback, which is known as the ‘quasar’ mode of the quenching process (see Figure 1.3 for an example). Both energetic feedback mechanisms involving the central SMBH could effectively expel or heat the surrounding gas disc and further quench the star formation activities (Hopkins et al., 2006b,a).

1.2 The Merger Scenario in Galaxy formation

Galaxy mergers have fascinated astronomers for decades and are known to play an important role in galaxy evolution. When two galaxies interact with each other, strong relaxation processes destroy rotating discs and turn late type galaxies into early type ones (Toomre & Toomre, 1972; Tinsley & Larson, 1977; Schweizer, 1982; Genzel et al., 2001). In addition, strong turbulence increases the instability within molecular clouds and enhances star formation activities (Kennicutt et al., 1987; Xu & Sulentic, 1991). In some cases, galaxy mergers may trigger extreme starburst and even active galactic nuclei because of large amount of fresh gas supply from one galaxy to the center of the other one (Sanders et al., 1988; Sanders & Mirabel, 1996; Dasyra et al., 2006). However, the major mergers modelled by most early papers are the most spectacular examples of a process that encompasses a large range of galaxy masses and interaction strengths.

1.2.1 The Growth of Dark Matter Halos & the Merger Tree

With the success of the CDM model in reproducing features of galaxy clusters or super clusters, Kauffmann et al. (1993) constructed a ‘merger tree’ that uses a Monte Carlo method to express the merging history of dark matter haloes by considering the progenitors of each halo every time a merger occurs. Figure 1.4 shows an example of merger tree taken from Figure 1 of Stewart et al. (2008). This merger tree model correctly reproduces the observed trends in luminosity, color, gas content and morphology of galaxies (Kauffmann, 1996; Somerville et al., 2001; Khochfar & Burkert, 2003). However, observationally, the details of when and how galaxy mergers happen and the outcomes of the mergers remain unclear. Perhaps, the simplest question

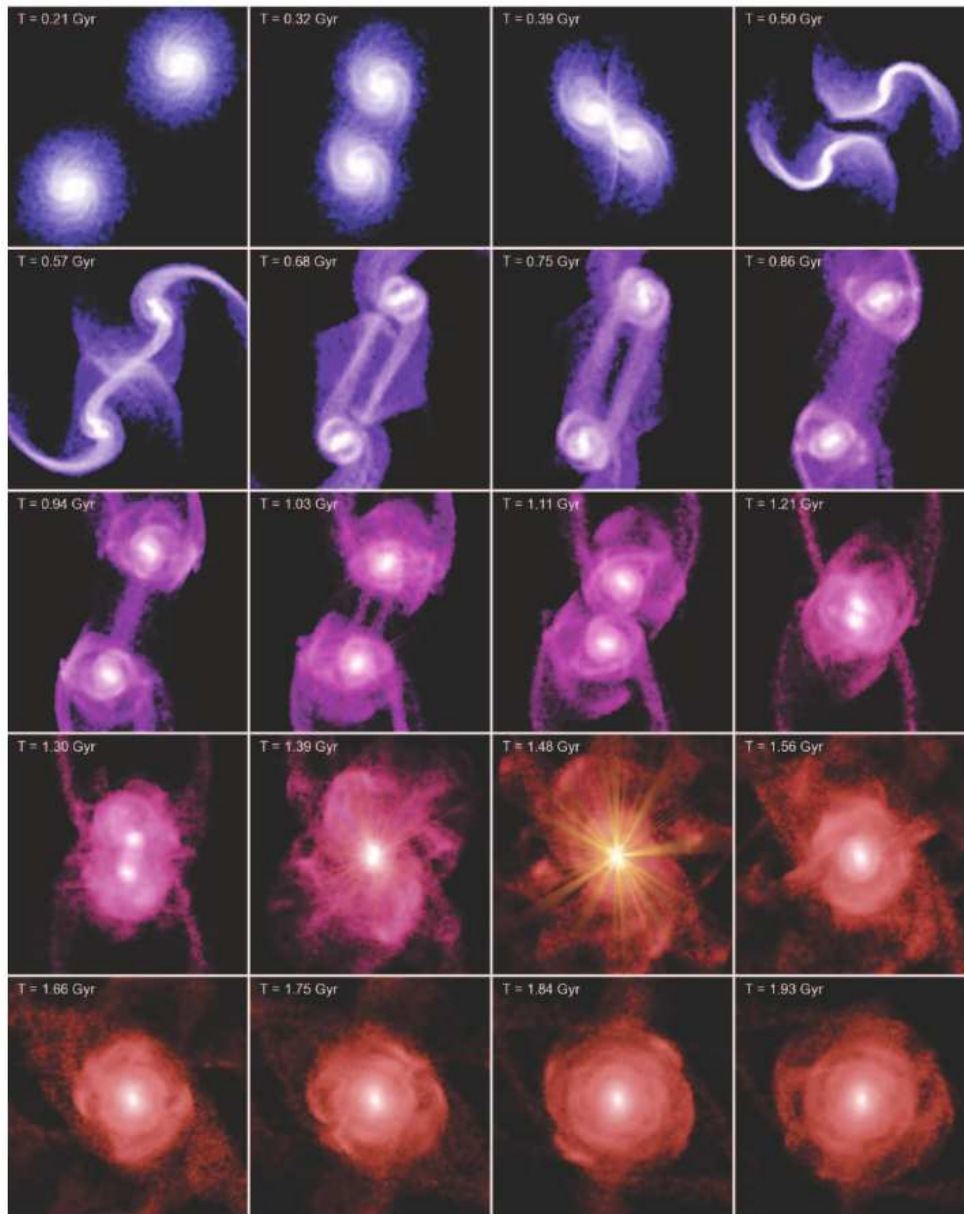


Figure 1.3 Time sequence of one typical merger simulations taken from Hopkins et al. (2006a) with $V_{\text{vir}} < 160 \text{ km s}^{-1}$ and initial gas fraction 20%. Each panel is $80h^{-1}$ kpc on a side and shows the simulation time in the upper left corner. Brightness of individual pixels gives the logarithm of the projected stellar mass density, while color hue indicates the baryonic gas fraction, from 20% (blue) to less than 5% (red). At $T = 1.03, 1.39,$ and 1.48 Gyr, the central black hole could be seen as an optical quasar. The nuclear point source provides a representation of the relative luminosities of stars and the quasar at these times.

to ask is whether the product of the merger is a blue system or a red system, and attempting to answer this question is an important goal of this thesis.

1.2.2 The Evolution of Stellar Populations: Wet & Dry Mergers

As mentioned above, galaxies tend to show bimodal distributions on the color magnitude diagram. Blue cloud galaxies appear to migrate to the red sequence through some form of star formation quenching mechanism. However, it is not clear when and how blue galaxies ceased their star formation and undertook this migration. It is clearly important to distinguish between mergers that result in significant star-formation (‘wet mergers’) and those which merely re-organize existing stellar populations (‘dry mergers’). Wet mergers are typically associated with gas-rich systems that trigger star formation (Barton et al., 2000; Bridge et al., 2007; Lin et al., 2007; Overzier et al., 2008; Di Matteo et al., 2008; Rodríguez Zaurín et al., 2010), cause quasar activity (Hopkins et al., 2006b) and turn disk galaxies into elliptical galaxies (Toomre & Toomre, 1972). Dry mergers (van Dokkum, 2005; Bell et al., 2006) may be responsible for the assembly of massive ($M_{\text{stellar}} \gtrsim 10^{11} M_{\odot}$) red galaxies which are observed in surprisingly high abundance at $z \sim 1$. However, the relative importance of wet and dry mergers in the formation of red sequence galaxies is still not clear (Bell et al., 2007; Brown et al., 2007; Bundy et al., 2009; Faber et al., 2007; Lin et al., 2008; Scarlata et al., 2007), and it is of interest to determine whether wet and dry mergers exhibit similar evolutionary trends as a function of cosmic epoch.

1.2.3 Scientific Goals of this Thesis

The central goal of this thesis is to chart the differential merging history of color-selected subclasses of merging galaxies, using visually classified galaxy merger sample obtained from the Deep component of the Canada-France-Hawaii Telescope Legacy Survey (CFHTLS-Deep, see Section 1.4.2 for more information). In addition, I aim to better constrain the number density of dry mergers at early merging stages by selecting close pair mergers from the CFHTLS, and to test the hot halo quenching model. Before describing the progress I have made in answering these questions, I will sketch out an overview of what is known regarding the evolution of the merger rate, and outline the standard techniques used to identify mergers.

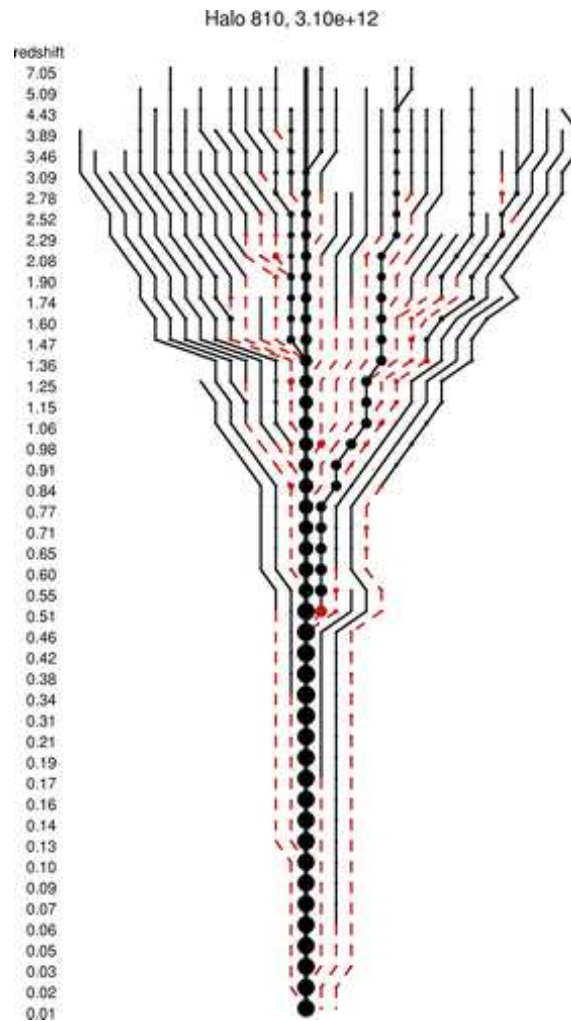


Figure 1.4 An example of merger trees, taken from Stewart et al. (2008). This merger tree is for galaxies with mass of halos equal to $M_0 \sim 10^{12.5} h^{-1} M_\odot$. A ‘typical’ merger history, with a merger of mass $\sim 0.1 M_0$ at $z = 0.51$. Time progresses downward, with the redshift z printed on the left-hand side. The bold, vertical line at the center corresponds to the main progenitor, with filled circles proportional to the radius of each halo. The minimum mass halo shown in this diagram has $m = 10^{9.9} h^{-1} M_\odot$. Solid (black) and dashed (red) lines and circles correspond to isolated field halos, or subhalos, respectively. The dashed (red) lines which do not merger with the main progenitor represent surviving subhalos at $z = 0$.

1.3 Galaxy Mergers in Observational Astronomy

1.3.1 Merger Rate Evolution

One straightforward way to understand galaxy merger evolution is to study *the evolution in the galaxy merger rate*. The galaxy merger rate is defined by the merger fraction per merging timescale within a particular redshift bin:

$$\text{Merger Rate} \equiv \frac{N_{\text{merger}}}{N_{\text{tot}} T_{\text{merger}}} \quad (1.1)$$

where N_{tot} and N_{merger} represent the total number of galaxies and mergers in a particular redshift bin, and T_{merger} represents the merging timescale. The galaxy merger rate is generally parameterized by a power law of the form $(1+z)^m$, and the value of the exponent of this parametric form has been used to place constraints on how much mass is assembled via major galaxy mergers. However, large variations in m are found in the literature, ranging from $m \sim 0$ to $m \sim 4$ (Bundy et al., 2004, 2009; Conselice et al., 2003; Guo & White, 2008; Lin et al., 2004a; Bridge et al., 2007; Lin et al., 2008; Lotz et al., 2008a; Jogee et al., 2009). Figure 1.5 taken from Bridge et al. (2010) shows that when these different merger selections were normalized to the timescale in which they were sensitive to identifying mergers, most studies agreed that the merger rate increases with redshift, however there remain some discrepancies in the absolute merger rate value at given redshift.

This discrepancy can be attributed to a combination of the following factors:

- Variation in the redshift ranges being probed.
- Small sample sizes in some of the surveys.
- Cosmic variance
- Uncertain merging timescales.
- Different selection methods in identifying mergers

The effects of the first three factors can be minimized by conducting a large volume survey and/or analyzing a large number of merger samples. Different merger selection methods and merging timescales are probably the most important uncertainties in characterizing galaxy merger rate evolution.

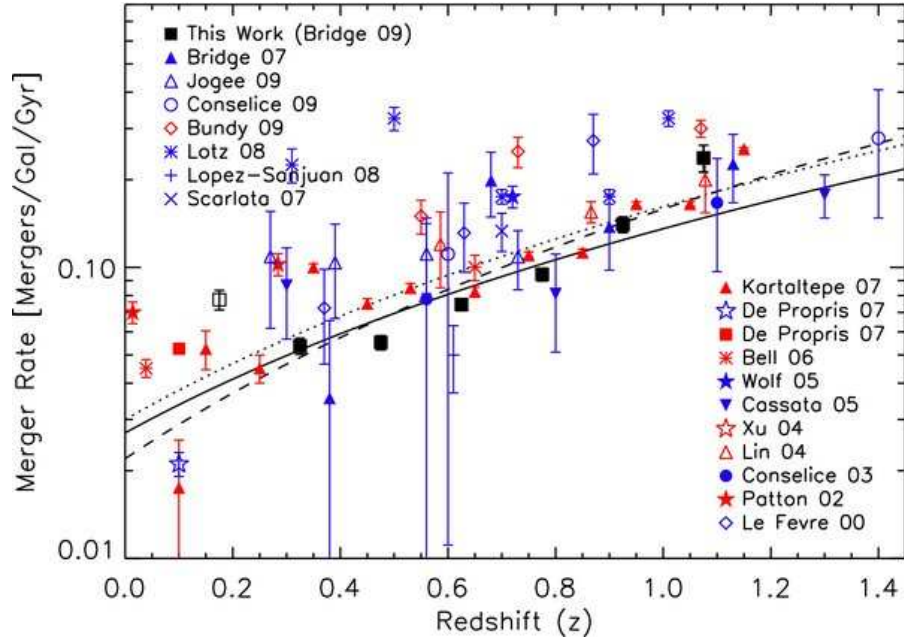


Figure 1.5 Merger rate as a function of redshift in units of mergers galaxy⁻¹ Gyr⁻¹, taken from (Bridge et al., 2010). Solid line represents the best fit to the CFHTLS data with the form of $(1+z)^m$, where $m = 2.33 \pm 0.72$; dashed line represents the best fit with $m = 2.83 \pm 0.29$ to a combined CFHTLS data with other works noted below; dotted line represents the best fit with $m = 2.43$ when a 2% statistical error is assumed. The filled black squares represent the merger rate derived from visually classified merger sample obtained from CFHTLS-Deep survey (Bridge et al., 2010). The red points show the observed merger rate derived from close pair fractions as a function of redshift from Patton et al. (2002, filled stars), Lin et al. (2004, open upward triangles), Xu et al. (2004, open star), Bell et al. (2006b, lined star), De Propriis et al. (2007, filled square), Kartaltepe et al. (2007, filled upward triangles), and Bundy et al. (2009, open diamonds). The merger rate derived from morphological studies as a function of redshift is shown in blue from Le Fèvre et al. (2000, open diamonds), Conselice et al. (2003, filled circle), Cassata et al. (2005, filled downward triangles), Wolf et al. (2005, open upward star), De Propriis et al. (2007, open star), Scarlata et al. (2007, “x”), Bridge et al. (2007, open square), Lotz et al. (2008b, lined stars), Conselice et al. (2008, open circle), López-Sanjuan et al. (2009, plus sign), Jogee et al. (2009, open upward triangle), and Bridge et al. (2010, filled black squares). The assumed merging timescale for merger fractions derived using CAS or concentration, asymmetry was 0.9 ± 0.2 Gyr from Lotz et al. (2008a) and Conselice et al. (2008). The timescale over which mergers selected via $G - M_{20}$ is assumed to be 0.4 ± 0.2 Gyr, close galaxy pairs 0.2 ± 0.1 Gyr (Lotz et al., 2008a), and visual classification (Bridge et al., 2010) 0.8 ± 0.2 Gyr.

1.3.2 Merger Selection Methods

The most widely used merger selection method is the close pair selection method (Patton et al., 2000, 2002; Lin et al., 2004a, 2008; Bundy et al., 2009; López-Sanjuan et al., 2010). This method selects galaxy merging pairs by limiting the projected separations r_p and the velocity differences δv of pair members. Patton et al. (2000) discovered that by choosing the close pair selection criteria of $5h^{-1} \text{ kpc} < r_p < 20h^{-1} \text{ kpc}$ and $\delta v \leq 500 \text{ km s}^{-1}$, most close pairs show clear tidal features which are solid indications of galaxy-galaxy interaction. The result is shown in the left panel of Figure 1.6, the right panel of which shows a mosaic of 16 images of close pairs that satisfy the selection criteria outlined in the left-hand panel. Since a close pair merging system contains two distinct galaxies, the close pair selection method tends to select mergers at their early merging phases. Although this method is straightforward, judgement is still required in sensibly defining the selection criteria. For example, some studies apply larger projected separations (Lin et al., 2008; de Ravel et al., 2009) or higher velocity differences (Bluck et al., 2012) than used by Patton et al. (2000) to select more candidates, at the cost of contaminating the merging sample with non-mergers. However, in spite of these biases, close pair selection method arguably is the more reliable way to select galaxy mergers at high redshift (i.e., $z > 1$ or higher) because all the morphological signatures as required by the morphological selection methods will be too faint to identify or too easy to confused with intrinsic peculiarity in galaxies at these redshifts, a fundamental difficulty in morphological selection methods, which we describe next.

Other categories of galaxy merger selection methods are based on the identification of morphological signatures. The most straightforward way of conducting morphological selection is visual examination. The advantage of visual examination is that it takes advantage of the brain-eye combination, which remains a superb pattern recognizer and which can detect faint tidal features that escape most automated classification methods. However, this method requires clear and well defined selection criteria to minimize the effect of personal subjective selection. Another disadvantage is that this method is labor intensive. The large numbers of galaxies in future surveys makes visual classification practically difficult. Therefore, automatic galaxy merger selection methods are needed.

One commonly used automatic method to select galaxy mergers is based on measurements of the indices of Concentration (C), Asymmetry (A) and Clumpiness (S). This ‘CAS’ system (Conselice et al., 2000) is based on the C–A system developed by Abraham et al. (1996). The concept of galaxy light concentration as a classifier was first introduced by Morgan (1972) and quantified by Doi et al. (1993). The concept became widely used in galaxy classification in mid 1990s (Abraham et al., 1994, 1996; Bershady et al., 2000; Graham et al., 2001).

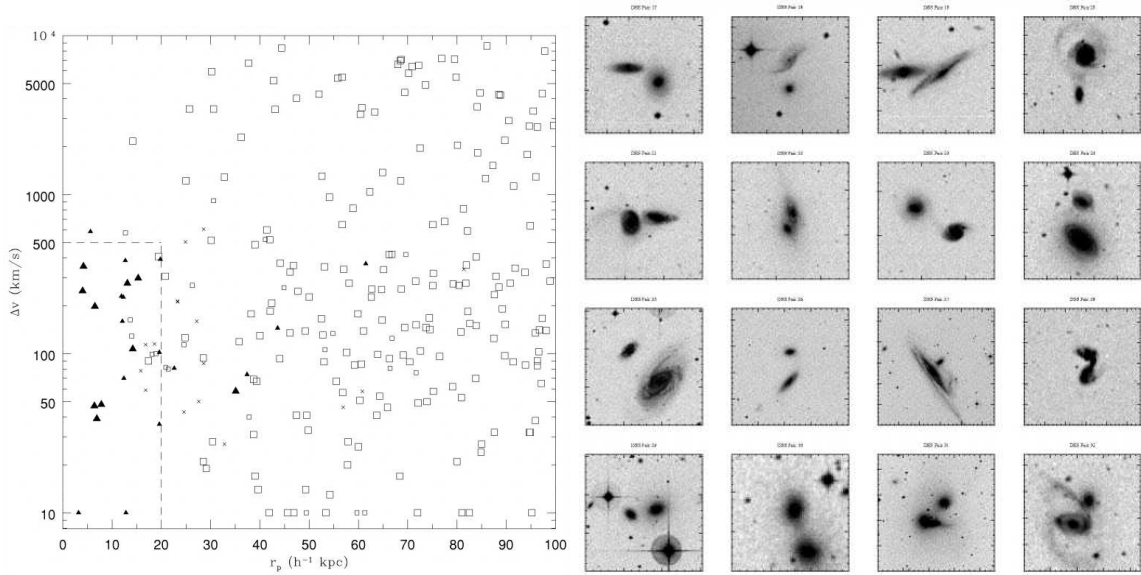


Figure 1.6 Left panel: Projected physical separation r_p versus velocity difference δv for 225 close pairs taken from Figure 5 in Patton et al. (2000). The data set was obtained from the Second Southern Sky Redshift Survey (SSRS2, da Costa et al. (1998a)). Two dashed lines indicate upper limits of the close pair selection criteria ($r_p < 20h^{-1}$ kpc and $\delta v \leq 500$ km s $^{-1}$). Different Symbols represent close pairs with different levels of interaction defined by the pair interaction classification index I_c , a visually determined index ranging from 0 to 10. I_c equals to zero indicates the close pair is ‘definitely’ not interacting, and I_c equals to 10 indicates the close pair is ‘definitely’ interacting. $I_c = 0, 1$ (large open squares), $I_c = 2, 3$ (small open squares), $I_c = 4, 6$ (crosses), $I_c = 7, 8$ (small filled triangles), $I_c = 9, 10$ (large filled triangles) Clearly close pairs with higher I_c index locate in the bottom left corner defined by the two dashed lines. Note that for plotting convenience, authors assigned pairs with velocity difference less than 10 km s $^{-1}$ to 10 km s $^{-1}$. Right panel: Mosaic of images for 16 close pairs that satisfy the selection criteria ($5h^{-1}$ kpc $< r_p < 20h^{-1}$ kpc and $\delta v \leq 500$ km s $^{-1}$), a large number of galaxies show clear signs of tidal interactions. These images were obtained from the Digitized Sky Survey with each side corresponds to $50h^{-1}$ kpc. See Figure 6 in Patton et al. (2000) for a full version (38 close pairs that satisfy the selection criteria) of the image mosaic.

One definition of the concentration index C used by Conselice et al. (2000) to select galaxy mergers is the ratio of the 80% - 20% curve of growth radii (r_{80} , r_{20}), within 1.5 times the Petrosian inverted radius at $r(1/\eta = 0.2)$, normalized by a logarithm:

$$C = 5 \times \log(r_{80\%}/r_{20\%}) \quad (1.2)$$

The parameter η used in the Petrosian inverted radius is defined as the ratio of the averaged surface brightness within r to the local surface brightness, $\eta \equiv \langle I(r) \rangle / I(r)$ (Bershady et al., 2000; Graham et al., 2005). The asymmetry index (Abraham et al., 1996) is defined as the number computed when a galaxy is rotated 180° from its center and then subtracted from its prerotated image, and the summation of the intensities of the absolute value residuals of this subtraction is compared with the original galaxy flux (Abraham et al., 1996; Brinchmann et al., 1998):

$$A = \frac{\sum_{i,j} |I(i,j) - I_{180}(i,j)|}{\sum_{i,j} |I(i,j)|} - B_{180} \quad (1.3)$$

where I is the galaxy's image and I_{180} is the image rotated by 180° with respect to the central pixel of the galaxy, B_{180} is the average asymmetry of the background. The concept of measuring the high spatial frequency clumpiness (S) is to smooth the galaxy image by a boxcar of a certain width and subtract the smoothed image from the original one. The width of the boxcar is a fraction of the Petrosian radius (e.g., in Lotz et al. (2004), the width of the boxcar is 0.25 Petrosian radius). Mathematically, The clumpiness index S , is defined by the summation of image residuals.

$$S = \frac{\sum_{i,j} |I(i,j) - I_s(i,j)|}{\sum_{i,j} |I(i,j)|} - B_s \quad (1.4)$$

where I_s is the smoothed galaxy image and B_s is the average smoothness of the background. If the clumpiness index S is small, then most of light within the galaxy is distributed in low spatial frequency structures. On the other hand, a large S index represents galaxy that is highly clumpy. During galaxy-galaxy interactions, mergers generally show prominent tidal features and enhanced regional star formations which make light distribution within galaxy mergers less concentrated, more asymmetric, and more clumpy.

Figure 1.7 gives a graphic illustration of how CAS indices are calculated, taken from Conselice et al. (2003). The automatic CAS selection criteria of $A > 0.35$ and $A > S$ is widely used in merger selection (Conselice et al., 2003; Conselice, 2006; Jogee et al., 2009) and can select roughly one-third of mergers based on the N-body simulation calibration result (Conselice, 2006). Jogee et al. (2009) performed a cross test among the visual and CAS morphological classification and found that merger rates derived from both methods agrees with each other within a factor of two at intermediate redshift for merger samples with stellar mass greater

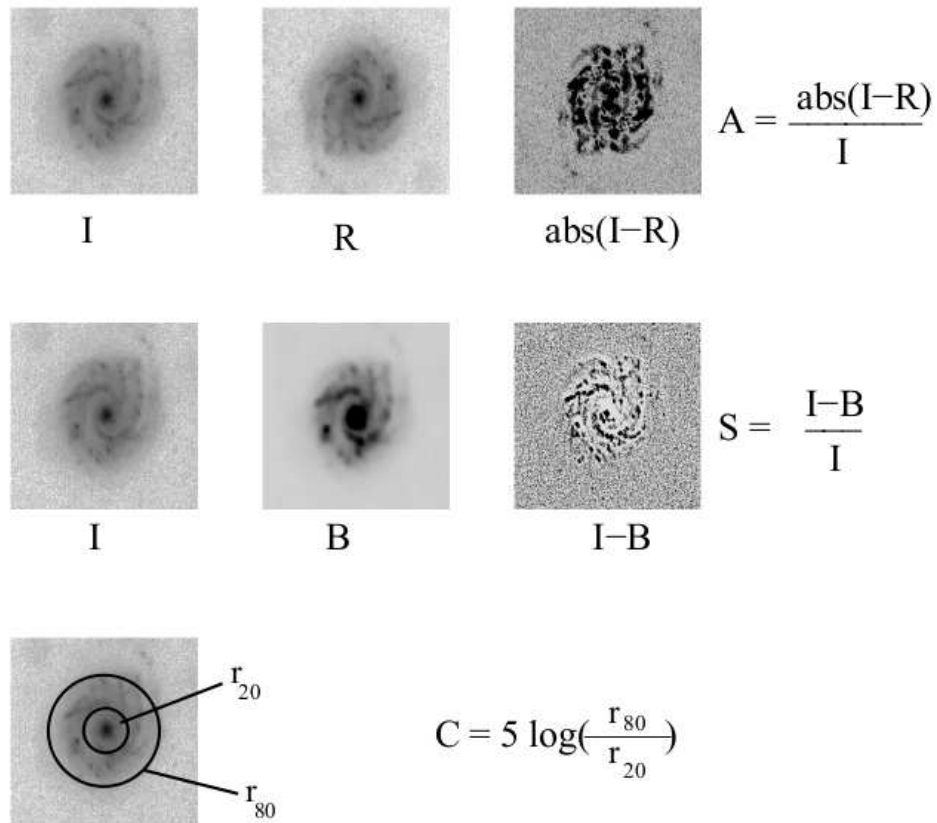


Figure 1.7 Graphical representation of how the three parameters, asymmetry (A), clumpiness (S), and concentration (C) are measured. For the measurements of A and S, I is the original galaxy image, R is this image rotated by 180° , while B is the image after it has been smoothed (blurred) by a factor of $0.3 \times r$ ($1/\eta = 0.2$) (see text for the definition of r and η).

than $M \geq 2.5 \times 10^{10} M_{\odot}$, but can overestimate the merger rate by a factor of three at $z > 0.5$ for less massive mergers ($M \geq 1.0 \times 10^{10} M_{\odot}$).

Although the CAS selection system is probably the most straightforward method to select galaxy mergers, it still has weaknesses. Firstly, the definition of a concentration index assumes a galaxy has a well-defined center. It can be practically difficult to find a center or define a galactic aperture for mergers with multiple nuclei or irregular morphology. Secondly, although the asymmetry index is sensitive to tidal features induced by galaxy-galaxy interactions, not all mergers are asymmetric (e.g., close pair mergers with larger separations) and not all asymmetric galaxies are mergers (e.g., edge on dusty spiral galaxies). Finally, the measurement of a clumpiness index requires one to define a galaxy smoothing length, which must be chosen carefully to avoid systematic effects dependent on a galaxy image's point spread function, pixel scale, distance, and angular size. Also, the bulges of highly concentrated galaxies give strong residuals that are not due to star-forming regions and must be masked out when computing the S index.

Another approach to automatic morphological merger selection is through the computation of Gini (Abraham et al., 2003) and M_{20} coefficients (Lotz et al., 2004). The Gini coefficient is a statistical evaluation based on the Lorenz curve (Lorenz, 1905), a rank-ordered cumulative distribution function of a population's wealth or, from Astronomer's point of view, a galaxy's pixel values. Figure 1.8 shows an example of the Lorenz curve, taken from Abraham et al. (2003). The diagonal line in Figure 1.8 is called the line of equality which represents a uniform distribution of wealth or galaxy pixel values. In other words, in a population where all individuals has exactly the same income gives a diagonal Lorenz curve. The Gini coefficient is defined by the ratio of the region A to the total area under the line of equality (A+B) in Figure 1.8. An evocative interpretation for the Gini coefficient taken directly from Abraham et al. (2003) is: "In other words, $G = 0$ for a perfect communist society and $G = 1$ for an absolute monarchy where all riches belong to the king!". Mathematically, the Lorenz curve is defined by the equation below. Let X be a positive random variable from a cumulative distribution function $F(x)$, and X_i denotes one of n random deviates drawn from X :

$$L(p) = \frac{1}{\bar{X}} \int_0^p X(t) dt = \frac{1}{\bar{X}} \int_0^p F^{-1}(u) du \quad (1.5)$$

where \bar{X} represents the mean value over all X_i and $F^{-1}(u)$ represents the inverse distribution function of X . The Gini coefficient is defined as the mean of the absolute difference between all combinations of X_i :

$$G = \frac{1}{2\bar{X}n(n-1)} \sum_{i=1}^n \sum_{j=1}^n |X_i - X_j| \quad (1.6)$$

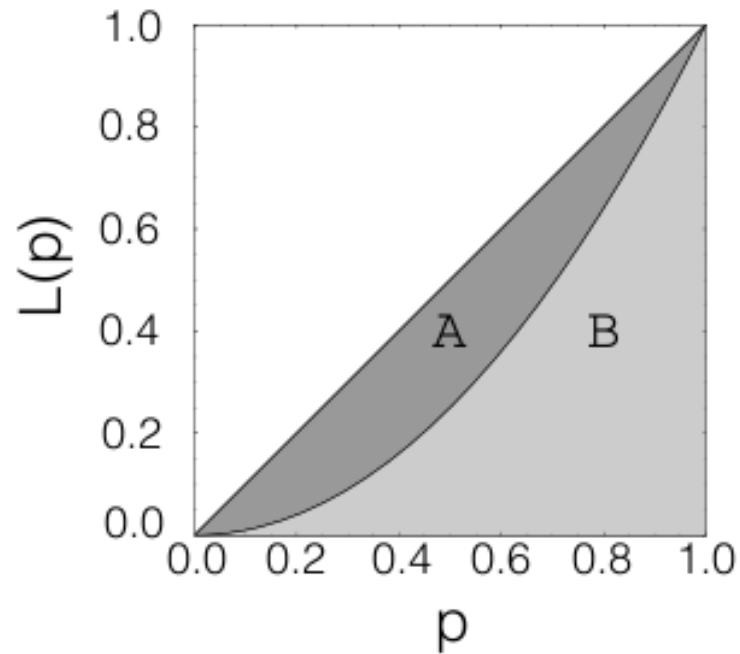


Figure 1.8 Geometric interpretation of the Gini coefficient based on the Lorenz curve. The x-axis corresponds to the quantile of the distribution, and the y-axis corresponds to the cumulative proportion. The line of equality is shown as the diagonal line, which represents a perfectly equal distribution. In this figure a schematic Lorenz curve divides the area below the line of equality into two areas, A and B. The Gini coefficient corresponds to the ratio of area A to the total area under the equality line $A+B$. The greater the deviation of a measured Lorenz curve from the line of equality, the greater the inequality.

An efficient way in calculating the Gini coefficient is to first sort the X_i into an increasing order and do the following summation (Glasser, 1962):

$$G = \frac{1}{\bar{X}n(n-1)} \sum_{i=1}^n (2i - n - 1)X_i (n > 2) \quad (1.7)$$

The computation of the M_{20} coefficient is based on the total second-order moment of light M_{tot} , which is defined by the flux of each pixel f_i multiplied by the squared distance from the pixel to the center of the galaxy, and then summed over all pixels enclosed in the aperture given by the segmentation map.

$$M_{tot} = \sum_{i=0}^n M_i = \sum_{i=0}^n f_i [(x_i - x_c)^2 + (y_i - y_c)^2] \quad (1.8)$$

where x_c, y_c is the galaxy's center. The center is computed by finding x_c, y_c such that M_{tot} is minimized. The second-order moment map traces light dispersion within a galaxy. The M_{20} coefficient is then defined as the normalized second-order moment of the brightest 20% of galaxy's flux. To compute M_{20} , one has to sort galaxy pixels by flux first and then sum M_i over the brightest pixels until the sum of the brightest pixels equals to 20% of galaxy's total flux. The normalization is done by the value of M_{tot} .

$$M_{20} \equiv \log_{10} \left(\frac{\sum_i M_i}{M_{tot}} \right), \text{ while } \sum_i f_i < 0.2 f_{tot} \quad (1.9)$$

Here f_i represents the flux of the i -th bright pixel and f_{tot} represents the total flux of the galaxy with the boundary defined by the segmentation map. Compared with the concentration index C mentioned above, the M_{20} coefficient puts more weight on spatial information by a factor of r^2 , and the galaxy boundary is not defined by a circular or elliptical aperture. The center and the aperture of the galaxy are left as free parameters. Lotz et al. (2004) discovered that most of nearby ultra luminous infrared galaxies (ULIRGs) show statistically different distributions on the Gini- M_{20} diagram. These ULIRGs tend to have higher Gini and M_{20} coefficients compared with local normal galaxies. In addition to selecting major mergers (mass ratio ranges from 1:1 to 1:4), the G- M_{20} merger selection method is also sensitive to minor mergers (mass ratio less than 1:4 and greater than 1:9) for a timescale of ~ 0.25 Gyrs (Lotz et al., 2010a,b).

1.4 Observations: The CFHTLS - Deep Survey

1.4.1 Survey Overview

The Canada-France-Hawaii Telescope Legacy Survey (CFHTLS) is a joint community project between Canada and France which obtained data over more than 450 nights over a five years

period, starting from mid-2003 to early 2009. The survey utilized a wide field imaging camera MegaCam (Boulade et al., 2003) having $36\ 2048 \times 4612$ pixel CCD to provide a 1 degree by 1 degree field of view with a pixel scale of $0.187''$. The legacy survey is comprised of three sub-surveys:

- (a) A shallow ‘Very Wide’ survey with 410 square degrees of sky coverage.
- (b) A 170 square degree ‘Wide’ survey.
- (c) A four square degree ‘Deep’ survey.

Since the science data of the thesis mainly comes from the Deep survey, we will now describe the data from the component of the survey in greater detail.

1.4.2 CFHTLS–Deep Survey

The CFHTLS Deep survey has high-quality photometry in five broad bands (u^*, g', r', i', z') with depth ranging from 26.1 (z') to 28.0 (g') mag. The integration times of the Deep Survey range from 33 to 132 hours depending on the filter ($u^* : 33$ hrs, $g' : 33$ hrs, $r' : 66$ hrs, $i' : 132$ hrs and $z' : 66$ hrs). The scientific goal of the Deep Survey was aimed mainly at the determination of cosmic equation of state, derived from observations of type Ia supernovas. Therefore, the Deep survey was tailored to the requirements of the SuperNova Legacy Survey (SNLS, see Sullivan et al. (2006b,a) for details). However, with the high quality and deep photometric data, the Deep survey serves an excellent data pool for studies other than supernova and cosmology. For example, studies of large scale structure (Semboloni et al., 2006), galaxy clustering (Olsen et al., 2007; Gavazzi & Soucail, 2007), galaxy formation and evolution (Bridge et al., 2010; Chou et al., 2011; Bielby et al., 2011) benefit from data obtained as part of the Deep Survey.

The Deep Survey has four fields (D1 - D4), covering four square degrees on the sky and each field has one square degree coverage. The survey fields were chosen to have low galactic extinction and were distributed in the right ascension for efficient observations throughout the year. In addition, the fields were also targeted by numerous other surveys, providing a rich supply of ancillary data (Table 1.4.2). The depth of the data presented in this thesis is $\sim 0-0.9$ magnitude shallower than the depth of completed Deep Survey because the data set used to classify galaxy mergers in this thesis was obtained from the SNLS group partway through the survey. The French astronomical data archive center Terapix has now released stacked mosaics and photometric catalogs of the survey fields that are publicly available¹. The latest release is

¹See the ‘Canadian Astronomy Data Center’, <http://www3.cadc-ccda.hia-ihp.nrc-cnrc.gc.ca/cadc/> for more information

Table 1.1 CFHTLS-Deep Survey Field Locations

Field	R.A. (J2000.0)	Dec. (J2000.0)	Ancillary Data
D1	02 26 00.00	-04 30 00.0	SWIRE, <i>XMM</i> , <i>GALAX</i> , VIMOS, VLA
D2	10 00 28.60	+02 12 21.0	COSMOS/ <i>ACS Spitzer</i> , VIMOS, VLA, <i>GALEX</i> , CANDELS
D3	14 19 28.01	+52 40 41.0	<i>Spitzer</i> , Deep-2, <i>GALEX</i> , CANDELS
D4	22 15 31.67	-17 44 05.7	<i>XMM</i> , <i>GALEX</i>

Table 1.2 CFHTLS-Deep Survey: Magnitude Limits

Field	Thesis Data Limiting Mag. (AB) (u^* , g' , r' , i' , z')	Completed Survey Limiting Mag. (AB) (u^* , g' , r' , i' , z')
D1	27.4, 27.8, 27.4, 27.3, 26.0	28.3, 28.0, 27.6, 27.3, 26.2
D2	26.3, 27.6, 27.2, 27.1, 25.9	26.3, 27.8, 27.4, 27.2, 26.1
D3	27.3, 27.8, 27.4, 27.2, 25.9	27.7, 27.9, 27.6, 27.3, 26.1
D4	27.4, 27.7, 27.3, 27.1, 25.9	27.5, 27.9, 27.5, 27.1, 26.1

the T0006 version. Table 1.4.2 summarizes the depth of the data presented in this thesis and the completed Deep Survey in AB magnitudes.

1.5 Integral Field Spectroscopy

In the first half of the thesis, the goal of this thesis is to better understand the space density evolution of wet and dry mergers, and how star formation is triggered and/or quenched in early- and late-stage of merging processes using galaxy merger samples obtained from CFHTLS. However, details about when and how star formation happened and the merging timescales are largely unknown. To further constrain star formation histories and merging timescales of galaxy mergers require detailed stellar population synthesis modelling of resolved stellar populations, which is heavily based on 2-D spectroscopic observations. In addition, detailed kinematic maps derived from 2-D spectroscopic observations are also crucial to modelling merging processes or understanding merging timescales. Therefore, I would like to conduct follow up spectroscopic observations for galaxy mergers at intermediate redshifts in CFHTLS fields to better understand their star formation histories and kinematics.

To conduct 2-D spectroscopic studies for mergers at intermediate redshifts, it requires a spectrograph that satisfies the following three requirements: First, the spectrograph should be

able to provide 2-D spectra with large enough field-of-view (FOV). A typical galaxy merger has a diameter of 50 kpc and the corresponding angular size at $z = 0.5$ is roughly $10''$ in the sky. Figure 1.9 shows the variation of angular size as a function of redshift of an object with a diameter of 50 kpc. That is, the spectrograph should have the capability to provide a FOV of $5''$ to $10''$. Secondly, the spectral coverage of the spectrograph needs to be in near-infrared (NIR). The H_α line, one of the most commonly used star formation tracers, is redshifted to NIR regime ($\lambda \sim 1 \mu\text{m}$) for intermediate redshift galaxy mergers. Finally, the spectrograph needs to have medium spectral resolving power to reveal enough kinematic details. A typical velocity dispersion for galaxies is on the order of several hundred kilometers per second, the velocity resolution of the spectrograph should be at least on the order of 100 km s^{-1} or less (equivalent to a spectral resolving power of $R \sim 3,000$ or higher at $\lambda \sim 1 \mu\text{m}$) to obtain enough information for kinematics studies.

1.5.1 NIR Integral Field Spectroscopy

One of the most efficient ways to obtain 2-D spectroscopic information is using integral field spectroscopy. Although the traditional 1-D long-slit spectroscopy can, in principle, be used to provide 2-D spectroscopic information by stacking up multiple exposures, it is less efficient to conduct 2-D spectroscopic studies because it is time-consuming and expensive. In addition, the variation in seeing size presented in multiple observations remains to be one uncertainty because the seeing size may affect the spectral resolving power. Thus, integral field spectroscopy has become more popular and important in contemporary astronomy due to its intrinsic capability of obtaining 2-D spectra in a single exposure. However, most of the currently available NIR integral field spectrographs (IFSs) on large telescopes are designed to work with adaptive optics systems, and usually provide small integral fields which is inadequate to the 2-D spectroscopic observations that require larger integral fields. For example, the OH-Suppressing InfraRed Imaging Spectrograph (OSIRIS) on the Keck telescope has an integral FOV of $1''.6 \times 6''.4$ and a spectral resolving power $R \sim 4,000$; the Near-Infrared Integral Field Spectrometer (NIFS) on the Gemini North telescope has an integral field of $3'' \times 3''$ and a spectral resolving power of $R \sim 5,000$. It is ideal to conduct spectroscopic studies for objects that require high spatial resolutions (e.g., galaxies at high redshifts) with these adaptive optics supported IFSs. However, these spectrographs are not ideal for medium redshift galaxy merger spectroscopic studies which large integral fields are preferred. Figure 1.9 (bottom panel) shows a montage of i' band images of four medium redshift galaxy mergers along with the size of the integral fields of OSIRIS and NIFS. It is obvious that given the integral fields of OSIRIS and NIFS, it requires more than one pointing to cover the entire surface area of any of these four galaxy mergers.

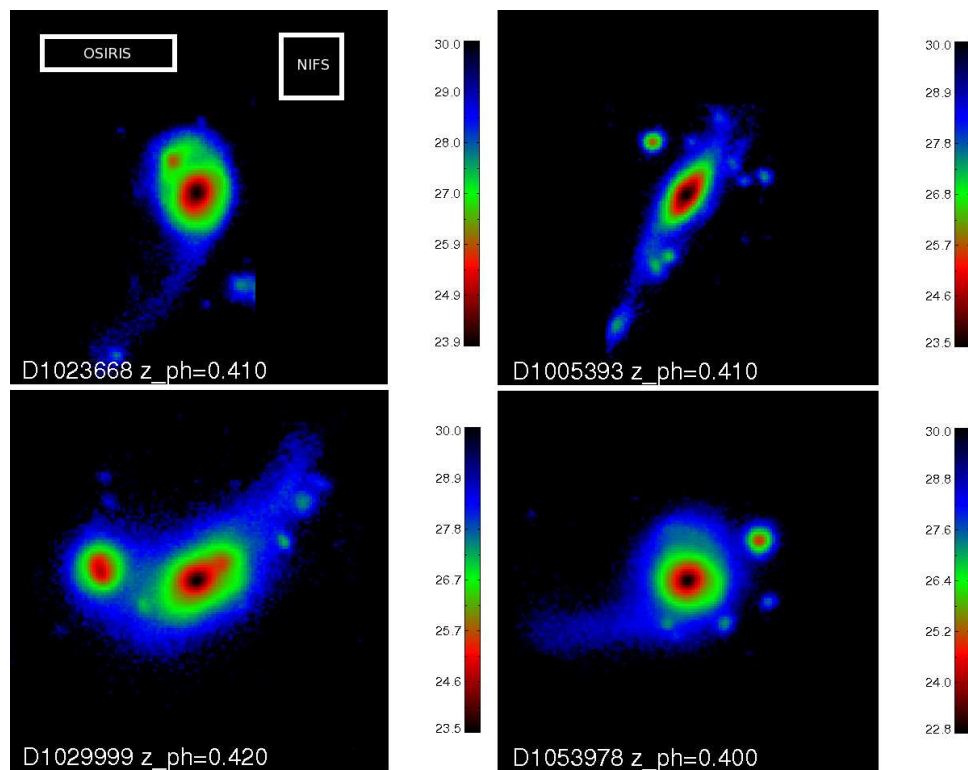
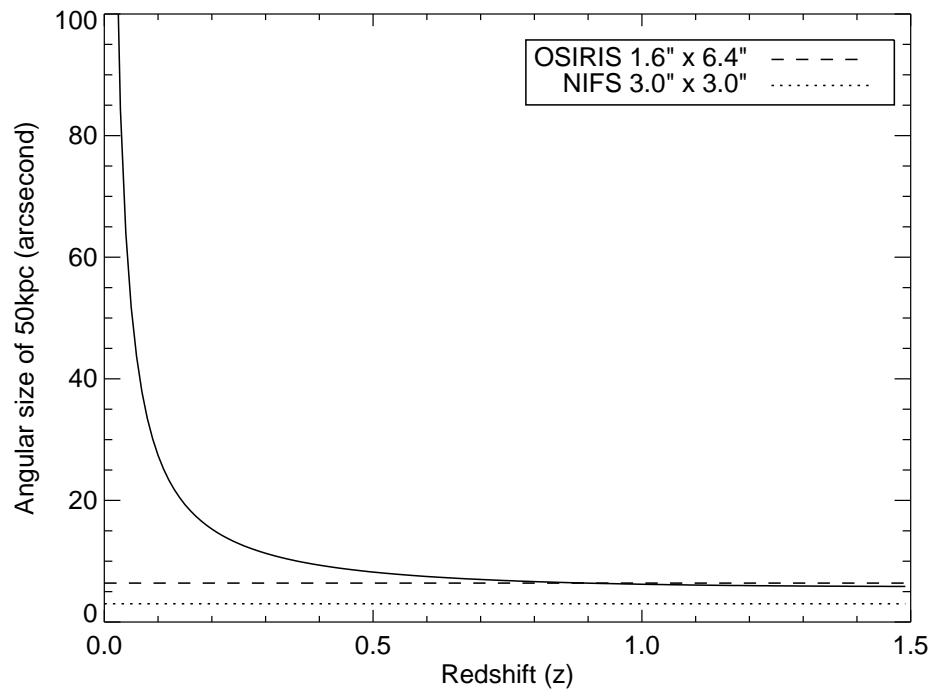


Figure 1.9 Top panel: variation of angular size of an object with a diameter of 50 kpc as a function of redshift. The angular size is roughly $10''$ at $z = 0.5$ and $6''$ at $z = 1.0$. The dotted and dashed lines indicate the integral field of view of NIFS ($3'' \times 3''$) and OSIRIS ($1.6'' \times 6.4''$), respectively. Bottom panel: a montage of i' band image of four medium redshift galaxy mergers taken from CFHTLS. The white boxes shown in the upper left picture represent the integral FOV of adaptive optics supported IFSs OSIRIS and NIFS, respectively. It is clear that the FOV provided by these IFSs cannot fully cover the entire galaxy merger in a single exposure.

Therefore, an IFS that is capable of providing a large integral field with NIR spectral coverage and medium spectral resolving power is necessary to conduct detailed 2-D spectroscopic studies of intermediate redshift galaxy mergers. §1.5.3 gives more details about potential scientific applications for such NIR IFSs.

1.5.2 Integral Field Units

The Integral Field Unit (IFU), which is known as the heart of an IFS, plays as an interface between the 2-D input integral field and the output 1-D spectra. There are three type of IFU: (1) microlens array (MLA) based IFU; (2) fiber based or fiber with MLA based IFU; and (3) image slicer based IFU. Figure 1.10 shows a cartoon of basic working principles of the three different types of IFU.

The concept of the MLA design can be traced back to the spectrograph TIGER on CFHT (Bacon et al., 1995). The 2-D input image from the telescope is sampled by a MLA and the light from each sub-section of the image is then focused on the spectrograph input plane for dispersion. To avoid spectra from overlapping, the MLA needs to be tilted with respect to the optical axis of the system. The disadvantage of the MLA design is that the resulting spectral coverage without overlapping is quite limited and the usage of the detector may not be efficient.

A fiber-fed IFU was first used in the optical spectrograph DensePak (Barden & Wade, 1988) which utilized an optical fiber array to sample the telescope input image. This fiber-fed IFU method is currently the most commonly employed technique for IFSs operating in visible wavebands. A fiber array located at the image plane of the telescope reforms the input light into a pseudo long-slit and the 2-D spectra can be obtained by dispersing the reformatted pseudo long-slit. Due to the flexibility in arranging spatial positions of fibers, the length of the fiber composed pseudo long-slit can fully match the detector size and therefore this design avoids the short spectral coverage problem when using MLA alone. However, the disadvantages of this fiber-fed IFU design are: (a) the sampling of the sky is not contiguous since there are gaps between the fiber cores; and (b) the focal ratio degradation (FRD) caused by fibers makes observations with large focal ratios that most telescopes have inefficient. The former can be overcome by placing a MLA in front of the fiber bundle to focus all the light collected by MLA into the fiber array. (Allington-Smith et al., 1997). For the MLA plus fibers system, an additional benefit of this combination is that the MLA can change the telescope focal ratio and mitigate the effect of FRD. This combination, however, is difficult to implement for IFSs operating in NIR wavebands because of the difficulties in alignment and junction between MLA and fibers during thermal cycles.

The concept of the image slicer based IFU can be traced back to Bowen (1938), with

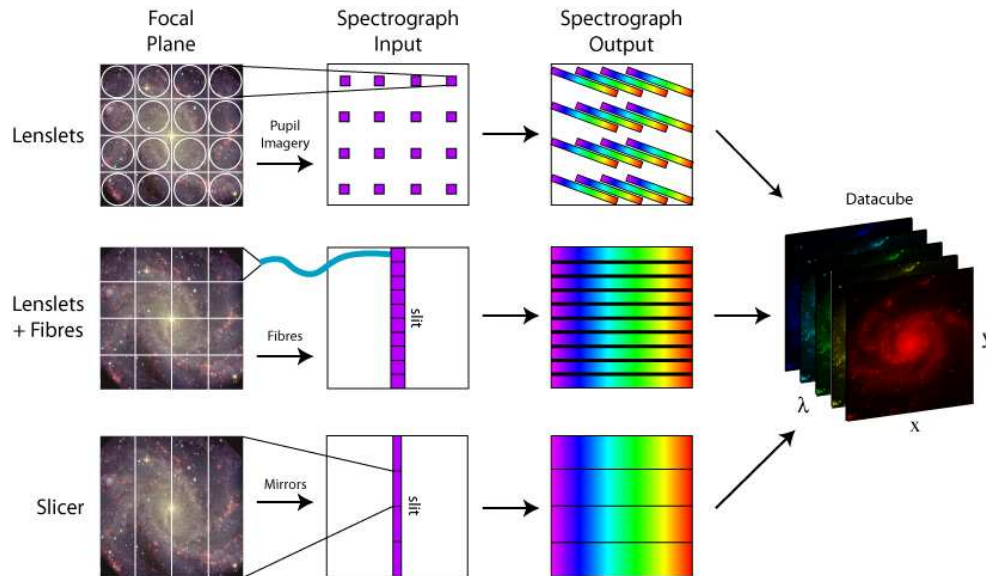


Figure 1.10 Three main IFU techniques commonly used in integral field spectroscopy. The picture is taken from Allington-Smith & Content (1998).

the current IFU variations being introduced by Diego (1993); Content (1997). The image slicer based IFU is mainly composed of two mirror arrays and basically serves as a re-imaging system. The first mirror array is the image slicer mirror array which slices an input 2-D images into several slices and the second mirror array reformats the slices in series to form a pseudo long-slit. In some cases (e.g., FISICA, see §4.2.1) an extra mirror array is added in the IFU optical path to reduce large field angle aberrations. The advantage of this technique is that the mirror based IFU is especially suitable for infrared IFSs because it can be cooled to cryogenic temperature without having the alignment issue as mentioned in the MLA plus fibers combination. Note that only the image slicer based IFU keeps the spatial information within the pseudo long-slit. The potential disadvantage of this technique is that the alignment of each components inside the IFU will be difficult because it is a fully reflective device.

1.5.3 Scientific Applications

Except for the above mentioned 2-D spectroscopic studies for medium redshift galaxy mergers, there is a myriad of astronomical questions that can significantly benefit from using a NIR IFS providing a large integral field with medium spectral resolving powers. Obviously the dynamics and chemistry of any extended object can be efficiently studied by such a spectrograph. This section gives several examples of potential scientific applications in Galactic, nearby extragalactic and high redshift extragalactic astronomy.

In Galactic astronomy, 2-D spectroscopic surveys of significant part of nearby star-forming regions, such as Orion or Eta Carinae, can be an excellent application if the size of the integral field can afford such observations. Since these Galactic objects sustain relatively large angular sizes in the sky and tend to be bright, it will be ideal to take the advantage of small telescopes to conduct 2-D spectroscopic surveys. With a spectral coverage in NIR, hydrogen lines ($[\text{Pa}_\alpha]$, $[\text{Pa}_\beta]$), He lines and iron lines ($[\text{Fe II}]$) are potential targets which can be used to understand the physical condition of the environment. In addition, Studies of shock propagation and stellar outflows within star forming regions require detailed kinematic information, which can be obtained through prominent emission lines such as $[\text{Pa}_\beta]$ or $[\text{Fe II}]$ (Luhman et al., 1998; Moon et al., 2009), one example is shown in Figure 1.11 (left panel).

Other than studies of Galactic star forming regions, nearby extragalactic astronomy can benefit from such NIR IFSs. Observations toward resolved stellar populations in nearby galaxies can reveal SED in the NIR regime, which is helpful in modelling their star formation histories (Förster Schreiber et al., 2001, 2003; Miner et al., 2011) and probing the stellar initial mass functions (van Dokkum & Conroy, 2012). Meanwhile, kinematics of galactic central kilo- or sub kilo-parsec regions can provide information of hot turbulent gas and broaden the understanding of gas fueling mechanisms for the central super massive black holes (Böker et al., 2008). This kinematic information is crucial to studies of active galactic nuclei and circumnuclear kilo-parsec size star formation rings.

In the high- z Universe, such NIR IFSs can work with large telescopes to conduct NIR spectroscopic surveys of star forming galaxies or mergers. One example is the Spectroscopic Imaging survey in the near-infrared with SINFONI (SINS), which observed 80 high redshift galaxies targeting at rest-frame optical emission lines (mainly H_α) (Förster Schreiber et al., 2009). SINS utilizes the Very Large Telescope (VLT) 8-m telescope and the NIR IFS SINFONI mainly under natural seeing conditions (a small portion of the samples were observed with adaptive optics) to extract star formation histories and kinematics of high- z star forming galaxies at $z \sim 1 - 3$. Figure 1.11 bottom right panel shows a portion of kinematic maps of high- z star forming galaxies taken from the SINS result. An NIR IFS that can provide a large integral FOV and medium spectral resolving power will be ideal to conduct H_α surveys for medium to high redshift ($z \sim 0.5 - 1.5$) star forming galaxies or mergers.

1.6 Organization of this Thesis

This thesis is organized as follows: In Chapter 2, I present the results of space density and mass-density function evolution of wet and dry mergers at their late merging stages using CFHTLS-

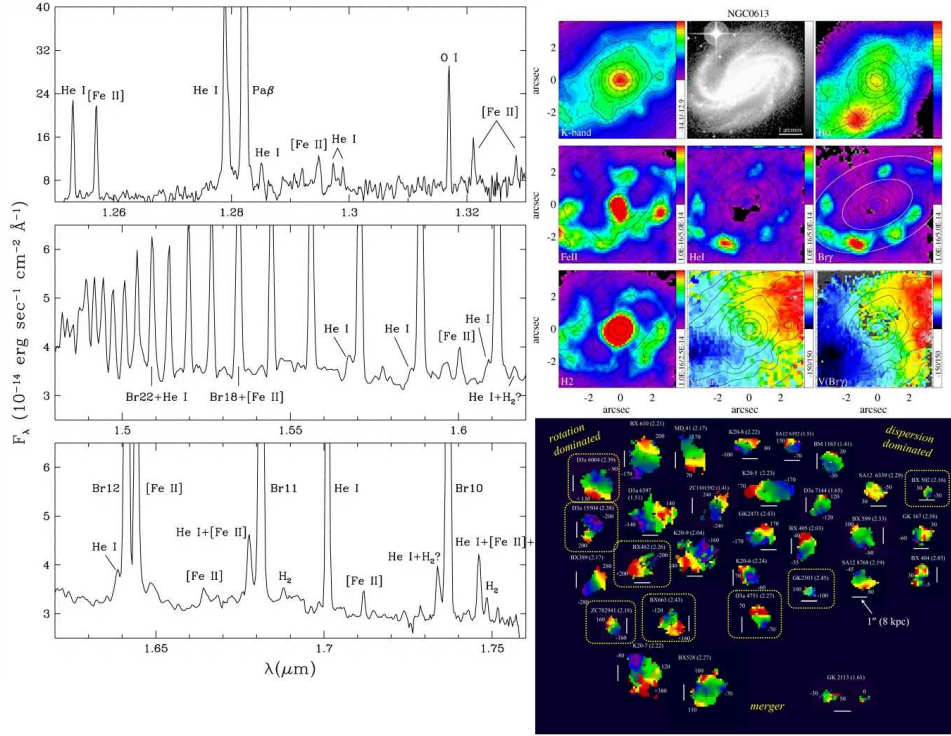


Figure 1.11 Left: a long-slit spectrum of Orion South at J and H bands taken by the Fspec (Williams et al., 1993) on the Steward 1.55m telescope with a spectral resolving power of $R \sim 3,000$ (Luhman et al., 1998). The area covered by the long-slit is $3''.5 \times 130''$. Using a medium spectral resolution NIR IFS with an integral FOV of $20'' - 50''$ on 2-m class telescopes, observations which can cover a much larger nebula area are absolutely possible. Top right: intensity and velocity maps of the central sub kilo-parsec region of a nearby galaxy NGC 613 ($z = 0.0049$) taken from Böker et al. (2008). Bottom right: velocity maps for high redshift star forming galaxies taken from the SINS survey (Förster Schreiber et al., 2009). Objects with dashed yellow round rectangles are observed with adaptive optics. The nearby and high redshift galaxies presented in right panels were mainly observed by SINFONI on VLT with $8'' \times 8''$ integral FOV under natural seeing conditions. A NIR IFS with an integral FOV of $5''$ to $10''$ can conduct spectroscopic observations for galaxies from nearby to high- z Universe.

Deep data. The material shown in Chapter 2 is published in the *Astronomical Journal* in Chou et al. (2011) Volume 141, page 87. In Chapter 3, I present the number of red-red, blue-red, and blue-blue dynamical merging pairs as a function of stellar mass and the relationship between the visible-wavelength colors of close pairs and the galactic halo masses in which they reside. The material shown in Chapter 3 has been submitted to the *Astrophysical Journal* in April 2012. In Chapter 4, I present the optical designs of an IFS called WIFIS, which can offer an unprecedented combination of spectral resolving power, spectral coverage and integral FOV among the currently available IFSs. Part of the material shown in Chapter 4 is published in 2010 *Proceedings of Society of Photographic Instrumentation Engineers (SPIE)*, Volume 7735, page 223. In Chapter 5, I describe the characterization result for the IFU used in the IFS presented in Chapter 4. Chapter 6 summarizes my thesis.

Chapter 2

The Space Density Evolution of Wet and Dry Mergers in the Canada-France-Hawaii Telescope Legacy Survey

A version of this chapter has been published in the Astronomical Journal 2011, vol. 141 pp. 87

2.1 INTRODUCTION

Hierarchical structure formation models suggest that galaxy mergers play an important role in galaxy mass assembly, but quantifying that role has remained challenging. The galaxy merger rate is generally parametrized by a power law of the form $(1+z)^m$, and the value of the exponent of this parametric form has been used to place constraints on how much mass is assembled via major galaxy mergers. Large variations in m are found in the literature, ranging from $m \sim 0$ to $m \sim 4$ (Bundy et al., 2004, 2009; Conselice et al., 2003; Guo & White, 2008; Lin et al., 2004a; Bridge et al., 2007; Lin et al., 2008; Lotz et al., 2008a; Jogee et al., 2009). A recent study by Bridge et al. (2010) analyzed these published merger rates and concluded that, overall, there is a general agreement that the merger rate at intermediate redshifts ($0.2 < z < 1.2$) does evolve, although the constraints on m remain fairly mild. Bridge et al. (2010) rule out $m < 1.5$ (i.e. flat or mild evolution) and suggest that the wide range of m reported in the literature is due to a combination of factors, including variation in the redshift ranges being probed, small sample sizes in some of the surveys, and cosmic variance.

The traditional approach used to explore the merger history of galaxies has been to estimate the fraction of merging galaxies relative to the total galaxy population. This approach has the benefit of simplicity, but it is arguable that a more physically interesting quantity is the evolving space density of mergers, rather than the merger fraction. Space densities are absolute measurements rather than relative measurements, and in that sense can stand on their own. Furthermore, space densities can be corrected for luminosity biases and other sources of incompleteness in a straightforward manner by using the standard $1/V_{\text{max}}$ formalism (Felten, 1977; Schmidt, 1968). Therefore our main aim in the present paper is to chart the evolving space density of mergers. Similar work has been undertaken by Lin et al. (2008) and Bundy et al. (2009), although these papers used pair counts to select merging galaxies, while our approach is based on morphological selection. Our analysis is thus quite complementary to Lin et al. (2008) and Bundy et al. (2009).

An important subsidiary goal of the present paper is to chart the differential merging history of color-selected sub-classes of merging galaxies. In recent years a host of observations have shown the evolutionary histories of galaxies in the so-called ‘red sequence’ and ‘blue cloud’ are different (Bundy et al., 2009; de Ravel et al., 2009; Lin et al., 2008; Willmer et al., 2006). This has led to the idea that it is important to distinguish between mergers that result in significant star-formation (‘wet mergers’) and those which merely re-organize existing stellar populations (‘dry mergers’). Wet mergers are typically associated with gas-rich systems that trigger star formation (Barton et al., 2000; Bridge et al., 2007; Lin et al., 2007; Overzier et al., 2008; Di Matteo et al., 2008; Rodríguez Zaurín et al., 2010), cause quasar activity (Hopkins et al., 2006b) and turn disk galaxies into elliptical galaxies (Toomre & Toomre, 1972). On the other hand, dry mergers (Bell et al., 2006; van Dokkum, 2005) may be responsible for the assembly of massive ($M_{\text{stellar}} \gtrsim 10^{11} M_{\odot}$) red galaxies which are observed in surprisingly high abundance at $z \sim 1$. However, the importance of these wet and dry mergers in the formation of red sequence galaxies is still not clear (Bell et al., 2007; Brown et al., 2007; Bundy et al., 2009; Faber et al., 2007; Lin et al., 2008; Scarlata et al., 2007), and it is of interest to determine if wet and dry merging systems exhibit similar evolutionary trends as a function of cosmic epoch.

A plan for this paper follows. In Section 2 we describe the observations, galaxy properties and merger identifications for our sample. This section is essentially a brief recapitulation, presented for the convenience of the reader, of the comprehensive description of the data set given in Bridge et al. (2010). In Section 3 we define our methodology for defining ‘wet’ and ‘dry’ mergers on the basis of both resolved colors and integrated colors. Section 4 is the heart of the paper, where we present the merger fraction, number density and stellar mass density for dry and wet mergers. Since recent work shows that the formation rate of massive elliptical

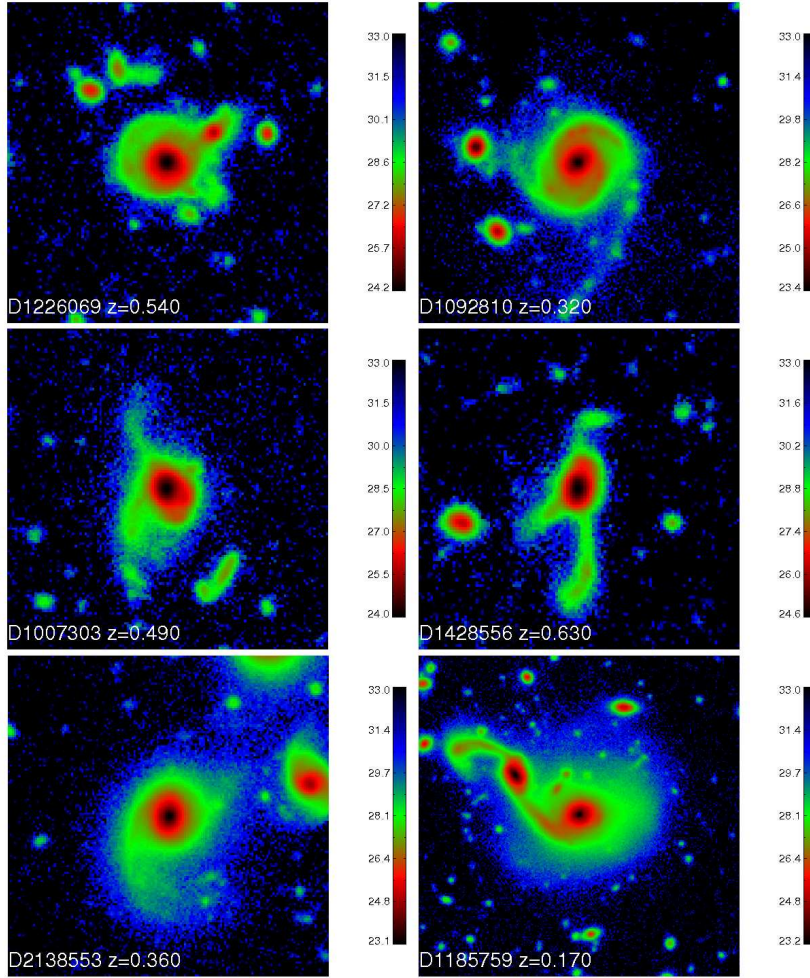


Figure 2.1 A montage of i' -band image of six typical galaxy mergers. Each stamp has the dimension of 100×100 kpc. The catalog name and the photometric redshift of the merger is shown in the bottom left corner of each stamp. The color bar indicates the i' -band magnitude.

galaxies through dry mergers is dependent on stellar masses (Bell et al., 2007; Bundy et al., 2009; Khochfar & Silk, 2009), in this section we also investigate the evolving space density of mass-segregated samples of wet and dry mergers. Our results are discussed in Section 5, and our conclusions presented in Section 6

Throughout this paper, we adopt a concordance cosmology with $H_0=70 \text{ km s}^{-1} \text{ Mpc}^{-1}$, $\Omega_M = 0.3$, and $\Omega_\Lambda = 0.7$. All photometric magnitudes are given in the AB system.

2.2 OBSERVATIONS

As has already been noted, a detailed description of the selection strategy for (and basic properties of) the galaxies analyzed in the present paper has already been presented in Bridge et al. (2010). The reader is referred to that paper for details beyond the outline presented here.

2.2.1 Data

The data in this paper come from two of the Canada-France-Hawaii Telescope Legacy Survey (CFHTLS) deep survey fields. These fields (denoted D1 and D2) together cover an area of 2 square degrees. The CFHTLS deep survey has high-quality broad-band photometry in five bands (u^* , g' , r' , i' , z') and the depth of the survey ranges from 26.0 (z') to 27.8 (g'). The optical images used to derive galaxy properties and morphological classifications were stacked by the *Elixir* image processing pipeline (Magnier & Cuillandre, 2004) to produce deep optical stacks with precise astrometric solutions. The typical seeing for the final stacks is 0.7''-0.8'' in the i' -band. The source extraction and photometry were performed on each field using SExtractor (Bertin & Arnouts, 1996) in dual image mode. The source detection was performed in the i' filter ($i' \sim 26.3$). A bad pixel mask was applied to the image prior to running the program to avoid noisy or contaminated regions caused by spikes or halos of bright stars. The total area masked is less than 10% for each field.

2.2.2 Merger identifications

Merging galaxies were selected visually, with multiple cross-checks on the visual classifications, and using simulations to characterize detection thresholds for features that are signatures of mergers. Visual classifications are labor intensive and somewhat subjective, but remain the best method presently available if accuracy is the ultimate goal. Interacting galaxies are defined as systems with a tidal tail or bridge. All galaxies down to an $i'_{vega} \leq 22.9$ mag ($\sim 27,000$) were inspected resulting in a final sample of 1298 merging galaxies. Figure 2.1 presents a montage of i' -band image of six typical galaxy mergers. The merger identification rate for galaxies with $i'_{vega} \leq 21.9$ mag is estimated to be $> 90\%$, and drops rather quickly at fainter magnitudes. Therefore in the present paper the $i'_{vega} = 21.9$ mag is used as the limit for merger identification. The redshift completeness limit was estimated by artificially redshifting low-redshift galaxies. For this completeness test, a group of galaxy mergers with redshift ranges from $z = 0.3$ to $z = 0.45$ and $M_g \leq -21.0$ mag were selected. They were artificially redshifted to higher redshifts after accounting for the k-correction, change in angular size and surface brightness dimming. After this step the merger identification was conducted once again and found to be

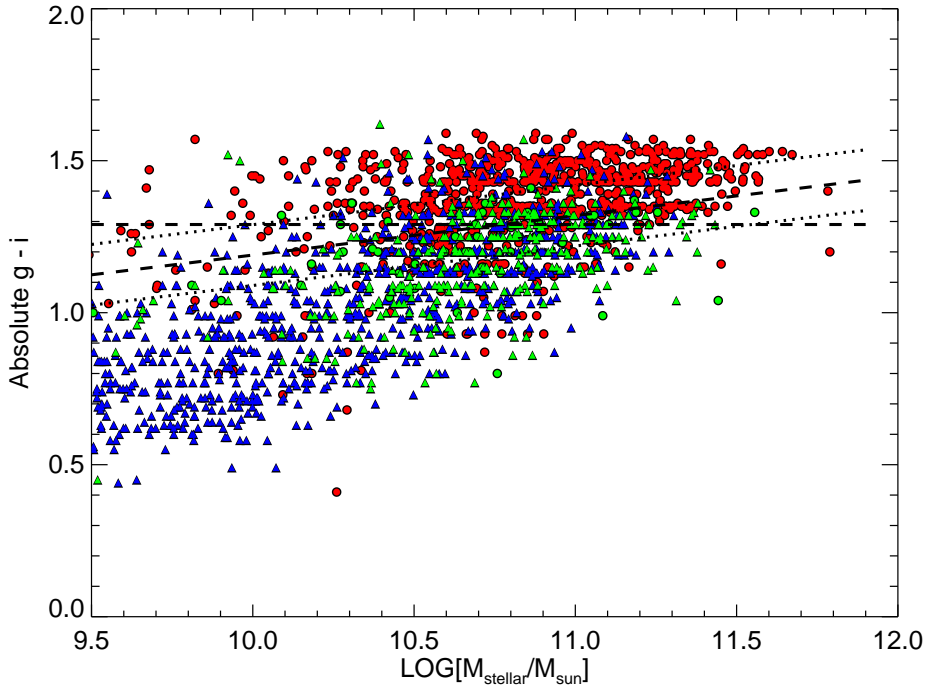


Figure 2.2 Colors of ~ 2200 field galaxies in the CFHTLS survey. The red filled circles and blue triangles represent the visually classified elliptical galaxies and spiral galaxies, respectively. The dashed line with a slope of 0.13 is derived from the red sequence fitting of 115 visually-classified elliptical galaxies with spectroscopic redshifts from the COSMOS; two equally spaced parallel dotted lines are used for merger classification test (described in the text). The horizontal dashed line represents rest frame color $g' - i' = 1.29$ mag, and is also used for the same test. The green circles and triangles represent elliptical galaxies and spiral galaxies with MIPS $24\mu m$ detections. As described in the text, we assign the MIPS-detected galaxies with $g' - i'$ color greater than the color bimodality line to the blue population. The results of merger classification test is shown in Figure 2.3, see text for more information.

acceptably high out to $z \sim 0.7$, where $\sim 85\%$ of the redshifted mergers could be still be identified as mergers, and the false positive contamination remains minimal. This redshift limit is particularly important because we utilize a $1/V_{\max}$ weighting to correct the Malmquist bias and to compute number densities. *It is important to note that V_{\max} of mergers presented in this paper is defined as the maximum volume over which mergers can be identified as such, and not the maximum redshift at which a given galaxy's integrated magnitude remains above the detection threshold.* As described in the next section, we calculated the V_{\max} value from the z_{\max} provided by the Z-Peg code which denotes the maximum redshift that the template SEDs is fainter than the observed limiting magnitude ($i'_{\text{vega}} \leq 21.9$ mag).

2.2.3 Galaxy properties

The CFHTLS survey has high quality five broad band photometry which makes the derivation of accurate photometric redshifts, ages and stellar masses possible. The galaxy properties were derived by comparing the spectral energy distributions (SEDs) obtained from observed fluxes to a set of template SEDs. The best-fit SEDs were determined through a standard minimum χ^2 fitting between the template SEDs and the observed fluxes. The template SEDs were computed by the PEGASE-II galaxy evolution code (Fioc & Rocca-Volmerange, 1997; Le Borgne & Rocca-Volmerange, 2002; Le Borgne et al., 2004) and were integrated through the CFHT filters. The SED fits were undertaken using the Z-Peg code (Bolzonella et al., 2000; Le Borgne & Rocca-Volmerange, 2002) and details are described in Bridge et al. (2010). The photometric accuracy is determined by comparing the derived photometric redshifts to the spectroscopic redshifts in the SNLS sample (Howell et al., 2005; Bronder et al., 2008). The accuracy of the photometric redshift down to $i \sim 22.5$ is $\sigma_{\Delta z}/(1+z) = 0.04$. The stellar mass for each merger was also estimated using the Z-Peg code by integrating the total star formation history (SFH) of the best-fit model, up to the best-fit age and subtracting off mass loss from late stages of stellar evolution.

2.3 Classification of Wet and Dry Mergers

We used two techniques to try to distinguish between wet and dry mergers. The common starting point for both methods is subdivision into red and blue stellar populations on the basis of rest-frame color relative to a fiducial reference color (Van Dokkum 2005; Willmer et al. 2006). Our approach to defining this reference color uses the rest frame $g' - i'$ versus g' color-magnitude diagram for ~ 2200 visually classified field galaxies in the CFHTLS D1 and D2 field (see Figure 2.2). Red dots represent visually classified elliptical galaxies and blue

dots indicate spiral galaxies. The green dots indicate the objects with MIPS $24\mu\text{m}$ detection (down to a flux limit of $340 \mu\text{Jy}$). Cowie & Barger (2008) report that at $z < 1.5$ most red galaxies with a $24\mu\text{m}$ flux $> 80\mu\text{Jy}$ fall into the blue cloud after the appropriate dust extinction is applied. To account for the color change in dusty sources, we artificially assign the green dots with $g' - i'$ color greater than the color bimodality to the blue cloud. In addition, color bimodality is known to be magnitude or stellar mass-dependent and usually derived from the fitting of red sequence objects (van Dokkum et al., 2000; Willmer et al., 2006). Therefore, the following stellar-mass-dependent fiducial color cut was adopted based on the red sequence fitting of 115 visually classified elliptical field galaxies with spectroscopic redshifts from Cosmological Evolution Survey (COSMOS) (Scoville et al., 2007; Lilly et al., 2007). The fitting line is expressed by the following equation:

$$(g' - i')_{\text{rest}} = -0.0076 + 0.13 \times M_{\text{stellar}} - C \quad (2.1)$$

The constant C serves as a parameter to control the vertical position of the fitting line on the diagram. To account for the potential classification errors caused by different slopes and C values, we have explored the implications of changing the free parameters in Equation (1) and find that all trends reported in this paper remain robust to the specific numerical values chosen. To show this, in several key figures in this paper we will bracket the results obtained using Equation (1) with curves showing the envelope obtained by using three values of C (0, 0.1 and 0.2) as well as using a perfectly horizontal line set at $g' - i' = 1.29$ mag to divide field galaxies into blue and red clouds¹

2.3.1 Method I: integrated colors

The first method for segregating wet mergers from dry mergers is, essentially, the simplest conceivable. We look at the total integrated color of the merger which we obtained by summing over all pixels in the merger (or merging pair), and simply note if the integrated color of the complete system is redder or bluer than the fiducial color threshold. Mergers whose integrated colors are redder than the threshold are deemed ‘dry’, and systems bluer than the threshold are deemed ‘wet’. As mentioned above, the only caveat is that we re-assign dry mergers with $24\mu\text{m}$ detections to the wet merger category on the assumption that these are blue galaxies being reddened by dust.

¹The reason to use $g' - i' = 1.29$ is that we try to balance the contamination of blue (red) galaxies in red (blue) cloud. For the $g' - i' = 1.29$ color cut the contamination on both sides is 14%.

This simple method is straightforward but it is not at all obvious that loss of the spatial information is an acceptable trade-off for such simplicity. For example, what if one object in a merging system is redder than the fiducial color, while the other object is bluer? We therefore decided to explore a somewhat more refined approach to ‘wet’ vs. ‘dry’ merger classification that retains some component of the spatial information in the images.

2.3.2 Method II: spatially resolved colors

Our second method is based on analysis of the colors of individual pixels. Pixels with rest-frame $g' - i'$ color greater than the fiducial threshold are labeled as ‘red’, and the ratio of the total flux in red pixels to the flux in all pixels is calculated. We refer to this quantity as the ‘Red-to-Total ratio’, (R/T) , given by:

$$(R/T) = \frac{F_{red}}{F_{total}} \quad (2.2)$$

where F_{red} indicates flux contained in red pixels and F_{total} refers to the flux from the entire merger.

The idea behind (R/T) is to crudely decompose a merger into individual stellar populations. A galaxy with $(R/T) = 1$ is comprised entirely of stellar populations with colors on the red sequence, while a merger with $(R/T) = 0$ is comprised entirely of stellar populations in the blue cloud. Of course most mergers are expected to lie somewhere in between these extremes. For the sake of simplicity we choose to define systems with $(R/T) > 0.5$ as being ‘dry’, but throughout this paper we will explore the results obtained for range of (R/T) values to ensure that our conclusions are not tied to any specific value of (R/T) . Finally, we note that in common with Method I, we re-assign ‘dry’ mergers with MIPS 24 μm detections into the blue cloud.

2.4 RESULTS

2.4.1 Merger Fractions

Figure 2.3 shows the merger fraction for a stellar mass-limited sample of objects ($M_* > 10^{9.5} M_\odot$), f_M , as a function of redshift. We define this merger fraction in the obvious way as $f_M = N_M/N$, where N_M is the number of mergers and N is the number of galaxies in the complete sample (once again, we refer the reader to Bridge et al. 2010 for details of the full sample). The figure shows curves for wet mergers (blue lines), dry mergers (red lines), and all mergers (black lines). The left-hand panel shows the merger fraction computed using integrated colors while the right-hand panel shows the corresponding curves computed using

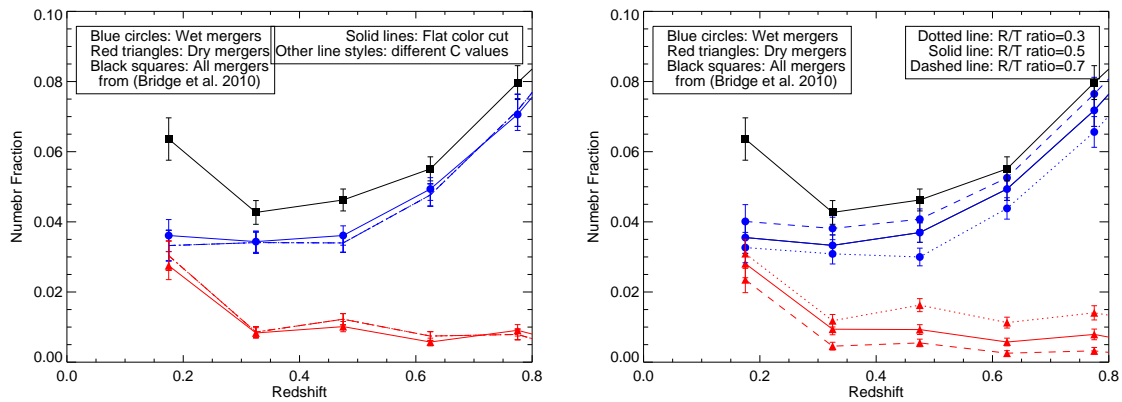


Figure 2.3 Merger fractions computed using two different methods. The left panel shows the merger fraction derived from different fiducial color cuts with integrated colors, while the right panel shows the merger fraction derived from different internal color ratios (see text for details). It is obvious that different color cuts do not affect the scientific results. In both panels, red curves indicate dry mergers, blue curves indicate wet mergers, and black curves indicate the total merging population. It is clear that the increase with redshift in the wet merger fraction, and the decrease with redshift in the dry merger fraction, are robust and do not depend on the selection method. Error bars are estimated by assuming Poisson errors.

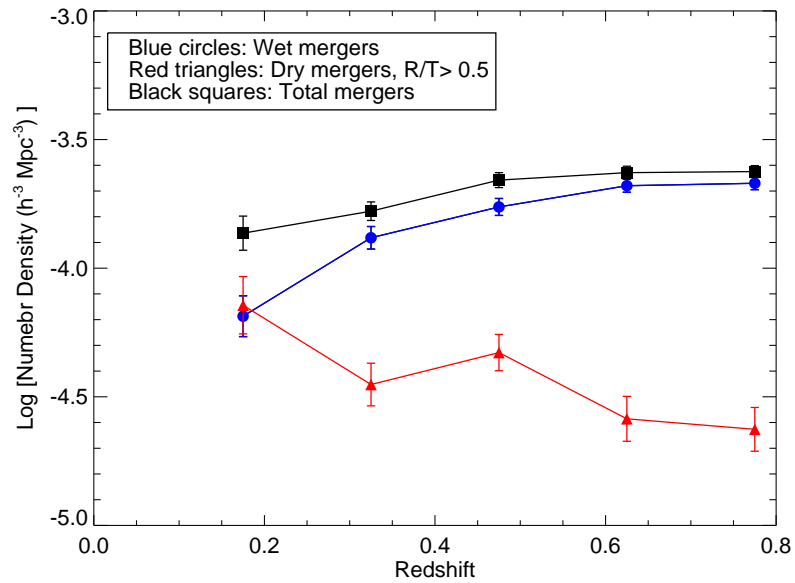


Figure 2.4 Co-moving space densities of wet and dry mergers. As in the previous figure, blue and red curves correspond to wet and dry mergers, respectively, while the black curve shows the total for all mergers. The growth in the total space density of mergers is modest, increasing by about a factor of two over the redshift range probed. The wet and dry merging galaxies show opposite trends with redshift. The space density of wet mergers is increasing with redshift, while that of dry mergers is (perhaps) modestly decreasing.

resolved colors, at three different values of the red-to-total fraction used to segregate wet and dry mergers. Errors were estimated assuming Poisson statistics.

A number of interesting results emerge from these figures. Firstly, a comparison of the left and right panels shows that the general trends seen are quite independent of the specific methodology used. In all cases the dry merger fraction is almost equal to the wet merger fraction at the lowest-redshift bin (around $z \sim 0.2$) but the fraction of dry mergers decreases rather quickly between $z = 0.2 - 0.3$ and remains somewhat flat at higher redshifts. In contrast to this, the fraction of wet mergers increases rather rapidly with redshift, and by $z \sim 0.7$ wet mergers outnumber dry ones by a factor of 6 to 1. The dry merger fraction at $z = 0.5$ is $\sim 1\%$, which is in agreement with the dry merger fraction of 1% at $\langle z \rangle \sim 0.55$ obtained by De Propris et al. (2010) using close pairs.

Another interesting feature noted in Figure 2.3 is the way that the total merger fraction drops from around 6.5% at $z \sim 0.2$ to around 4.5% between $z = 0.3$ and $z = 0.5$, before rising to around 7% at $z = 0.7$. This effect seems due to the rapid growth with time in dry mergers at lower redshifts and the rapid decline with time in wet mergers in earlier Universe. This dip is seen more predominantly in D2 than in D1 field suggesting that cosmic variance is involved (Bridge et al., 2010). The non-monotonic changes in the merging fraction seen suggest that over the redshift range being probed a power law provides a poor description for the changing total merging fraction. At the same time, the monotonic changes in the wet and dry populations when considered separately suggests that a power law might provide a reasonable description for these sub-populations, so we have analyzed them separately. We adopt the analytic form $f_M = f_0 \times (1 + z)^m$, where f_0 is also set as a free parameter, and m is the standard power-law index. Fitting this relationship to the $R/T = 0.5$ curves on the right-hand panel yields $m = 2.0 \pm 0.3$ and $m = -3.1 \pm 0.5$ for wet and dry mergers, respectively. Since the merger sample may not be complete in the last bin at $z = 0.77$, and the power-law indices $m = 1.2 \pm 0.4$ and $m = -4.1 \pm 0.6$ are obtained for wet and dry mergers with the last data point excluded. We see that the dry merging population is best described by negative evolution, and the basic statement that the wet and dry populations are evolving with the same m is excluded at more than three sigma significance².

The careful consideration given to selection effects described in Bridge et al. (2010) leaves little doubt that the effects noted in Figure 2.3 are really seen in the observational data, but what is their ultimate physical significance? The visibility of red and blue stellar populations is expected to be a strong function of k-corrections, which differ markedly for red and blue

²Note that the total and wet merger fraction keep increasing rapidly beyond the redshift limit of this paper, so it seems that the merger rate evolves more dramatically at higher redshifts than at $z < 0.7$. See Bridge et al. (2010) for more discussion on this point.

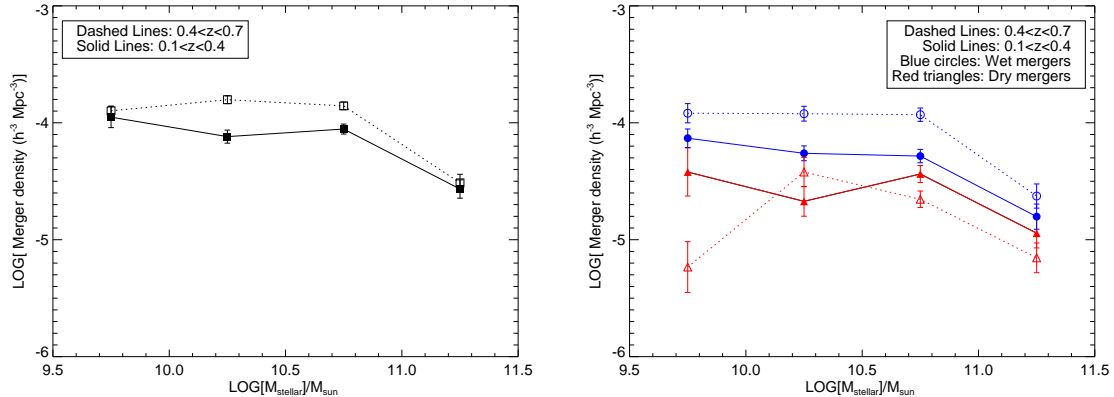


Figure 2.5 [Left:] Mass density function in mergers in two redshift bins. The high-redshift bin ($0.4 < z < 0.7$) is shown with a dashed curve, while the low redshift bin ($0.1 < z < 0.4$) is shown with a solid curve. We see evidence for modest evolution in the mass density function, with most change occurring at intermediate masses, and no change at the high and low mass ends. [Right:] Subdivision of the data in the left hand panel into wet and dry mergers. Line styles segregate the data into two redshift bins, as for the left-hand panel. As in previous figures, red curves correspond to dry mergers, and blue curves correspond to wet mergers. For mergers in the most massive bin, an increase in the dry merger space density is offset by a decrease in the wet merger space density, so the total space density is nearly conserved. At intermediate masses, the mass density function of dry mergers is nearly unchanged in both redshift bins, with perhaps some evidence for a slight decrease in the space density of intermediate-mass dry mergers at high redshifts. On the other hand, the mass density function of wet mergers is increasing with redshift.

galaxies at $z \sim 0.7$ (the redshift limit for the present paper). To better understand this, we will now explore the space densities of mergers using the V_{\max} formalism to account for color and luminosity biases.

2.4.2 The Space Density of Merging Galaxies

Figure 2.4 shows the evolving co-moving space density of all mergers, as well as of the subsamples of wet and dry mergers. These space densities were computed by weighting each merger by $1/V_{\max}$ and summing over redshift bins in the standard manner (see, for example, Totani & Yoshii (1998)). As described in §2.2, V_{\max} values were computed using the Z-PEG code, although it is once again emphasized that in most cases the ultimate limit on the detectable volume is set by the merger classification limit rather than the magnitude detection limit. As

with the previous figure, the blue and red curve correspond to wet and dry mergers, while the total for the whole population is shown in black. Error bars were computed by bootstrap resampling.

The main trends noted in our description of Figure 2.3 remain visible in Figure 2.4, most notably the mild negative evolution in the dry mergers and positive evolution in the wet mergers, with the populations converging at around $z \sim 0.2$. However, a rather striking new feature emerges: *the total space density for all mergers apparently remains almost flat at all redshifts, with a mild increment at $z > 0.5$.* In other words, the decline with redshift in dry mergers appears almost perfectly offset by a rise with redshift in the fraction of wet mergers.

2.4.3 The Role of Stellar Mass

As was noted in the Introduction, stellar mass is the central parameter driving much of galaxy evolution. What role does stellar mass play in conditioning the effects noted in the previous two figures? To explore this, we applied a stellar mass cut of $10^{9.5}M_{\odot}$ and a redshift cut of $z > 0.1$ to our merger sample, leaving 1296 objects in our mass-limited sample. Figure 2.5 shows the stellar mass density function for this total sample in two redshift bins (left-hand panel), and the result obtained when the total sample is divided into wet and dry sub-populations (right-hand panel; note we have adopted the same color scheme as for the previous figures). Error bars were derived in the same manner as for the merger number density.

The left-hand panel of Figure 2.5 shows that the increase in the space density of high-redshift mergers occurs mostly in intermediate-mass galaxies. There is little evidence for an increase in the space density of merging galaxies in either our lowest mass bin or in our highest mass bin, which is consistent with the result shown in Figure 2.4. The overall situation is clarified further in the right hand panel, which shows that: (i) the space density of wet mergers is always higher than the space density of dry mergers, regardless of redshift or mass; (ii) the space density of wet mergers evolves more quickly than the space density of dry mergers. In fact, in the dry merging population there appears to be little evidence for redshift evolution except in the lowest mass bin, suggesting that any evolutionary trends for dry mergers occur mainly at low masses.

2.5 DISCUSSION

We would like to compare results with those presented in recent papers by Lin et al. (2008), hereafter Lin08, and Jogee et al. (2009), hereafter Jog09. These authors used different selection

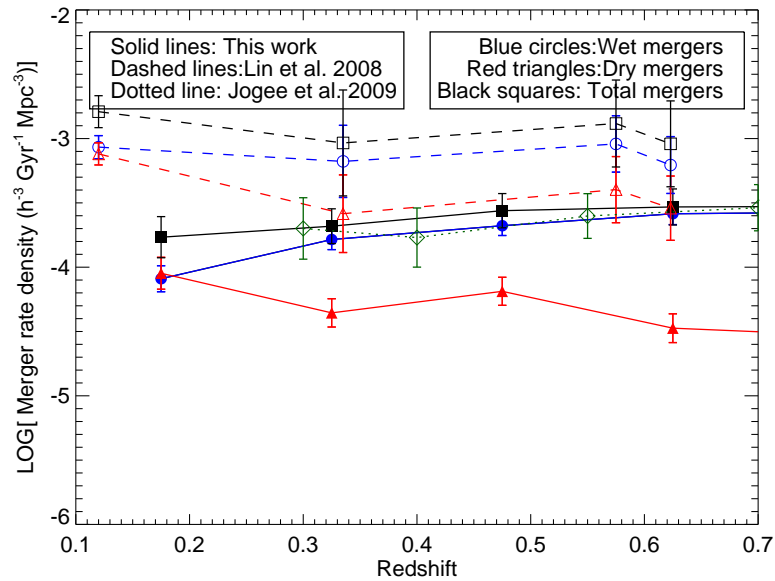


Figure 2.6 A comparison of the evolving merger rate density in the present work with the results obtained by Lin et al. (2008; Lin08) and Jogee et al. (2009; Jog09) using pair counts and automatic morphological selection. Our merger rate density is derived by choosing a merging time scale of 0.8 ± 0.2 Gyr, as discussed in Bridge et al. (2010). The merging timescale used by Lin08 and Jog09 is 0.5 Gyr. Qualitative trends determined using both methods are similar. The absolute merger rate density from our work is lower by a factor of ~ 3 compared to Lin08 but is comparable to that in Jog09 (see text for details).

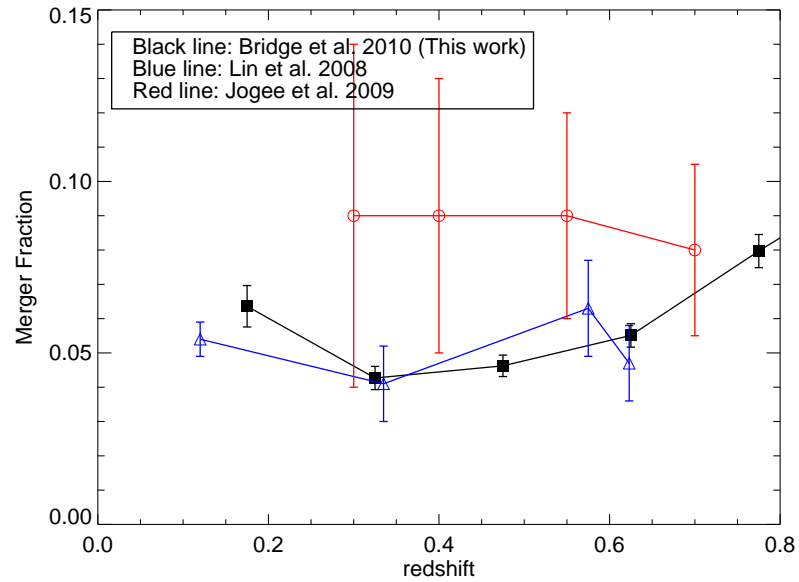


Figure 2.7 Comparison of merger fractions with two different merger selection methods. The blue line and triangles indicate the merger fraction derived from close pair merger selection method; the red line and circles indicate the merger fraction derived from mergers selected by automated CAS asymmetry and clumpiness parameters. In Figure 2.6 our merger rate density is in good agreement with data obtained by Jog09. However, it is clear that our merger fraction is in good agreement with data obtained by Lin08. This indicates that the main uncertainty comes from different merging timescales and correction factors that translate the empirical merger fraction to merger rate density (see text for more details).

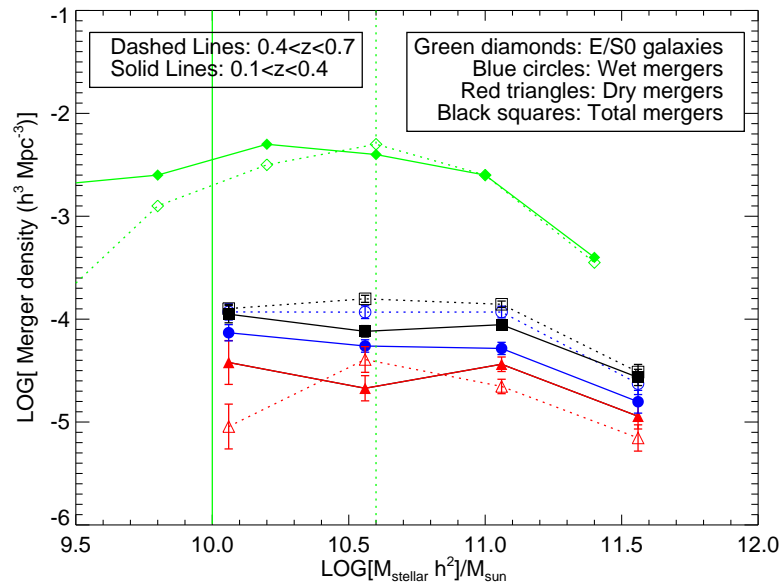


Figure 2.8 A comparison of the stellar mass density function for mergers in the present sample with the corresponding stellar mass density function for early-type galaxies presented in Bundy et al. (2005). The data point of early-type galaxies are more or less from the same redshift bins. Two vertical lines indicate the completeness limit of early-type galaxies in different redshifts. The x-axis is in units of $M_{\text{stellar}} h^2 / M_{\text{sun}}$ to facilitate comparison with Bundy et al. (2005). Note the completely different shapes for these two samples, even though elliptical galaxies are associated with the end product of mergers, and there is no evolution in the space density of massive elliptical galaxies. This shows quite clearly that not all of the major mergers will end up with massive elliptical galaxies, unless the merger timescale is much longer than usually assumed. See text for details.

methods. Lin08 used close pair selection while Jog09 used morphological criteria quantified using the automated CAS method (Conselice et al., 2000; Conselice, 2003). Both sets of authors provide estimates of the volumetric merger rate with respect to redshift, which provides a nice focus for inter-comparisons. The Lin08 merger sample is composed of data from DEEP2 (Davis et al., 2003), the Team Keck Treasury Redshift Survey (Wirth et al., 2004), the Southern Sky Redshift Survey 2 (da Costa et al., 1998b), the Millennium Galaxy Catalog (Liske et al., 2003; Driver et al., 2005) and the Canadian Network for Observational Cosmology Field Galaxy Redshift Survey 2 (Yee et al., 2000), for a total of 506 close pairs (compared to 1300 mergers presented in this work). The Jog09 sample is taken from the GEMS (Rix et al., 2004) with spectrophotometric redshifts and spectral energy distributions taken from COMBO-17 (Wolf et al., 2004), for a total of ~ 800 mergers.

In order to compare our results with Lin08 and Jog09, the merger densities shown in Figure 2.4 must be converted to a merger rate density, and this requires a merging timescale to be assumed. The appropriate timescale to use is unclear, since it may be a function of a number of factors, such as galaxy mass ratio and gas fraction (Lotz et al., 2009b,a). Additionally, different merger selection methods would select mergers in different merging stages and therefore require different correction factors as well as merging timescales. To make sure that we are comparing the same thing in Figure 2.6, we still keep the original merging timescales used in the corresponding papers. Recent work based on N-body/hydrodynamical simulations for equal mass gas-rich mergers suggests that merging timescales typically range from 0.2 Gyr to 0.9 Gyr, on the basis of a comparison between the tidal features seen and those produced by simulations³. Note that the simulation results are valid for mergers selected by different methods. At present we will adopt a merging timescale of 0.8 ± 0.2 Gyr estimated from visual comparison of both dry and wet mergers presented in Bridge et al. (2010) who also visually examined the snapshots of simulated mergers and the duration in which the galaxies would be classified as ‘interacting’ under the criteria used to classify the galaxies presented in the paper. Figure 2.6 shows the comoving merger rate density for galaxies with redshifts $z < 0.7$ in these samples⁴. In this figure dashed lines show the results from Lin08, the dotted line corresponds to Jog09, and solid lines show results obtained from our data. Blue and red colors represent wet and dry mergers, respectively. Note that Jog09 does not break the sample down into wet and dry mergers, so only the total merger rate density is shown.

³It is worth noting that the most obvious features emerge at the first encounter and the final merging stages (Lotz et al., 2008b).

⁴Lin08 designate around 30% of their merger sample as ‘mixed pairs’ (one red galaxy and one blue galaxy). For purposes of comparison with our own data, we have simply included half of the Lin08 galaxies in the wet mergers category and half of them in the dry mergers category. None of the conclusions in this paper are sensitive to this assumption.

Figure 2.6 shows several interesting things. Firstly, we see that the merger rate density from our work is generally a factor of ~ 3 less than that in Lin08, although it is in excellent agreement with that of Jog09. Note however, that our merger fraction (shown in Figure 2.7) is actually in rather good agreement with that of Lin08, so that the disagreement between our merger rate density and that of Lin08 is due to differences in translating from an empirically close pair fraction to a merger rate density. This step is more complicated in a pair count analysis than it is in a morphological analysis, because the former involves a number of coefficients (fraction of galaxy pairs to mergers and correction factor for the companion selection effect due to the limited luminosity range) with values that are not well established. The relevant issues are well-described in Lin08, who outline the steps needed to obtain Equation 5 in that paper. Another factor that may explain the difference with regard to Lin08 include the possibility that we are missing some mergers because their tidal tails have dropped below our surface brightness detection threshold, although this possibility has been investigated in Bridge et al. (2010) and we believe it is not a significant factor (i.e. certainly less than a factor of two) out to $z = 0.7$.

Another interesting result that emerges from the figure is the fact that in spite of the systematic offset in the absolute rates compared to Lin08, many of the qualitative trends are similar when our results are compared to theirs. In both cases, the density of wet mergers is essentially identical to the density of dry mergers in the nearby Universe. Also in both cases the evolution in the *total* merger rate densities at these redshifts is at best modest, and arguably flat. Finally, in both cases we see that wet mergers and dry mergers have different trends as a function of redshift, and that dry mergers contribute less at higher redshifts than they do at lower redshifts. Since Jog09 do not break their sample into wet and dry mergers, we are unable to compare such trends with their sample, although as we have already noted our overall merger rate densities are in good agreement with theirs.

It is highly interesting to explore how the trends shown in Figure 2.6 depend on the stellar masses of the mergers. This can be most clearly seen by placing the stellar mass density functions for wet and dry mergers (already shown in Figure 2.5, subdivided into two redshift bins) into a broader context, namely that which includes the population these systems are thought to develop into in hierarchical models. To this end, Figure 2.8 shows the mass density function (converted to our chosen IMF) for early-type galaxies at both $z \sim 0.4$ and $z \sim 0.7$ taken from Bundy et al. (2005), as well as our derived mass density functions for mergers. If elliptical galaxies are being built up via mergers then the mass density function of elliptical galaxies is a cumulative quantity that grows with redshift. A simple model that is worth considering in one in which any redshift-dependent trends have no mass dependence. On a logarithmic plot such a uniform multiplicative mass growth simply displaces the mass density function upward, so the

normalization of the mass density function changes with redshift, but the shape of the curve stays the same. Although this argument is based on an assumption that the merger products do not participate in subsequent mergers, since the typical merger rate is $\sim 10^{-4} \text{ Gyr}^{-1} \text{ Mpc}^{-3}$ it is not very likely that a typical elliptical galaxy will experience multiple massive mergers within the span of a few billion years. It is clear from Figure 2.8 that *the shapes of the mass density function curves are completely different and that of early-type galaxies has very little evolution at the high mass end (with observational errors)*. This seems rather surprising in light of the expectation that major mergers are thought to be the progenitor population for elliptical galaxies. In that case, one expects that the two curves would have similar shapes, with the early-type galaxy mass density function displaced upwards as elliptical galaxies form, unless the merging timescale is a very strong function of mass. We conclude from this analysis that if elliptical galaxies are formed from mergers, at some epoch the mass density function of mergers must have been very different from that seen today.

We can explore the implications of the very different forms for the merger and early-type galaxy mass density functions by adopting the approach first used by Toomre (1977), who compared the number of elliptical galaxies to the number of merging galaxies in the Second Reference Catalog (de Vaucouleurs et al., 1976b). At the high-mass end, we find that the space density of massive early-type galaxies is only a factor of five larger than the space density of wet mergers. This is a highly puzzling result to understand in a framework in which massive mergers produce elliptical galaxies, since our results also show that the merger rate has not changed rapidly since $z=0.7$. Unless the merging timescale is $\sim 5 \text{ Gyr}$ for massive mergers (about an order of magnitude larger than current estimates) the space density of massive galaxy mergers would greatly over-produce massive elliptical galaxies if these mergers all turn into elliptical systems. A better match is seen for elliptical galaxies of intermediate mass ($\sim 10^{10.5} M_{\odot}$), which outnumber mergers by a factor of about 50 in Figure 2.8. In this case, a merging timescale of order 0.5 Gyr is consistent with mergers producing the space density of elliptical galaxies seen in Figure 2.8 (again, assuming a constant merger rate, as is suggested from our data).

We conclude from this analysis that not all massive major mergers ($M_{\text{stellar}} > 10^{11} M_{\odot}$) will end up being the most massive elliptical galaxies, at least not at $z < 0.7$. On the other hand, the merging timescales suggested by numerical simulations are consistent with the data if we suppose that less massive elliptical galaxies form via mergers. Since low-intermediate mass ellipticals are 10–100 times more common than their most massive counterparts, the hierarchical explanation for the origin of elliptical galaxies may be correct for the vast majority of ellipticals, even if incorrect for the most massive ones.

If the massive merging systems captured in Figure 2.8 do not end up as elliptical galaxies,

what is their ultimate fate? That is unclear. However, Robertson & Bullock (2008); Governato et al. (2009); Kannappan et al. (2009) claim that the end product of major mergers of gas-rich spiral galaxies is often a larger spiral galaxy, so that would seem to be a strong possibility.

2.6 CONCLUSION

We have divided the 1298 merging galaxies in Bridge et al. (2010) into ‘wet’ and ‘dry’ merging categories using two techniques, one based on integrated colors and the other based on spatially resolved colors. We find that our general results are independent of the specific method used. Using the V_{max} methodology, we are able to compute the space density of merging galaxies out to redshift $z \sim 0.7$. The local space density of wet mergers is essentially identical to the local space density of dry mergers. The space density of merging galaxies does not change rapidly with redshift, increasing by less than a factor of two out to $z \sim 0.7$. On the other hand, wet and dry merging populations show different evolutionary trends. At higher redshifts dry mergers are a smaller fraction of the total merging galaxy population, while the wet mergers make a proportionately greater contribution.

We have compared the stellar mass density function of merging galaxies to the corresponding stellar mass density function of early-type galaxies, and find that these functions are very different in shape, even though the former are thought to be the progenitor population of the latter. We also show that the present space density of massive galaxy mergers is already similar (within a factor of three) to that of *existing* massive elliptical galaxies. This suggests that not all of the massive major mergers will end up with massive elliptical galaxies, unless the merging timescale is much longer than expected. On the other hand, for systems with masses less than $10^{10.5} M_{\odot}$, we find that the space density of low-intermediate mass elliptical galaxies is consistent with hierarchical formation via mergers.

Acknowledgements

The authors thank NSERC and the Government of Ontario for funding this research. We also thank Damien Le Borgne and Karl Glazebrook for useful discussions.

Chapter 3

A Close-pair Analysis of Damp Mergers at Intermediate Redshifts

A version of this chapter has been accepted by the Astrophysical Journal

3.1 INTRODUCTION

The mass assembly history of the Universe is a major observable predicted by galaxy formation and evolution scenarios. Observational data have shown that galaxies in the local Universe generally fall into two categories: quiescent ellipticals, which dominate the massive galaxy population ($M_* \geq 10^{10.5} M_\odot$), and blue star forming disc galaxies which occupy the lower mass regime (Baldry et al., 2004; Balogh et al., 2004; Kauffmann et al., 2003). This color bimodality, which groups galaxies into the ‘blue cloud’ and ‘red sequence’, exists not only in the local Universe, but also out to redshift $z \sim 1$ (Bell et al., 2004; Willmer et al., 2006), and possibly up to $z = 2$ and beyond (Pozzetti et al., 2010; Conselice et al., 2011). The origin and the evolution of this color bimodality is largely unknown. The traditional view of red systems is that they are early-type galaxies that form monolithically at high redshift (Eggen et al., 1962) though in modern theories of galaxy evolution ‘nurture’ plays as big a role as ‘nature’, and evolution is driven by several physical mechanisms, including galaxy-galaxy interactions (Blumenthal et al., 1984; Di Matteo et al., 2005; Hopkins et al., 2010; Lambas et al., 2012), in-falling cold gas (Dekel & Birnboim, 2006; Dekel et al., 2009; Kereš et al., 2009; Bournaud et al., 2011), and hot halo gas quenching (Birnboim & Dekel, 2003; Birnboim et al., 2007; Panuzzo et al., 2011; Gabor & Davé, 2012).

There is now a considerable body of evidence suggesting that the red sequence is populated

by galaxies which have somehow ‘migrated’ there from the blue cloud (Martin et al., 2007; Hughes & Cortese, 2009; Bundy et al., 2010; Shapiro et al., 2010). Observations have shown that the total stellar mass of red massive galaxies ($M_* \geq 10^{11} M_\odot$) has grown by a factor of two since redshift $z \sim 1$, while that of blue disc galaxies remains more or less the same (Bell et al., 2004; Faber et al., 2007; Abraham et al., 2007). Furthermore, Brammer et al. (2011) show that this mass growth trend can be traced up to $z \sim 2.2$. There is some evidence suggesting that the (visible wavelength) color transformation timescale for migration of a blue galaxy onto the red sequence is fast, ~ 1 Gyr (Bell et al., 2004; Blanton, 2006). Assuming the average gas to total mass ratio of late type galaxies is $\sim 15\%$ (Rubin et al., 1985) and a typical constant star formation rate is a few solar mass per year, it is difficult to consume all the gas content in blue galaxies within a timescale of 1 Gyr. In addition, simulations show that filaments in the intergalactic medium (IGM) can also channel new and fresh gas into galactic halos, continuously feeding galaxies (Brooks et al., 2009; Kereš et al., 2009). Thus, in order to move a galaxy from the blue cloud onto the red sequence the star formation must be sharply cut off or quenched, rather than being stopped simply by a depleted supply of cold gas. Most mechanisms invoked for quenching star formation involve various forms of feedback which couples star-formation in disks to hot gas in galactic halos (Gabor et al., 2010).

One well-studied mechanism for halting star-formation is the hot halo quenching model, which suggests that as gas falls into galactic dark matter halos it is heated by virial shocks. If the mass of a dark matter halo exceeds $\sim 10^{12} M_\odot$, the rate of gravitational heating by shocks is greater than that of radiative cooling. As a result, a hot virialized gas halo is formed near the virial radius. These hot halo shocks heat up the in-falling cold gas immediately, which prevents the gas from collapsing and forming new stars (Birnboim & Dekel, 2003; Birnboim et al., 2007). The hot halo quenching model alone cannot quench all star formation within a galaxy since some in-falling gas will still cool down and form stars in the center of the galaxy, but this model provides a simple explanation for the mass-dependent bimodal galaxy distribution (Dekel & Birnboim, 2006; Cattaneo et al., 2006; Panuzzo et al., 2011).

Another interesting mechanism for halting star-formation in galaxies is major merger quenching. In this picture, intense star formation triggered by the merging of two or more galaxies of roughly comparable stellar mass produces strong stellar winds that expel and/or heat the ISM through shocks or feedback from supernovae (Cox et al., 2006; Ceverino & Klypin, 2009). Stellar feedback from supernovae is probably not sufficient to quench the star formation of the entire galaxy (Springel et al., 2005), so some additional energy source is probably required to supplement this quenching process.

Some semi-analytical models integrate these various ideas into a hybrid picture in which

a central super massive black hole (SMBH) is an additional energy supply. In the hot halo quenching model, the in-falling cold gas could accrete on to the SMBH and trigger low luminosity AGN and radio emission, which is also known as the ‘radio’ mode of the quenching process (Croton et al., 2006; Hopkins & Hernquist, 2006). Similarly, major mergers can induce more violent material accretion and generate large amounts of energy feedback, which is known as the ‘quasar’ mode of the quenching process. Both of these energetic feedback mechanisms involving the central SMBH could effectively expel or heat the surrounding gas disc and further quench the star formation activities (Hopkins et al., 2006b).

Irrespective of how quenching operates, galaxy mergers are the central building blocks of the standard Λ -dominated cold dark matter model (Λ -CDM; Cole et al., 2008; Neistein & Dekel, 2008). In this model major mergers transform disk galaxies into more massive spheroids (Toomre & Toomre, 1972; Toomre, 1977). However, it is difficult to study the full process of star formation and/or quenching mechanisms from single snapshots of galaxy mergers. An alternative way forward is to study the evolution of large samples of mergers as a function of redshift, and to connect these observations to models for triggering or quenching star-formation. One approach along these lines is to investigate the merger rate density evolution of ‘wet’ and ‘dry’ mergers at different merging stages. So-called wet mergers refer to galaxy mergers with intense star formation, while dry mergers are those with weak star formation.

Recent studies suggest that the fraction of dry mergers is low at high redshifts ($z \geq 0.5$) but that dry mergers become important at low redshifts ($z < 0.2$) (Lin et al., 2008; de Ravel et al., 2009; De Propris et al., 2010; Chou et al., 2011). However, the reason for this change in the dominant mode of merging, the mechanism by which color transformations occur, and the corresponding merging timescales remain uncertain. A significant complication is that different procedures for defining samples result in mergers with quite different properties. In essence, there are two main ways to define samples of mergers. The first is based on morphological criteria, and focuses on structural disturbances and/or tidal features (Conselice et al., 2000, 2003; Bridge et al., 2007; Jogee et al., 2009; Bridge et al., 2010; Chou et al., 2011). Because mergers tend to show strong morphological disturbances at the first encounter and the last merging stage (Conselice, 2006; Lotz et al., 2008b), morphological selection methods are biased toward selecting mergers at later merging stages. The second approach is based on dynamical selection, which identifies mergers by limiting the projected physical separation and the velocity differences between two close pair members (Patton et al., 2000; Lin et al., 2004a, 2008; López-Sanjuan et al., 2010).

Bridge et al. (2010) showed that when these different merger selections were normalized to the timescale in which they were sensitive to identifying mergers, the majority of studies agreed

that the merger rate increases with redshift, however there remain some discrepancies in the absolute merger rate value at given redshift. Lotz et al (2010) suggest that differences in the range of mass ratios measured by different techniques and differing parent galaxy selection also likely contribute to the variation between studies.

In this paper, our aim is to better constrain the number density of dry mergers at early merging stages, and to test the hot halo quenching model. Our analysis is based on imaging data from the Deep component of the Canada-France Hawaii Telescope Legacy Survey (CFHTLS-Deep), and spectroscopic follow-up with the 6.5m Magellan and 5.1m Palomar Telescopes. Combining these datasets allowed us to define a sample of close kinematic pairs with redshifts between $z = 0.1 - 1.2$. We investigate (1) the number of red-red, blue-red and blue-blue galaxy pairs as a function of stellar mass, and (2) the relationship between the visible-wavelength colors of close pairs and the galactic halo masses in which they reside. In a companion paper, Chou et al. (2011), we have constrained the dry merger number density at late merging stages, and in this paper we seek to undertake a complementary analysis of systems in the early stages of merging. By comparing the number density of dry mergers at different merging stages, we hope to clarify whether star formation is enhanced or quenched (or both, at different epochs) by mergers.

The paper is organized as follows: §2 gives the details of the sample selection, data reduction and the derivation of galaxy properties (stellar masses, color, spectroscopic redshifts, etc.) Results are presented in §3, followed by discussion in §4. Our conclusions are presented in §5. Throughout this paper, we adopt a concordance cosmology with $H_0=70 \text{ km s}^{-1} \text{ Mpc}^{-1}$, $\Omega_M = 0.3$, and $\Omega_\Lambda = 0.7$.

3.2 OBSERVATIONS

3.2.1 Photometry and galaxy Properties

The optical photometry used in this paper primarily comes from two of the (CFHTLS) deep survey fields. Together these fields (denoted D1 and D4) cover an area of 2 square degrees. Another small fraction ($\sim 0.6\%$) of the sample comes from D2 field. The CFHTLS deep survey has high-quality broad-band photometry in five bands (u^*, g', r', i', z') and the depth of the survey ranges from 26.0 (z') to 27.8 (g'). The typical seeing for the final stacks is $0.7''-0.8''$ in the i' -band. We utilized the imaging stacks from the Supernovae Legacy Survey (Sullivan et al., 2006b, SNLS) for all our objects. The source extraction and photometry were performed on each field using SExtractor (Bertin & Arnouts, 1996) in dual image mode. The source detection was performed in the i' filter ($i' \sim 26.3$), after applying a bad pixel mask, to avoid noisy or

contaminated regions caused by spikes or halos of bright stars. The total area masked is less than 10% for each field.

Galaxy properties such as stellar mass and star formation rate were derived by comparing the five broad band photometry to a set of template SEDs. The best-fit SEDs were determined through a standard minimum χ^2 fitting between the template SEDs and the observed fluxes. The template SEDs were computed by the PEGASE-II galaxy evolution code (Fioc & Rocca-Volmerange, 1997; Le Borgne & Rocca-Volmerange, 2002; Le Borgne et al., 2004) and were convolved with the CFHT filters. A more detailed description of the SED fitting analysis that was performed on this data set using the Z-Peg code (Bolzonella et al., 2000; Le Borgne & Rocca-Volmerange, 2002) can be found in Bridge et al. (2010); Chou et al. (2011). The stellar mass for each pair member was estimated using the Z-Peg code by integrating the total star formation history (SFH) of the best-fit model, up to the best-fit age and subtracting off mass loss from late stages of stellar evolution. The galaxy properties of close pairs were taken from the SNLS catalog. An upper limit of photometric redshift $z < 1.2$ was applied for the sample presented in this paper because (a) there are a limited number of galaxies with robust spectroscopic redshifts $z > 1.2$ to calibrate the photometric redshifts, and (b) because the difference between the spectroscopic and photometric redshift becomes too large to derive accurate galaxy properties.

Although the galaxy properties of most of close pair galaxies are derived based on five broad band photometries and the best-fit photometric redshift, we ran Z-Peg code again for close pair galaxies with confident spectroscopic redshift measurements (see Section 3.2.4 for the measurement of spectroscopic redshifts) by replacing the best-fit photometric redshifts to confident spectroscopic ones to obtain precise galaxy properties. This indicates that the results presented in Figure 4 & 5 are based on confident spectroscopic redshift measurements.

3.2.2 Spectroscopy of the photometric sample

This sample described in the previous section was used to define targets for a three-night spectroscopic program undertaken using the Inamori-Magellan Areal Camera and Spectrograph (IMACS) on the Magellan Baade 6.5-m telescope in October 2005 and September 2006. SCOPIC, a **S**pectroscopic study of **C**lose **O**ptical **P**airs **I**n **C**FHTLS (PI Bridge), was aimed at identifying a large sample (~ 1500) of kinematic close galaxy pairs in order to further understand the galaxy merger rate and the connection between mergers, star-formation and AGN activity. Close pair candidates were selected using the following criteria, 1) a projected separation between pair members less than $50 h^{-1}\text{kpc}$, 2) an apparent i' magnitude difference ≤ 1.5 mag, in order to select roughly equal mass or major mergers and 3) a photometric redshift

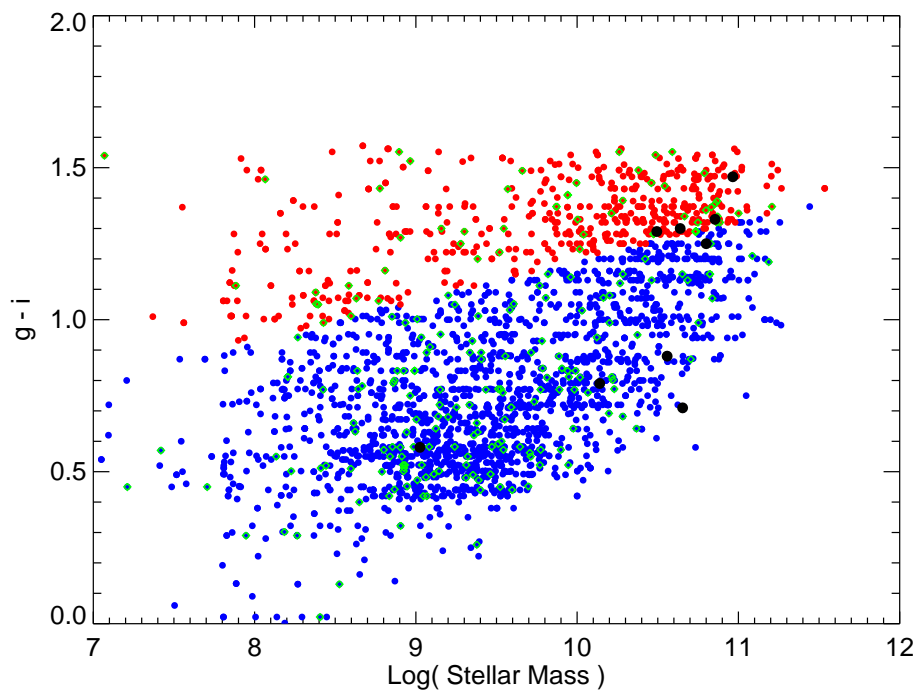


Figure 3.1 Rest frame $g' - i'$ color versus stellar mass for close pair galaxies in D1, D2 and D4 fields. Red and blue dots represent the red and blue galaxies classified via the fiducial color as shown in Equation 3.1. Black dots are D1 galaxies with MIPS24 μm detection. Green diamonds represent close pairs which both galaxies are detected. Note that red pairs also span a wide range in stellar mass, showing that there is no selection bias towards the bright red pairs. We artificially assign objects with 24 μm detection as blue galaxies and excluded objects with photometric redshifts greater than 1.2. The sample end up with 607 red and 2143 blue galaxies.

difference between pair members of $\Delta z < 0.15(1 + z)$. This selection resulted in a sample of 2730 galaxies that resided in close pair (or triple system) of galaxies over 2 square degrees and were spectroscopically targeted.

Figure 3.2 shows the the distribution of projected separations for the potential close pairs in the fields chosen, along with our sampling of this distribution. The black solid curve represents the projected separation distribution for all the potential close pairs presented in D1 and D4 fields which satisfy the above mentioned selection criteria. The green solid and dashed curves represent the projected separation distribution of total and non-detected close pairs, respectively. The red dashed curve represents the projected separation distribution for detected close pairs (both pair members have confident redshift measurements, see Section 3.2.4 for more details). To increase the statistics, both green and red curves have a bin size of $5 h^{-1}$ kpc. There is clearly a significant drop in our sampling of the parent population of potential close pairs when the projected separation is greater than $20 h^{-1}$ kpc, which indicates a selection bias for close pairs with smaller projected separations. This selection bias is due to a higher selection priority of potential close pairs with projected separations smaller than $20 h^{-1}$ kpc. Therefore, all the results presented in the present paper focus mainly on close pairs with projected separations smaller than $20 h^{-1}$ kpc.

Slits masks were designed to maximize the opportunity to get redshifts for both members of a close pair, by placing either a separate slit on each member or using a single slit that was tilted to cover both galaxies. IMACS has one short (f/2) and one long (f/4) focal ratio camera. The observations were conducted with the short camera and the $8K \times 8K$ Mosaic2 CCD detector, providing a field of view of $27'.4$ in diameter. We used the grating with a groove density of 200 lines/mm and the diffraction order m of 1 to achieve the spectral coverage of 5000 - 9000 Å with the central wavelength at 6600 Å. The slit width was set to $1''$ and the wavelength dispersion was $\sim 10 \text{ \AA}$ per slit or equivalent to a resolving power of 660. The individual exposure times were 30 minutes with a total average integration time for each slit mask of 1.5 hours. The data reduction was performed using the Carnegie Observatories System for MultiObject Spectroscopy (COSMOS) software package, developed by A. Oemler, K. Clardy, D. Kelson, and G. Walth and publicly available at <http://www.ociw.edu/Code/cosmos>. We used COSMOS to align slit masks, correct flat fields, subtract sky background and perform flux calibrations for IMACS data. The flux calibration stars were LTT1788 and gd71 for D1 and D4 fields, respectively. The spectral energy distribution (SED) of the standard stars were taken from Hamuy et al. (1992, 1994) and Bohlin et al. (1995). A 3σ rejection threshold was used to remove cosmic rays when stacking sub-frames from the same slit mask. 1-D spectra were extracted using an IDL program we wrote for this purpose.

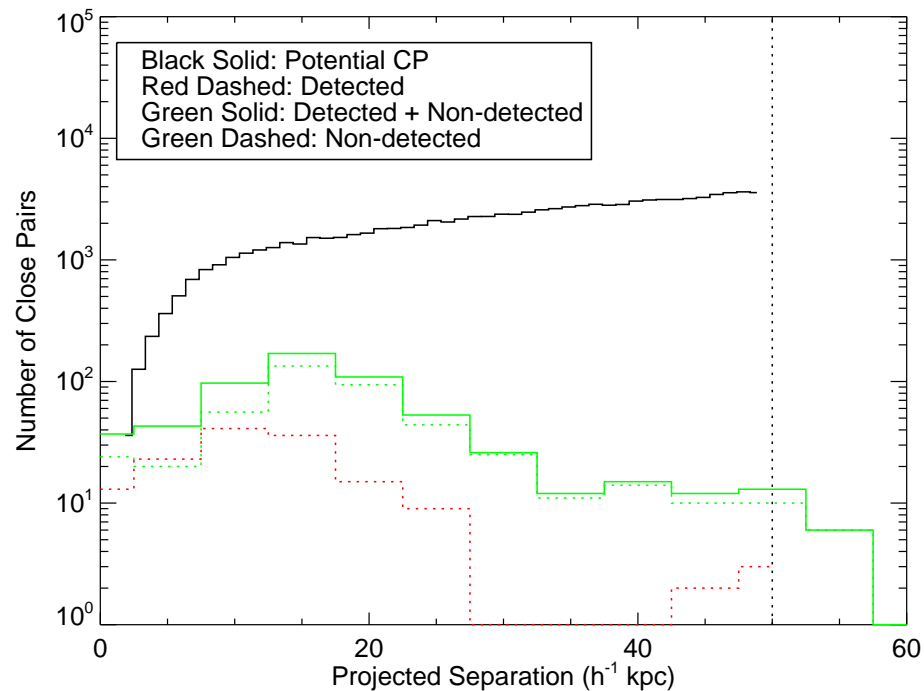


Figure 3.2 An analysis of the selection biases in our sample as a function of projected separation. The black curve represents the projected separation distribution of all the potential close pairs presented in D1 and D4 fields which satisfy the close pair selection criteria. The green solid and dashed curves represent the projected separation distribution of total and non-detected close pairs presented in this work; red dashed curve represents the projected separation distribution of detected close pairs (i.e., both pair members have confident redshift measurements, see Section 3.2.4 for more details). Note that there is a significant drop when the projected separation is greater than $20 h^{-1}\text{kpc}$ in the green and red curves, which indicates a selection bias for close pairs with smaller projected separations.

Although the vast majority of the data described in this paper comes from the Magellan Baade telescope via the SCOPIC survey, as a test of our methodology we also obtained spectra for a small sample of 20 (mainly red) close pairs in the CFHTLS D2 using the Palomar 200-inch telescope. The purpose of investigating this small sample was to verify that red galaxies are detectable using our techniques; we will occasionally refer to these Palomar observations when describing the effectiveness of our methodology of this paper, but to preserve sample homogeneity we do not include any Palomar data in our figures or analysis. These pairs were observed using the Double Spectrograph (DBSP) on the Palomar 200-inch telescope in March 2010. DBSP has a blue and a red spectrograph that work simultaneously to provide a spectral coverage of 3000 - 7000 Å for the blue camera and 4700 to 10000 Å for the red camera, respectively. The slit length of DBSP long-slit mode is 128'' and the slit width varied from 1''0 to 1''5 depending on weather conditions in order to achieve the highest S/N ratio. We used a grating with a groove density of 1200 lines/mm that yields a wavelength dispersion of 1.38 Å and 2.1 Å for 1''0 and 1''5 slits, respectively at the diffraction order $m = 1$. The blazed wavelength of the red and blue spectrographs was set to 7100 Å and 4700 Å. The individual exposure time was 10 minutes, with a total integration time of one hour per galaxy. The data reduction was done using a combination of standard IRAF routines and our own IDL code for extraction.

3.2.3 Color classification

Galaxies were classified as red or blue based on the stellar mass-dependent color selection criteria introduced in Chou et al. (2011). In this process galaxies are subdivided on the color-mass plane according to position relative to the following line:

$$(g' - i')_{\text{rest}} = -0.0076 + 0.13 \times M_{\text{stellar}} - 0.1 \quad (3.1)$$

The rest frame $g' - i'$ color is obtained from the Z-peg code fitting results. If the rest frame $g' - i'$ color of a galaxy is greater than the fiducial color defined by the line, the galaxy is classified as red, and vice versa for blue galaxies. Figure 3.1 shows the rest frame $g' - i'$ color versus the stellar mass of close pair galaxies in the D1, D2 and D4 fields. Red and blue dots represent red and blue galaxies, respectively. The black dots represent galaxies with the Spitzer Multiband Imaging Photometer for SIRTf (MIPS) 24 μm detection (down to a flux limit of 340 μJy). Cowie & Barger (2008) report that at $z < 1.5$ most red galaxies with a 24 μm flux $> 80\mu\text{Jy}$ fall into the blue cloud after the appropriate dust extinction corrections are applied. To account for the color change in dusty sources, we artificially assign the black dots with the rest frame $g' - i'$ color greater than the fiducial color to the blue cloud. Note that MIPS 24

μm observations do not include the D4 field, so the black dots on the Figure 3.1 correspond to galaxies from the D1 field only. However, there are only 10 objects in the D1 field with a MIPS 24 μm detection, which is less than 1% of the sample in the D1 field. It is reasonable to assume that the number of galaxies with MIPS 24 μm detection in the D4 field is similarly low and therefore this should not affect the overall result. After the correction for 24 μm detections, the sample is comprised of 607 red galaxies and 2143 blue galaxies. Green diamonds on Figure 1 represent close pairs where both members have spectroscopic redshift measurements.

3.2.4 Spectroscopic redshifts

Redshifts were obtained from our spectra based on emission line identifications and cross-correlation against blue and red galaxy templates. The emission line identification method is straightforward by recognizing multiple emission lines using their relative positions on the wavelength axis. The redshift is determined by fitting a Gaussian function to the identified brightest emission line. The corresponding redshift and the 1σ error can be derived from the central wavelength and the 1σ error of the fitting function. For the majority of the continuum detected galaxies, emission lines are obvious and relatively easy to identify, however in a small number ($\sim 20\%$) of cases, emission lines are hard to identify or only the continuum can be seen (e.g., very red elliptical galaxies). For those galaxies, we used the cross-correlation fitting method to determine the spectroscopic redshift by identifying absorption features. We developed an IDL program based on the package ‘C_CORRELATE’ and adopted the photometric redshift as a prior guess. To save computation time, we only considered the redshift range of $z_{pri} \pm 1.0$ (if $z_{pri} < 1$ then we start from $z = 0$). A blue and a red galaxy template generated from the stellar population synthesis code BC03 (Bruzual & Charlot, 2003) were used during cross-correlation fittings. The templates were constructed using a model that convolves a single stellar population with solar metallicity and an exponentially declining star formation history with an e-folding timescale $\tau = 1$ Gyr. The star formation cutoff time t_{cut} was set to 20 Gyr. We also applied the dust attenuation to templates using the default values in BC03 that the total effective V-band optical depth τ_V equals to 1.0 and the fraction μ of the contribution from the ambient diffuse ISM equals to 0.3, respectively. Finally, we took the SED with the age of 1.0 Gyr as the blue galaxy template, and the SED with an age of 5.0 Gyr as the red galaxy template. Since the output SEDs from the BC03 do not include the emission lines, we added emission lines artificially to the blue template based on the emission line list used in the DEEP2 survey kindly provided by Renbin Yan (private communication). The emission line widths in the DEEP2 line list were convolved to the IMACS spectral resolution before being added to the blue template.

We adopted the confidence level classification system introduced by Abraham et al. (2004) for the reliability of the spectroscopic redshifts (see Table 3.1 for definitions of the confidence levels). Class 1 corresponds to an unreliable redshift, while class 4 corresponds to a high reliable redshift. Single emission line objects require special consideration because in most cases a line is detected with certainty, but the identification of the line is uncertain. In such cases we used photometric redshifts as an auxiliary source of information, and if the inferred spectroscopic redshift is within 1σ error of the photometric redshift, we classify the object as having a high confidence redshift (class 9), otherwise we assign it a low confidence level (class 1).

Of 2750 galaxies targeted with slits, roughly half of them (1385) have redshift measurements. About 80% (1115) of these redshifts have confidence levels greater than 1, which we refer to successfully detected ones. As expected, the redshift success rate is directly related to the brightness of the galaxy, and Figure 3.3 shows our magnitude selection function (the fraction of successful redshift measurements as a function of i' -band magnitude) for the total sample and for red and blue subsets. For galaxies with an i' -band magnitude brighter than 20, the success rate for blue galaxies is more or less equal to that of red galaxies, while at fainter magnitudes ($i' > 20$ mag) the rate is on average $\sim 20\%$ higher for blue galaxies. This is understandable, as blue galaxies, having active star formation, often exhibit emission lines which are easily detected even when continuum measurements needed for absorption-line redshifts are impossible to obtain. The lower panel of Figure 3.3 shows the absolute number of galaxies in our sample as a series of histograms. The solid lines represent the total number of galaxies, while dashed lines represent the total number of galaxies with confidence levels greater than unity. The histograms show a fairly broad peak spanning $22 < i' < 24$ mag, and at this point the selection function

Table 3.1 Redshift confidence classes

Class	Confidence	Number of Galaxies	Note
Failures:			
0	None	1367	No detection.
1	< 50%	270	Only one emission/feature is detected. The emission line can not be identified even with the aid of photometric redshift.
Redshifts inferred from multiple features:			
2	> 75%	321	Reasonably secure. Redshift determined from two or more emission lines or features.
3	> 95%	327	Secure. Redshift determined from multiple emission lines/features + supporting continuum.
4	Certain	168	Unquestionably correct.
Single Line Redshifts:			
9		297	Obvious single line emission. The inferred spectroscopic redshift is consistent with the photometric redshif.

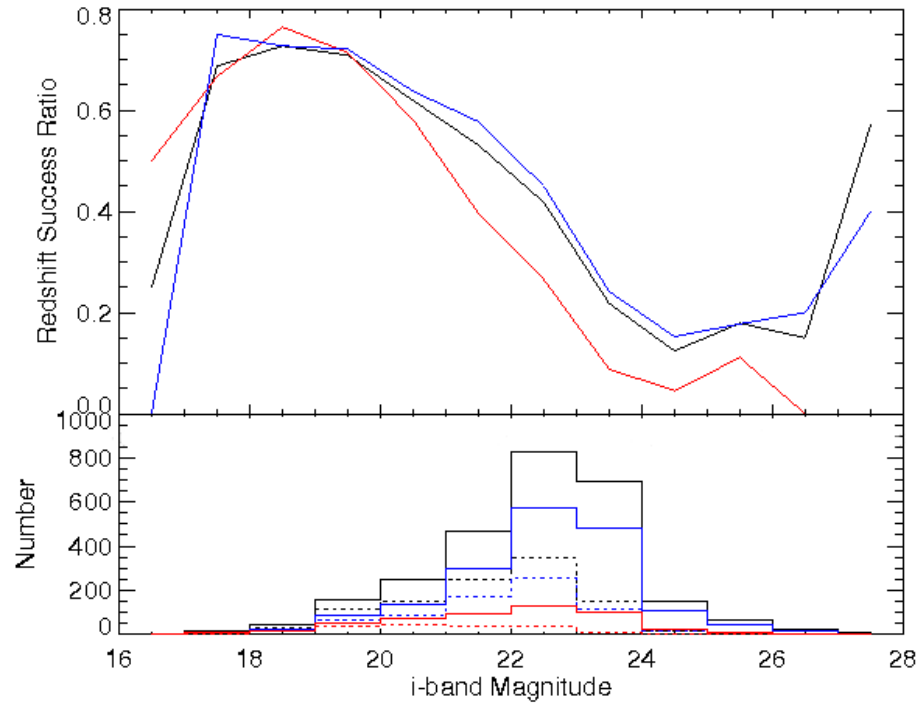


Figure 3.3 (Upper panel) Successful redshift ratio versus i' -band apparent magnitude. The black solid line shows the successful ratio for total galaxies; blue and red solid lines shows the successful ratio of blue and red galaxies, respectively. (Bottom panel) Histogram corresponding to the total, red and blue galaxies shown in black, red and blue, respectively. Solid histograms represent the total number of galaxies in different magnitude bins, while dashed histograms represent the number of galaxies with confidence level greater than 1.

corresponds to $\sim 40\%$ successful detections ¹.

In summary, we have obtained redshifts for 1385 galaxies in the range $0.1 < z < 1.2$, and 1115 of these ($\sim 80\%$) have high-confidence measurements. Table 3.1 shows the number of galaxies in each confidence level.

3.3 RESULTS

Figure 3.4 shows the relative velocity versus physical separation for all close pairs in our sample in which both members have high-confidence redshifts. The format of this figure resembles that of Figure 5 in Patton et al. (2000), but with a number of key differences, which we will now proceed to describe.

The central difference between our analysis and that of Patton et al. (2000) is that we have attempted to sub-divide pairs by the stellar populations of their member galaxies. We distinguish between ‘red-red’ pairs (systems in which both galaxies are quiescent), ‘blue-red’ pairs (systems in which one galaxy is quiescent while the other is star-forming) and ‘blue-blue’ pairs (systems in which both galaxies are star-forming). Red, green and blue colors in Figure 3.4 represent red-red, blue-red and blue-blue pairs, respectively. Since none of the galaxies presented on Figure 3.4 and Figure 3.5 have Spitzer MIPS $24\mu\text{m}$ detection, contamination of the quiescent red galaxy sample by very dusty star-forming systems is probably negligible. There are 148 pairs (exclude the biased selected D2 samples) selected on the basis of photometric redshift where both members have confident spectroscopic redshift measurements, and we will show in a moment that only around one-fifth of these turn out to be physical pairs once spectroscopic redshift and velocity information is incorporated. Among the above-mentioned 148 candidate pairs, 8 are red-red pairs, 29 are blue-red pairs and 111 are blue-blue pairs.

In addition to segregating pairs by their dominant stellar populations, Figure 3.4 also sub-divides pairs into two bins on the basis of their estimated total (*i.e.* dynamical) masses. We adopt the simplistic approach of estimating the system’s total mass by simply scaling each galaxy’s stellar mass by a constant total mass-to-stellar mass ratio of 10:1 taken by Gonzalez et al. (2007) and then summing the masses (we will describe a somewhat more refined approach later in this paper). Subdivision into high-mass and low-mass bins occurs at a total mass of $10^{12}M_{\odot}$ because, as noted earlier, this is the mass threshold predicted by the hot halo model.

¹The success rate is similar for the sample of 20 galaxies used to test our methodology with the Palomar 200-inch. Roughly half of the Palomar galaxies were not detected due to bad weather conditions, although nine pairs were observed in good weather conditions. We obtained six spectroscopically confirmed close pairs (12 galaxies) out of nine pairs (18 galaxies), which corresponds to a redshift success rate of $\simeq 70\%$. Among the six spectroscopically confirmed close pairs, one was a blue-blue pair and the remainder were red-red pairs. The members of these pairs have i' band magnitudes brighter than 20.

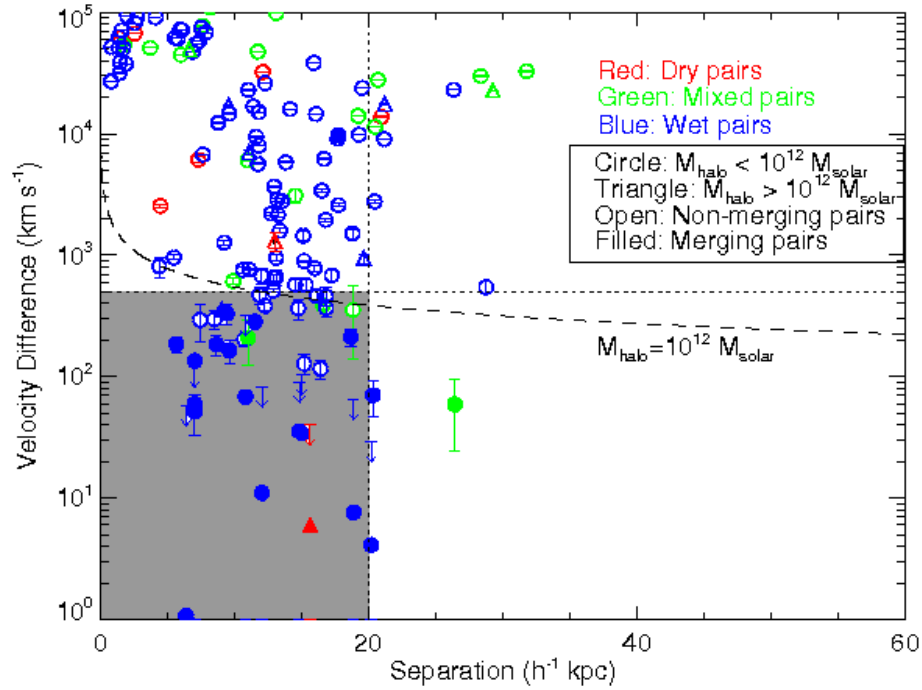


Figure 3.4 Diagram of separation versus velocity difference for close pair galaxies. Red, green and blue colors represent red-red, blue-red and blue-blue pairs, respectively. Circle and triangle symbols represent galaxies with their total halo masses smaller and greater than $10^{12}M_{\odot}$ (equivalent to a stellar mass of $10^{11}M_{\odot}$ using the stellar to total halo mass ratio of 0.1 taken from Gonzalez et al. (2007)). Filled symbols represent pairs with their separation smaller than the corresponding virial radii, which are classified as merging pairs. Two dotted lines indicate the separation of $20h^{-1}$ kpc and the velocity difference of 500 km s^{-1} . The bottom left grey corner defined by the two dotted lines shows the conventional real merging pair selection area suggested by Patton et al. (2000). The dashed lines represent the virial radius as a function of velocity difference of a system with a halo mass of $10^{12}M_{\odot}$. Before the selection of merging close pairs, there are 148 spectroscopic pair candidate (8 red-red pairs, 29 blue-red pairs and 111 blue-blue pairs on the plot). Note that none of the close pairs presented on the diagram has MIPS24 μm detection (flux limit equals to $340 \mu\text{Jy}$). After the pair selection based on the virial radius assumption using the stellar to total halo mass ratio equals to 0.1, 21 out of 148 pairs are merging pairs. The 21 selected pairs is composed of one red-red pairs, two blue-red pairs and 18 blue-blue pairs.

Circles and triangles in Figures 3.4 and 3.5 represent pairs with total halo masses less than and greater than $10^{12}M_{\odot}$.

Patton et al. (2000) note that close pairs with separations less than $20h^{-1}$ kpc and velocity differences less than 500 km s^{-1} generally show clear morphological signs of galaxy-galaxy interactions. Our own visual inspection, described earlier, concurs with Patton et al.’s impression and we therefore adopt these criteria as a useful starting point for our own more detailed analysis. Patton et al.’s limits are shown as two dotted lines on Figure 3.4, and in the present paper we will treat pairs inside these limits (the light grey region at the lower-left corner of the figure) as probable merging pairs. Figure 3.4 shows a gap at separations smaller than $5 h^{-1}$ kpc and velocity differences $\Delta v < 10,000 \text{ km s}^{-1}$. This gap finds its origin in an inevitable ambiguity that arises when distinguishing between close pairs and on-going mergers at very small separations. The former were targeted by our investigation, but the latter were not. To verify our explanation for the gap in the figures, we inspected both the two-dimensional spectra and the i' -band images of all galaxies seen at small separations, and compared them with merging systems from the sample in Bridge et al. (2010). Objects located at the upper left corner ($\Delta v > 10,000 \text{ km s}^{-1}$) of the figures correspond to physically unconnected pairs seen at small separations because of projection effects. While these objects were generally both placed on a single slit, they exhibited no obvious tidal features on the i' -band images, so that the catalog construction process and subsequent morphological classification treated them as independent galaxies.

In addition to the gap at small separations, Figure 3.4 shows a paucity of close pairs with separations greater than $20h^{-1}$ kpc. This finds its origin in the selection bias against systems with large separations described in Section 3.2.2.

If we adopt Patton et al.’s methodology, there are 31 probable merging pairs isolated in Figure 3.4. It is interesting to note that 27 of these are blue-blue pairs, three are blue-red pairs and one of them is a red-red pair. This strongly suggests that red-red mergers are quite rare at $z \sim 0.5$ (at least for close pairs with their separation smaller than $20h^{-1}$ kpc), which is consistent with the reported decline in ‘dry’ merging activity at such redshifts reported in Chou et al. (2011). To our magnitude limit, blue galaxies outnumber red galaxies by nearly a factor of four: the parent sample contains 607 red galaxies ($\sim 22\%$ of the total sample) and 2143 blue galaxies ($\sim 78\%$ of the total sample). The most conservative assumption is to assume that merging has no impact whatsoever on the colours of galaxies and that galaxies of different colour are spatially uncorrelated, in which case the colours of close pairs can simply be modelled as a binomial distribution with a 22% probability that a galaxy is red. In this case we expect the fraction of red-red pairs to be $(0.22)^2$, corresponding to a 4.8% red fraction, and therefore

we expect to see 1.5 red-red pairs amongst our sample of 31 physical pairs. This is consistent with the single detection of a red-red merging pair.

However, a legitimate criticism of the analysis presented above is that our definition for what constitutes a probable merging pair is non-unique. For example, Lin et al. (2004a, 2008) advocate a maximum separation of $50h^{-1}$ kpc rather $20h^{-1}$ kpc. If we extend our sample out to this limit, there would be one more blue-red and two more blue-blue merging pairs². Given the somewhat arbitrary nature of the limits chosen, it is worthwhile considering whether or not a more physically motivated definition for what constitutes a merging pair might not be preferable. Therefore, inspired by the idea of a halo occupation number (Lin et al., 2004b; Hopkins et al., 2010), we propose the following simple definition: **a merging pair is a system of two galaxies whose projected separation r_p is equal to or less than two times the total system's virial radius**. In other words, the pair can be thought of as sharing a common halo if $r_p < 2r_{\text{virial}}$, where $r_{\text{virial}} = GM/V^2$, and G represents the gravitational constant, M represents the total halo mass of the system and V represents the 3D relative velocity of the two pair members. Since the actual 3-D relative velocity is not available, we must multiply line-of-sight velocity differences by a factor of $\sqrt{3}$ as a statistical correction when computing r_{virial} from redshifts³.

For reference, the virial radius of a system with a total mass of $10^{12} M_{\odot}$ and a velocity difference of 500 km s^{-1} is $12 h^{-1}$ kpc. The dashed curve in the figure maps variation of virial radius as a function of velocity difference for a system with the halo mass of $10^{12} M_{\odot}$. In our approach any system with a total mass of $10^{12} M_{\odot}$ would be considered a merging pair if it lies anywhere below this curve. We applied this methodology to systems of all masses by assuming a certain total mass-to-stellar mass ratio, and in Figure 3.4 we flag merging pairs determined in this manner using filled symbols. Using this approach, 21 systems (around 65% of the pairs in the boxed region at the lower-left corner of Figure 3.4) are found to be merging. One of these is a red-red system and two pairs are blue-red systems, but 18/21 (86%) of the pairs are blue-blue systems.

A criticism that can be directed at Figure 3.4 is its heavy reliance on a uniform stellar-to-total mass ratio in order to infer virial radii. As described earlier, the total masses (and hence virial radii) used to construct Figure 3.4 have been computed using the rather simplistic

²It is worth recalling that the Milky Way is about 750 kpc from M31 with a velocity difference of about 120 km s^{-1} (Karachentsev et al., 2004; de Vaucouleurs et al., 1991). Even though our ultimate destiny seems to be to merge with the Andromeda galaxy, the present configuration of the Local Group would not result in the Milky Way + M31 system being flagged as a merging pair by any of the criteria adopted here.

³The factor of $\sqrt{3}$ is obtained by assuming an isotropic velocity difference distribution, so that the relationship between the pairwise velocity V its components V_x, V_y and V_z can be simply expressed as $\sqrt{3}$ times the line-of-sight velocity: $V = \sqrt{V_x^2 + V_y^2 + V_z^2} = \sqrt{3V_z^2} = \sqrt{3}V_z$.

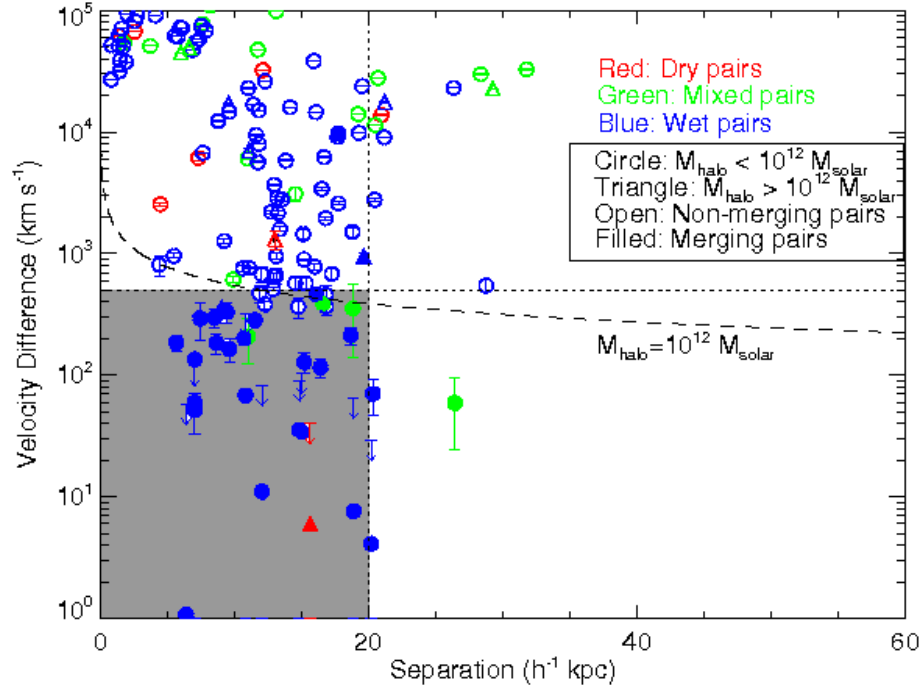


Figure 3.5 Diagram of separation versus velocity difference for close pair galaxies using different stellar to total halo mass ratios taken from Leauthaud et al. (2011). This figure is presented in the same way as Figure 3.4. It is clear that the number of filled symbols increases, and most of them are still located within the conventional merging pair selection area. After the application of different stellar to halo mass ratios, 30 out of 148 are classified as merging pairs. One of them are red-red pairs, four of them are blue-red pairs and 25 of them are blue-blue pairs. Table 3.2 summarizes the number of pairs selected by different criteria.

Table 3.2 Summary of three types of close pairs selected using different criteria.

criteria	$r_p < 20h^{-1}\text{kpc}$ $\Delta v < 500\text{kms}^{-1}$	$r_p < 2r_{virial}$ (Gonzalez et al. (2007))	$r_p < 2r_{virial}$ (Leauthaud et al. (2011))
Red-red Pairs	1	1	1
Blue-red Pairs	3	2	4
Blue-blue Pairs	27	18	25
Total	31	21	30

approach of assigning a total mass to a composite system by assuming a constant total mass-to-stellar mass ratio of 10:1. This commonly-adopted (Conroy et al., 2007; Spitler et al., 2008) total mass to stellar mass ratio is taken from Gonzalez et al. (2007), who derived it from galaxy groups and clusters with total halo masses $\geq 10^{14}M_{\odot}$, which are about two orders of magnitude more massive than the total masses of the systems in our sample. Naturally, other measurements of the total mass-to-stellar mass ratio can be found in the literature (for example Conroy et al. 2007, Giodini et al. 2009, Leauthaud et al. 2010) but most such work focuses either on limited classes of objects (e.g. early type galaxies; Heymans et al. 2006) or on composite systems with masses higher than $10^{13}M_{\odot}$ (Mandelbaum et al., 2006).

Fortunately, statistical analyses of stellar-to-total mass ratios based on weak lensing are now beginning to emerge, and these can better inform our analysis, by allowing us to incorporate a total-to-stellar mass ratio that is a function of stellar mass. Table 3.2 summarizes the number of pairs selected by adopting a variable total-to-stellar mass ratio using the weak-lensing based results presented by Leauthaud et al. (2011), and provides a comparison with the other methods we have described. We emphasize that weak-lensing measurements are constructed from large samples in the appropriate mass range for our purposes, but at present such investigations are independent of galaxy morphology. The results presented Leauthaud et al. (2011) are based on COSMOS imaging data (Scoville et al., 2007) coupled to follow-up spectroscopic redshifts from the zCOSMOS survey (Lilly et al., 2007). In Figure 3.5, we incorporate these data in attempt to improve upon Figure 3.4. The format of Figure 3.5 is identical to that of Figure 3.4, except that non-constant stellar-to-total mass ratios have been used to infer the virial radii. As a result, there are 31 physical pairs out of 148 pairs shown in Figure 3.5 and again we flag merging pairs using filled symbols. Leauthaud et al. (2011) probes systems with halo masses down to below $10^{11}M_{\odot}$, making this an excellent fit to our sample. However, it should be emphasized that weak lensing analyses are fairly new and subject to a large number of subtle systematics, so some caution should be used in the interpretation of Figure 3.5. We suspect that Figure 3.5 is likely to have more long-term value than Figure 3.4, but the latter provides a robust backstop against which Figure 4 can be compared.

3.4 DISCUSSION

3.4.1 Abundance of physical pairs

A comparison of Figures 3.4 and 3.5 makes it clear that the use of a non-constant mass-to-light ratio based on weak lensing data results in an increase in the number of physical pairs. This is because the typical total-to-stellar mass ratios for galaxy-scale halos are much higher than the corresponding value for groups or clusters, so the derived virial radii are also larger. In Figure 3.5 one physical pair is a red-red system, four physical pairs are blue-red systems, and 25 physical pairs are blue-blue systems. Although red-red pairs are clearly rare, their absence is not due to our experimental design: when we augmented the IMACS data with Palomar observations purposely designed to find red-red systems with our technique, we did find them: the Palomar observations resulted in five red-red pairs and one blue-blue pair, and the redshift success rate is consistent with that of IMACS observations⁴.

Overall, 30 out of 148 spectroscopic pair candidate pairs presented in Figure 3.5 turn out to be physical pairs. While the majority of these occupy the light grey region in the diagram which Patton et al. (2000) suggest corresponds to systems with clear indications of tidal disturbance, around 10% of the physical mergers lie outside this region. These are typically pairs with one rather massive galaxy (resulting in a total system halo masses greater than $10^{12} M_{\odot}$, denoted by the triangle symbols in Figure 3.5), although two are pairs with relatively low velocity differences but larger separations. The latter galaxies would likely be missed by the traditional close pair selection methods for identifying physical merging pairs, since it would be rather risky to select merging pairs by simply selecting on the basis of higher velocity differences or larger separations, which would result in many false detections. It is also interesting to note that we find a number of systems ($\sim 15\%$) that are unlikely to be physical pairs even though they are located in the bottom left corner of Figure 3.5. These are likely to be ‘false positives’ inferred using the Patton et al. (2000) methodology, and these systems emerge because their halo masses are low, resulting in small virial radii. Of course our method has false positives of its own: since the velocities used in our analysis are line-of-sight, and therefore a combination of projected galaxy peculiar velocities and cosmological redshifts, some fraction of these pairs are likely to have true separations of several Mpc and are unlikely to merge. Such false positives are inevitable in any physical pair selection technique, and the net result is that the number of close physical close pairs is likely to be slightly over-estimated.

⁴We again emphasize that Palomar observations are not included in the summary statistics presented in this paper (e.g. in any of the discussion below) since they were intentionally biased and mainly useful for testing our methodology.

It is worthwhile to consider the ultimate fate of the physical pairs identified in the present survey. We assume that they will all eventually merge and become single systems. However, as noted in the Introduction, the timescale over which this will occur is far from certain, and the question of whether mergers trigger or suppress star-formation remains open. We will have more to say about this later in the discussion in the context of the Hot Halo model, but for now it is worthwhile to point out that Figure 3.5 reveals a rather striking discrepancy in the fraction of red-red ‘pairs’ that are likely to be line-of-sight optical superpositions, relative to the number of physical red-red pairs. This is clearly seen even if one simply uses the straightforward definition for a physical merger suggested by Patton et al. (2000), and compares the fraction of pairs that are red-red systems inside the box ($\sim 1\%$) to the corresponding fraction (5%) of pairs that are red-red systems in regions of the diagram that are outside the box.

3.4.2 Comparison with DEEP2 and VVDS Surveys

Because the overall completeness of our survey (shown in Figure 3.2) is relatively low, we have mainly focused on making *relative* comparisons between the properties of physical pairs and field galaxies, since the photometric and spectroscopic selection criteria for the two populations are the same. However, it is worthwhile giving some consideration to the absolute numbers of objects seen, with the merger rate density of close pairs obtained from other surveys. Comparison with results from a merger analysis of the DEEP2 survey (Lin et al., 2008) is particularly interesting, because these authors also selected close pairs based on dynamical criteria (i.e., separations $< 30h^{-1}$ kpc and velocity difference $< 500 \text{ km s}^{-1}$)⁵.

The present IMACS survey’s co-moving volume is two square degrees over a redshift range of $0.1 < z < 1.2$, which corresponds to $1.1 \times 10^7 \text{ Mpc}^3$. Using the merger rate density of $\sim 1.0 \times 10^{-3} h^3 \text{ Mpc}^3 \text{ Gyr}^{-1}$ (where $h = 0.7$) and a merging timescale of 0.5 Gyr for all pairs taken from Figure 7 in Lin et al. (2008), one expects $\simeq 1900$ close pairs in our survey volume. Figure 3.5 shows that our survey contains 31 physical pairs. While this number seems low, in fact it matches our expectations based on the selection criteria presented in Figures 3.2 and 3.3. In Figure 3.3, near the peak of the galaxy count distribution at around $i \sim 22.5$ mag the spectroscopic completeness is around $\sim 40\%$ for an individual galaxy, and this should be squared to compute the pairwise completeness (as a first order approximation, to account for the fact that we require successful redshifts for both galaxies in the pair). So the overall spectroscopic completeness of galaxies targeted with slits is around 16%. This must in turn be multiplied by the sparse sampling completeness factor which accounts for the fact that only a

⁵Note that the maximum separation of close pairs selected in the DEEP2 survey is $10h^{-1}$ kpc larger than the projected distance selection criterion used in this work.

subset of galaxies was targeted with a slit. In Figure 3.2 we see that the ratio of the parent sample to the observed sample is roughly 10:1 for potential pairs with separations smaller than $20h^{-1}\text{kpc}$. Therefore, our 31 physical pairs maps to $31/0.16 \times 10 = 1937$, which is in good agreement with the expected $\simeq 1900$ physical pairs predicted from the merger rate density of the DEEP2 survey.

Our main conclusion (that dry mergers are rare at intermediate redshifts) has been foreshadowed by Lin et al. (2008), using the data from the DEEP2 Survey. These authors report that the red-red pair merger rate density within the redshift range $0.2 < z < 1.2$ is $\sim 1.0 \times 10^{-4} h^3 \text{Mpc}^{-3} \text{Gyr}^{-1}$ with the merging timescale of 0.5 Gyr. Using this red-red pair merger rate density and a merging timescale of 0.5 Gyr, we can estimate the number of red-red pairs predicted from the DEEP2 survey result given our IMACS survey volume. Again using the IMACS survey volume noted earlier of $1.1 \times 10^7 \text{Mpc}^3$, we would expect $(1.0 \times 10^{-4} h^3 \text{Mpc}^{-3} \text{Gyr}^{-1}) \times (0.5 \text{Gyr}) \times (1.1 \times 10^7 \text{Mpc}^3) \sim 190$ red-red pairs if our survey had placed a slit on every available galaxy and extracted redshifts with 100% completeness. As we have already shown, the two completeness correction factors encapsulated by Figures 3.2 and 3.3 can be used to map this expectation into an observed number of pairs in our survey. For red galaxies, our redshift completeness is 25% at $i' \sim 22.5$ mag, and as noted before this should be squared to compute the pairwise completeness and this then must be multiplied by the inverse of our sampling completeness. Therefore our single detection of red-red close pair translates to $1/0.06 \times 10 \simeq 160$ pairs after applying the completeness correction factors, which is consistent with the number of predicted red-red pairs obtained from the DEEP2 survey.

Some of our conclusions can also be tested using published results from the VIMOS VLT Deep Survey (VVDS) (de Ravel et al., 2009). These authors provide a set of 36 spectroscopically confirmed physical pairs with separations $r_p < 20h^{-1} \text{kpc}$ and velocity differences $\Delta v < 500 \text{km s}^{-1}$. The fraction of pairs corresponding to early type galaxies is $\sim 8\%$, which is significantly lower than the fraction (25%) estimated when the pair criteria are expanded to separations up to $r_p = 100h^{-1} \text{kpc}$. Evidently, most of the red-red pairs in the sample are seen at larger separations.

3.4.3 Damp vs. Dry Mergers

Based on the analysis presented in the previous section, we conclude that there is a high degree of consistency in the predicted number of *early-stage* mergers (with their separations smaller than $20h^{-1} \text{kpc}$) seen in our pair analysis data, compared with the published space densities for such systems. It is less clear that the *late-stage* mergers probed by morphological studies (e.g. that of Chou et al. 2011) are also consistent with these numbers, given the very high-fraction

(> 50%) of nearby late-stage mergers that are red.

Why are so many nearby late-stage mergers red? A possible solution might be the existence of a short-lived star formation epoch during the early merging stage. In this scenario, some galaxies in the field are not truly ‘dry’ nor truly ‘wet’, since they still contain a small amount of gas (Rampazzo et al., 2005; Crocker et al., 2012). When two galaxies interact at the close pair stage, a small amount of star formation is triggered by tides, which makes at least one of the galaxies appear blue. This nascent star-formation period must be fairly transient, since during the late-phase of the merger the remnant must become red in a short period of time (of order the merging timescale, ~ 0.5 Gyr). The result is a relatively high number density of dry mergers despite a paucity of red-red pairs. This begs the question: what combination of physics might result in weak tides that trigger star-formation, along with other processes that truncate it? One possibility is a combination of tidally-induced merging coupled with the hot halo picture, as discussed in §3.4.4 below. However, before describing this idea further, we must first consider the precise definition of a dry merger, both in our paper and in the literature.

In this context, it is interesting to consider how the rest-frame ($g' - i'$) color selection threshold we have used to define our red galaxy sample compares with the colour-selection criteria adopted in other papers that also probe ‘red mergers’ at intermediate redshifts. Our ($g' - i'$) colour threshold has relatively little sensitivity to contributions made by young stellar populations, so it is particularly interesting to compare our work to Lin et al. (2008) [hereafter Lin08], who used a ($u - b$) color threshold, and van Dokkum (2005) [hereafter vD05], who used a ($b - r$) color threshold, to define their red populations. To inter-compare the surveys, we can use spectral synthesis models to investigate how much additional star-formation is needed in order for an underlying old stellar population to no longer meet the red galaxy color-selection thresholds used in each of these papers. We used the BC03 code (Bruzual & Charlot, 2003) to construct spectral energy distributions comprised of a dominant very old stellar population polluted by star-formation from a very young stellar population. The stellar mass of the template galaxy was fixed to a stellar mass of $5 \times 10^{10} M_{\odot}$. Both stellar populations were modelled using exponential star-formation histories with an e-folding timescale of 1 Gyr and a foreground-screen dust extinction model with $\tau_V = 1.0$. The ages for the old and the young stellar populations were fixed at 10 Gyr and 0.1 Gyr, respectively, and we varied the stellar mass fraction between the old and the young populations before measuring the corresponding broad band colors. Our analysis shows that the ($g' - i'$) color threshold used in the present paper is rather liberal — a 10% contribution to the total mass is needed from the young stellar population in order to exceed our colour threshold. In contrast to this, the ($u - b$) color threshold used by Lin08 can accommodate a $\sim 1\%$ young stellar population, and the

$(b - r)$ color threshold used by vD05 can accommodate essentially no young stellar population ($< 1\%$). This also implies that these early type galaxies may not be completely dry. While it is a mistake to assume that morphological characteristics uniquely map onto particular stellar populations, we suspect that our red galaxy sample is likely to be comprised of a combination of elliptical galaxies and early-type spirals, while the Lin08 and vD05 samples are probably dominated by pure ellipticals. And if the Lin08 and vD05 studies are of ‘dry mergers’, our study is mainly made of systems better described as ‘damp mergers’. However, it is worth noting that a non-negligible fraction of the red galaxies presented in vD05 exhibit excesses in 8 and $24\mu\text{m}$ bands (Desai et al., 2011), which suggests that at least some of these objects are star-forming. Putative early type galaxies may appear to be almost dry using rest-frame visible color selection criteria, but they may not be completely dry and/or may be undergoing gas rich minor mergers (Desai et al., 2011). The present paper shows that even damp mergers are quite hard to find, so the truly dry mergers must be remarkably rare.

3.4.4 Implications for the Hot Halo Model

We conclude this section by noting the constraints placed on the hot halo quenching model by our results. As noted in the Introduction, in the hot halo quenching model systems with halo masses greater than $10^{12}M_{\odot}$ shock-heat infalling gas within the virial radius, so star-formation is quenched. We have estimated the halo masses of all physical pairs, and are able to subdivide our physical pair sample into two groups, with halo mass greater than and less than $10^{12}M_{\odot}$, and denote these with different symbols in Figures 3.4 and 3.5. These figures show no significant evidence for an enhancement in the fraction of red pairs with their projected separations smaller than $20h^{-1}$ kpc in the high-mass group. Indeed, as noted earlier, red-red pairs are simply rare at all masses, and there is an excess of blue systems, again at all masses, relative to the field. Rather than being quenched, it seems that star formation is enhanced by galaxy-galaxy interaction at the close-pair (early stage merger) phase. This begs the following question: why is there so little evidence for shock-induced star-formation quenching in our data, given the abundance of red late-stage mergers reported by Chou et al. (2011)? It is possible that the quantity of gas flooding into a potential well in a merger is sufficiently large that shocks are inefficient until the merger is nearly complete. The crossing timescale of a close pair is only ~ 60 million years, and it may be difficult to increase the gas temperature in such a short time period by gravitational heating. This admittedly rather vague suggestion does hint at the possibility that timescales do matter, so that the degree of shock-induced quenching might depend strongly on the phase of the merger being witnessed. Testing this intriguing idea will require a much larger sample than that used in the present paper.

Another possible explanation is that the gas in these interacting galaxies is not falling into the pair’s dark matter halo; instead, it is already present in the halo, and quite likely being accreted onto the central regions of one or both galaxies, as predicted by simulations (Mihos & Hernquist, 1994; Di Matteo et al., 2007) and seen observationally (Barton et al., 2000; Ellison et al., 2011)

3.5 CONCLUSIONS

We have obtained spectra for ~ 2800 candidate close pair galaxies at $0.1 < z < 1.2$ identified from the Canada-France-Hawaii Telescope Legacy Survey fields. Spectra of these systems were obtained using the multi-object spectrograph IMACS on the 6.5m Magellan and DBSP on the 5m Hale telescopes. These data allow us to constrain the rate of dry mergers at intermediate redshifts and to test the ‘hot halo’ model for quenching of star formation. Redshifts were obtained for $\sim 50\%$ of the galaxies in our sample (1385 galaxies), and $\sim 80\%$ of the redshift measurement (1115 galaxies) have confidence levels greater than unity. Because confirmation of physical pairs requires successful high-confidence redshifts for both galaxies in the pair, in the end we are left with 148 close pair candidates (296 galaxies). We used virial radii estimated from the correlation between dynamical and stellar masses published by Leauthaud et al. (2011) as a reference to select physically merging systems from this sample, based on halo occupation. We find that around 1/5 of our candidate pairs (31 pairs) are physically associated and share a common dark matter halo. These pairs are divided into red-red, blue-red and blue-blue systems using rest-frame $g' - i'$ colors, using the classification method introduced in Chou et al. (2011). After correcting for known selection effects, the fraction of blue-blue pairs is significantly greater than that of red-red and blue-red pairs. Given a fairly liberal rest-frame color selection criteria in selecting red galaxies, red-red pairs are almost entirely absent from our sample, suggesting that red early-phase mergers are rare at $z \sim 0.5$. This result is consistent with that obtained from the DEEP2 survey (Lin et al., 2008). Our data supports models with a short merging timescale (< 0.5 Gyr) in which star-formation is enhanced in the early phase of mergers, but quenched in the late phase of mergers. Hot halo models may explain this behaviour if virial shocks that heat gas are inefficient until the merger is nearly complete.

Chapter 4

Optical Designs of the Wide Integral Field Infrared Spectrograph

Part of the material presented in this chapter has been published in an SPIE conference proceeding, 2010, vol 7735E, pp223

4.1 INTRODUCTION

In this chapter, I present two versions of the optical designs of the Wide Integral Field Infrared Spectrograph (WIFIS) that can provide unprecedented combinations of etendue and spectral resolving power: I call the two designs WIFIS1 and WIFIS2. Both WIFIS1 and WIFIS2 provide an integral field of $\sim 12'' \times 5''$ on a 10-m telescope (or equivalently $52'' \times 20''$ on a 2.3-m telescope.)¹ WIFIS1 has spectral resolving powers $R \sim 5,500$ covering each of the NIR JHK band separately with three gratings; WIFIS2 does $R \sim 3,000$ with the spectral coverage of zJ (0.9–1.3 μm) or H band (1.3–1.8 μm) separately with two gratings. Due to different spectral resolving powers and spectral coverages provided by two WIFIS designs, WIFIS1 and WIFIS2 are targeting at different science goals mainly focusing on studying kinematics and chemistry of extended objects. One of the primary science targets of WIFIS is redshifted $H\alpha$ line emission from merging galaxies or star-forming galaxies at the redshift ranges of $z \sim 1.5$ (for WIFIS1) and $z = 0.4$ –1.0 (for WIFIS2). Figure 4.1 shows an image of a typical galaxy merger NGC 2623 overlaid with the WIFIS integral field, showing an excellent agreement between the size of the

¹WIFIS will have chance to start its commissioning on the 10-m Gran Telescopio Canarias (GTC) in Spain in the near future. As a first step, WIFIS will start its commissioning on the 2.3-m Bok telescope at the Kitt Peak Observatory in Arizona, US. Therefore, throughout this chapter, the integral FOV of WIFIS is given with respect to 10-m and 2.3-m telescopes.

merging galaxy and that of the WIFIS integral field. Other scientific targets of WIFIS include nearby star-forming regions, supernova remnants, and local galaxies (see §4.6 for more details).

The primary principle on which the WIFIS optical designs are based is to achieve a combination of the largest integral fields and the maximum spectral resolving powers using the most of the detector pixels of the state-of-art Hawaii II RG (H2RG) $2K \times 2K$ array. For spectroscopy, the spectral resolving power (R) is defined as:

$$R = \frac{\lambda}{\delta\lambda} \quad (4.1)$$

where $\delta\lambda$ is the spectral resolution element (= projected slit width on the detector). The spectral resolution element and the spectral coverage ($\Delta\lambda$) for slit-based spectroscopy is then related as

$$\delta\lambda = \frac{\Delta\lambda n}{N} \quad (4.2)$$

with the number (n) of detector pixels per the resolution elements and the total number (N) of detector pixels in the dispersion direction. As a result, we obtain

$$R = \frac{\lambda}{\delta\lambda} = \frac{\lambda N}{\Delta\lambda n} \quad (4.3)$$

where, for a fixed N , $\Delta\lambda$ is inversely proportional to R and n . Assuming the Nyquist sampling rate, which requires a minimum number of two pixels per spectral resolution element to sufficiently sample the spectral resolution element², and $0.3 \mu\text{m}$ spectral coverage for each of the JHK bands, the above relation gives the maximum spectral resolving power $R \simeq 5,500$ for $N = 2,048$, such as the H2RG array. Alternatively, this corresponds to the maximum spectral resolving power $R \sim 2,800$ for the combination of the zJ ($0.9 - 1.3 \mu\text{m}$) band. The two WIFIS optical designs were made to satisfy these two cases: WIFIS1 for $R \simeq 5,500$ for JHK bands; WIFIS2 for $R \simeq 2,800$ for zJ and H bands. The etendue of WIFIS, on the other hand, is mainly determined by its IFU, and, as described in detail in §4.2.1, it provides the maximum integral field size obtainable with a detector of 2,048 pixels in the spatial direction under natural seeing conditions.

Table 4.1³ summarizes the spectral resolving powers and integral field sizes, along with the entire spectral coverage of NIR IFSs currently employed on large telescopes; Figure 4.2 compares their etendues times the corresponding average throughput and spectral resolving powers.

²Strictly speaking, the Nyquist sampling requires a bandlimited function and in the case of time limited spectroscopy observations this is not quite true. The application of the Nyquist sampling on a time limited function usually causes aliasing. However, since the spectral resolution element is sampled by a few pixels (in the case of WIFIS is two pixels), each pixel serves as a low-pass-filter that significantly alleviate the effect of aliasing. Therefore, our approach by locating two pixels in a single resolution element remains a good approximation.

³The integral field size of KMOS presented in the Table 4.1 is for a single IFU, the actual integral field size of KMOS is sustained by 24 IFUs. SPIFFI works with the AO system SINFONI to provide high spatial resolutions. Although in the largest FOV ($8'' \times 8''$) mode, it is recommended to observe under natural seeing conditions due to the plate scale is comparable to the spatial resolution provided by the AO system.

Table 4.1 Summary of important specifications of IFSs in NIR on large telescopes.

Instrument / Adaptive Optics	Telescope	Average Throughput	Spectral Resolving Power	Integral Field Size	Spectral Coverage (μm)
NIFS/Altair	Gemini 8-m	17%	5,300	$3'' \times 3''$	0.94 – 2.50
OSIRIS/KECK AO	Keck 10-m	9%	3,900	$4''.8 \times 6''.4$	1.0 – 2.4
SPIFFI/SINFONI	VLT 8-m	25%	3,000	$8'' \times 8''$	1.0 – 2.45
SPIFFI/SINFONI	VLT 8-m	25%	4,000	$0''.8 \times 0''.8$	1.0 – 2.45
KMOS/None	VLT 8-m	26%	3,800	$2''.8 \times 2''.8$	0.8 – 2.5
PIFS/None	Palomar 5-m	23%	1,300	$5''.5 \times 9''.5$	1.0 – 2.5
WIFIS1/None	10-m class	25%	5,500	$12'' \times 5''$	1.14 – 2.36
WIFIS2/None	2-m class	25%	3,000	$52'' \times 20''$	0.9 – 1.8

Compared with other NIR IFSs, both WIFIS1 and 2 provide the largest product of etendue and throughput, while they have comparable spectral resolving powers. For example, currently the largest etendue-throughput combination achieved by other IFSs is the $8'' \times 8''$ integral field size and 8-m aperture size with the average throughput of $\sim 25\%$ (or $800 \text{ arcsec}^2 \text{ m}^2$) from SINFONI/SPIFFI on the VLT telescopes. Hence, WIFIS, when built, will provide a larger etendue-throughput combination (i.e., $1,175 \text{ arcsec}^2 \text{ m}^2$) with better (for WIFIS1) or comparable (for WIFIS2) spectral resolving powers. Note that SINFONI has $R \simeq 3,000$ spectral resolving powers.

4.2 WIFIS Optical Designs and Systems

WIFIS optical system is composed of the following five main components: (a) a re-imaging unit comprises a pair of off-axis parabolas (OAPs); (b) an IFU called "FISICA" standing for *Florida Image Slicer for Infrared Cosmological and Astrophysics*; (c) a collimator; (d) a grating based dispersing unit; and (e) a spectrograph camera followed-by a H2RG detector. Figure 4.3 presents projected layouts of the WIFIS optical systems: WIFIS1 and WIFIS2 have similar optical configurations. The linear dimensions of WIFIS1 and WIFIS2 optical systems are $\sim 1.4 \text{ m} \times 0.8 \text{ m}$ and $0.8 \text{ m} \times 0.8 \text{ m}$, respectively.

4.2.1 Re-imaging Unit and Integral Field Unit

As shown in Figure 4.3, the first component of the WIFIS optical systems is a re-imaging unit comprising a pair of OAPs which converts (or just transfers) an input beam from a telescope

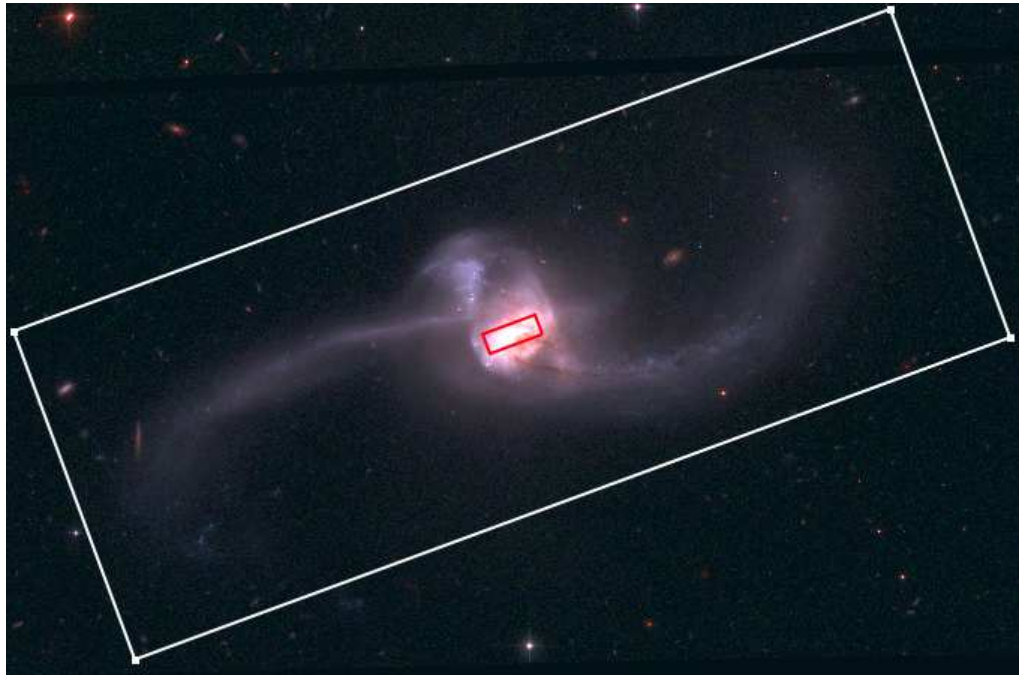


Figure 4.1 An optical color composite image of a nearby major merger NGC 2623 taken by the Hubble Space Telescope. The intensity is shown in logarithmic scale in order to reveal low surface brightness features. The central red rectangle indicates the WIFIS integral field of view of $12'' \times 5''$, which can cover the central kilo-parsec region of the merger. The big white rectangle indicates the $12'' \times 5''$ WIFIS integral field of view if this galaxy merger was at redshift $z = 0.5$. This picture demonstrates the benefits of the large etendue affordable by WIFIS when observing merging galaxies at different redshifts.

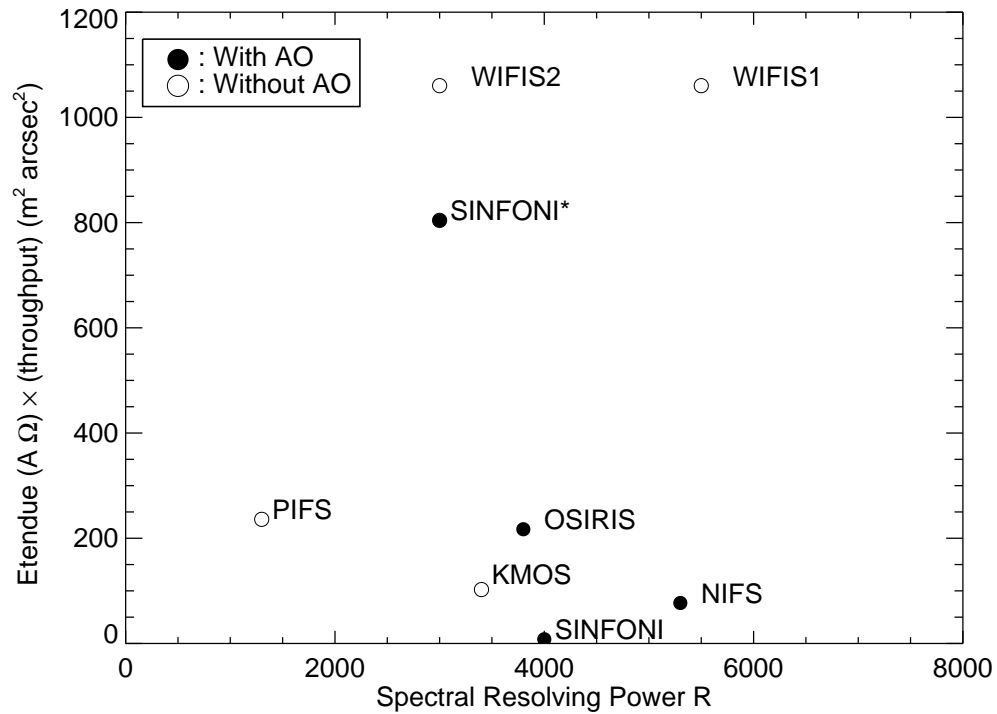


Figure 4.2 Etendue times throughput versus spectral resolving powers for IFSs listed in Table 4.1. Filled circles represent IFSs work with an adaptive optics system, and open circles represent IFSs operate under natural seeing conditions. WIFIS is designed to operate under natural seeing conditions and can offer incomparable etendue-throughput as well as higher or comparable spectral resolving powers. Note that the data point of the K-band Multi-Object Spectrograph (KMOS) represents the etendue for one IFU only, the full integral field of KMOS is sustained by 24 IFUs.

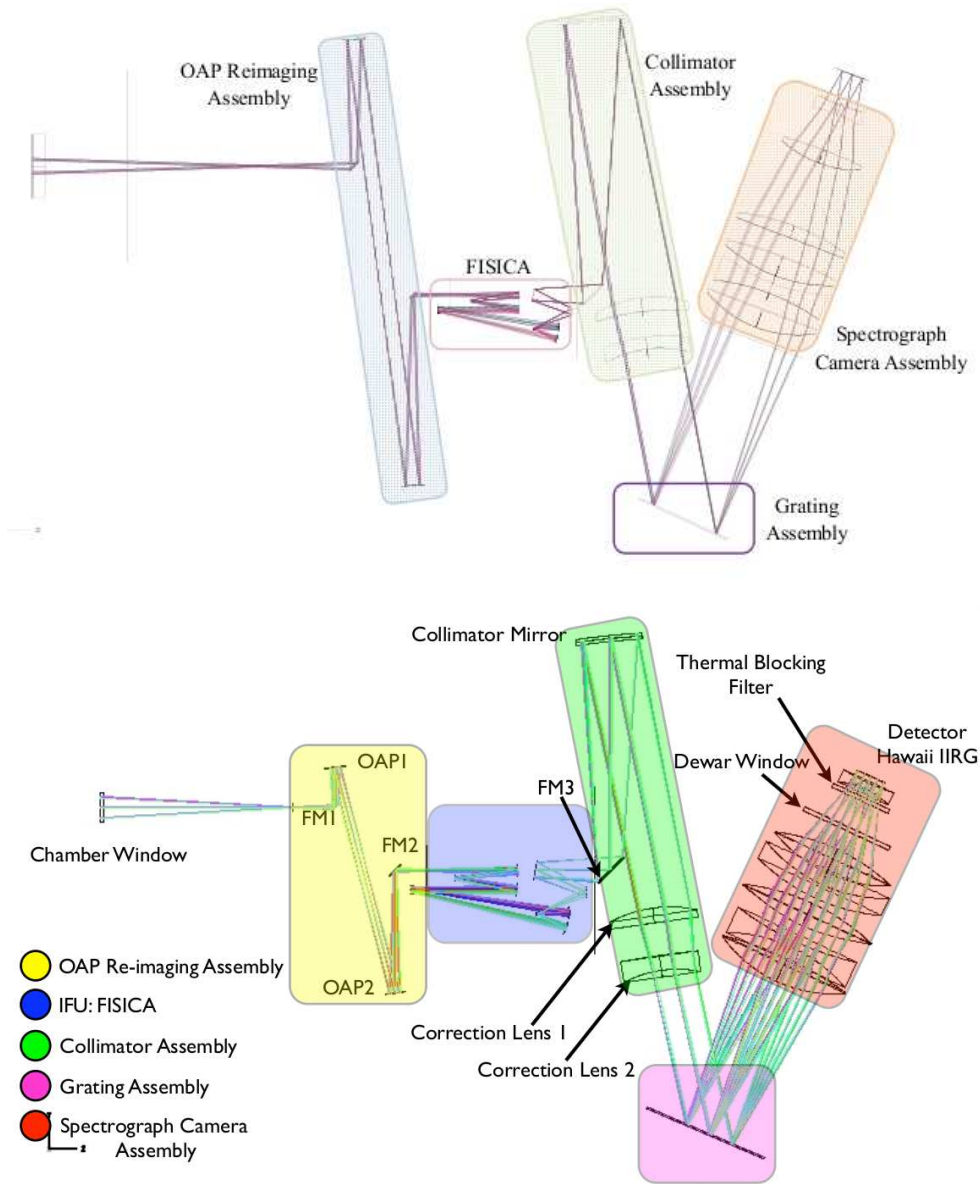


Figure 4.3 Top panel: Optical layout of the WIFIS1 design. At the left hand side, light from the telescope goes through the OAP re-imaging unit. The re-imaging unit converts the telescope focal ratio to $f/16$ for the following IFU FISICA. FISICA decreases the input focal ratio by a factor of two and produces a pseudo long-slit. The output pseudo long-slit will be collimated, dispersed and focused by the collimator system, the gratings and the spectrograph camera. Bottom panel: Optical layout of the WIFIS2 design. Basically WIFIS2 share the same configuration of WIFIS1 but with a smaller collimated beam. The dimension of WIFIS1 and WIFIS2 design is $\sim 1.4 \times 0.8$ meters and 0.8×0.8 meters, respectively.

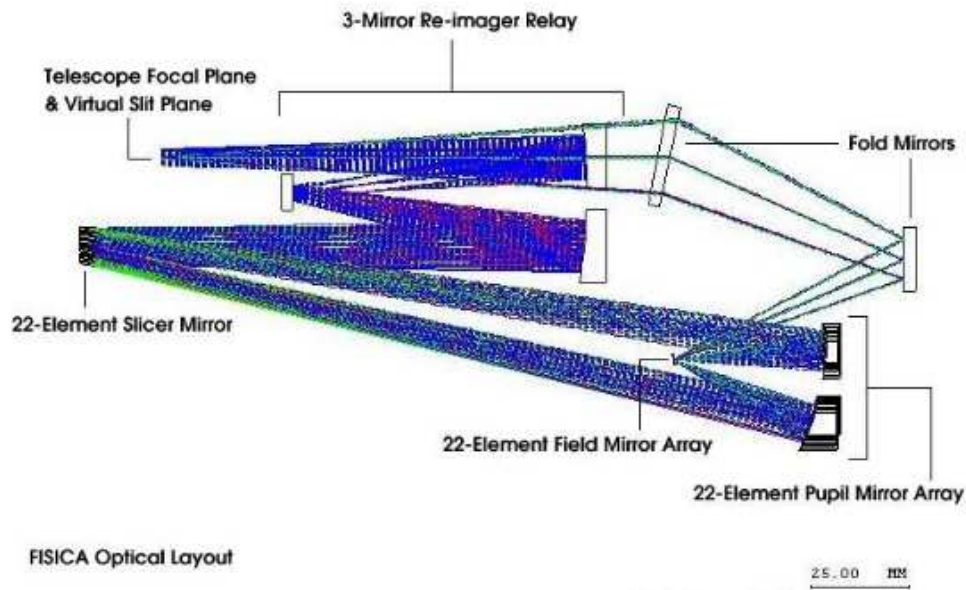


Figure 4.4 Optical layout of FISICA taken from Eikenberry et al. (2004). An $f/16$ input beam from the re-imaging unit is focused by the 3-mirror re-imager relay onto the slicer array. The slicer array delivers the sliced images to the 22-element pupil array and then the 22-element field array. The image of the pseudo long-slit from the field array is delivered by the two fold mirrors to the output position of FISICA. Note that to emphasize the fact that the optics behind FISICA will actually ‘see’ the pseudo long-slit originates from the telescope focal plane, rays arrive the second fold mirror are traced inversely rather than go to the real output position on the right hand side.

into an $f/16$ output beam to the following FISICA IFU. (Note that FISICA is optimized to work with an $f/16$ input beam; see below.) The first OAP mirror collimates an input beam and creates a pupil location before the second OAP mirror, providing an ideal location for a cold stop and/or order-blocking filters; while the second OAP mirror re-images the collimated beam onto FISICA. Telescopes of different focal ratios require different combinations of OAPs.

FISICA, which serves as the WIFIS IFU, is a 22-element image slicer mirror array that converts an input 2-D integral field into a 1-D pseudo long-slit. It was developed at the University of Florida and has been tested with the FLAMINGOS spectrograph on the Kitt Peak 4-m telescope (Eikenberry et al., 2004), confirming its functionality. The basic working principle of FISICA is to slice an input 2-D field from the telescope focal plane into 22 ‘slices’ and rearrange them in series to form a pseudo long-slit.

FISICA is mainly composed of three mirror arrays: a slicer array, a pupil array and a field

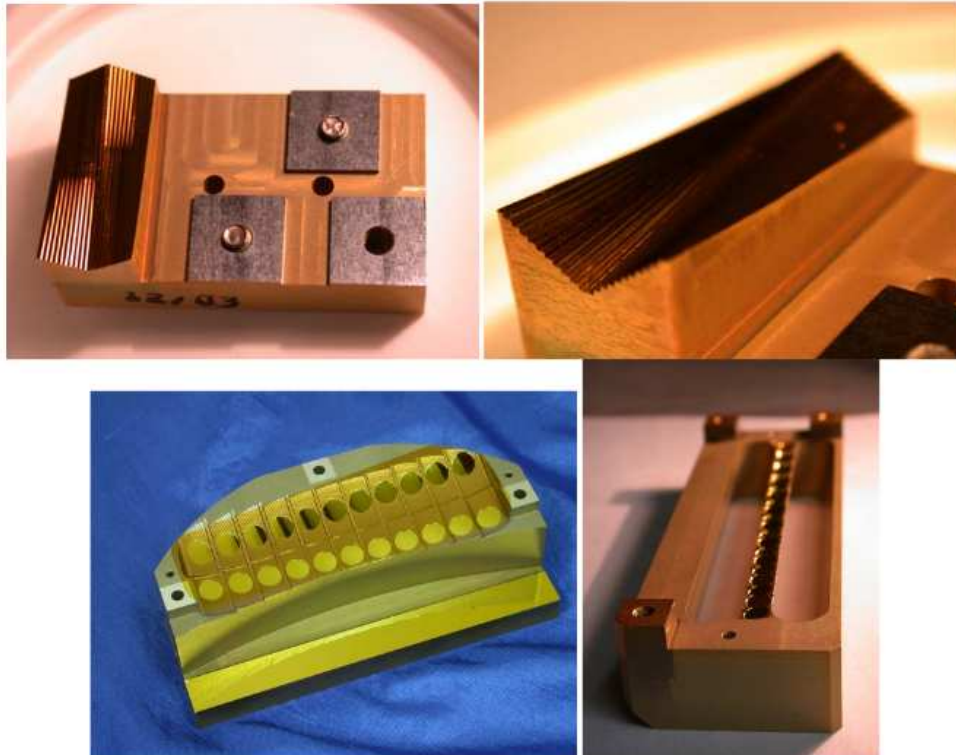


Figure 4.5 Fabricated mirror arrays for FISICA prior to the IFU integration. Images are taken from Eikenberry et al. (2004). Top left panel: slicer array and base. Top right panel: close view of the slicer array. Bottom left panel: the pupil array is composed of 2×11 circular mirrors. Bottom right panel: the 22-element field array.

array, together with its own re-imager relay, which increases an input f-ratio by factor of two (e.g., $f/16$ to $f/32$), and two flat fold mirrors. Figure 4.4 presents the optical layout of FISICA, where an $f/16$ beam from the WIFIS re-imaging unit (see above) is focused on the slicer array of FISICA after its three-mirror re-imaging relay. The slicer array has 22 tilted rectangular slices with cone-shaped cross sections. Figure 4.5 (top panels) shows images of the fabricated slicer array. The 22 slicer mirrors, which form two groups (each group with 11 slicer mirrors) of tilted angles, on the slicer array deliver sliced images to the following pupil array. The pupil array is also composed of 22 circular-shaped pupil mirrors arranged in 2 by 11 format, providing one to one correspondence between the slicer and pupil mirrors (see Figure 4.5 bottom left panel). This geometrical arrangement of the slicer and the pupil arrays minimizes the field angles in FISICA, reducing potential aberrations. After the pupil array lies a field array composed of 22 linearly-arranged mirrors (see Figure 4.5 bottom right panel), which, together with the slicer and pupil arrays, demagnifies the input beam by factor of four (e.g., $f/32$ to $f/8$), resulting in the total net magnification of 0.5 by FISICA (e.g., $f/16$ to $f/8$). The two flat fold mirrors following the field array direct the image of the pseudo long-slit from FISICA to the following collimator system. On a 10-m telescope, FISICA can provide an integral field of $12'' \times 6''$ (or $9 \text{ mm} \times 4 \text{ mm}$), which corresponds to an output pseudo long-slit dimension of $264'' \times 0''.27$ (or $100 \text{ mm} \times 0.098 \text{ mm}$). This is equivalent to $52'' \times 24''$ on a 2.3-m telescope.

The WIFIS integral field size described above is roughly comparable to the maximum integral field size achievable for a seeing-limited IFS using a $2\text{K} \times 2\text{K}$ detector array (e.g., H2RG). The typical seeing in the NIR wavebands for ground-based observatories is $\leq 1''$, and often it can reach below $0''.5$, especially for K band, at the best sites hosting some of the largest telescopes. This requires the width of the pseudo long-slit of an IFU on large (e.g., $> 8\text{-m}$) telescopes to be $\leq 0''.5$, while it can be $\sim 1''$ for smaller telescopes in order to have a highest throughput. This required slit width is similar to what FISICA (i.e., WIFIS IFU) provides: $0''.27$ on a 10-m telescope, or equivalently $\simeq 1''.0$ on a 2.3-m telescope. Given that WIFIS operates at the near Nyquist sampling mode in both the spectral and spatial samplings and also that it uses most of the detector pixels of the H2RG detector, the WIFIS integral field size is comparable with the maximum integral field size that can be obtained with any of a $2\text{K} \times 2\text{K}$ detector array.

4.2.2 Collimator, Dispersing Unit and Spectrograph Camera

Collimator System

The collimator systems of WIFIS1 and WIFIS2 share the same configuration composed of a flat fold mirror, a collimator mirror and a pair of achromatic correction lenses. In Figure 4.3, a fold mirror (FM3) is located behind FISICA changing the direction of the FISICA output beam to avoid any potential vignetting. The two achromatic lenses after the collimator mirror reduce the off-axis ray aberrations of the collimated beam. Both the collimator systems of WIFIS1 and 2 produce $f/8$ output beams.

In the WIFIS1 optical layout (see Figure 4.3 top panel), an OAP mirror serves as the collimator mirror, which is tilted by seven degrees to keep the FISICA output beam from overlapping with the collimated beam. The materials of the two correction lenses are CaF₂ and S-FTM16 (Brown et al., 2004) which provide reduced chromatic aberrations due to similar variation of their index of refractions along the wavelength. The first correction lens has an even aspherical surface of six-order polynomials to minimize spherical aberrations in the collimated beam, whereas the second lens has a normal spherical surface. The diameter of the collimated beam of WIFIS1 is ~ 90 mm, which gives the collimator focal length of 720 mm. In WIFIS2, in contrast, a simple spherical mirror is used as a collimator mirror, along with two correction lenses made of S-FPL53 and S-FTM16 glass materials. Like the collimator system in WIFIS1, the first correction lens in WIFIS2 also has an even aspherical surface of six-order polynomials and the second lens is spherical. WIFIS2 has a collimated beam diameter of ~ 50 mm, which is significantly smaller than that of WIFIS1 and gives the collimator focal length of 400 mm. §4.6 provides detailed comparison between WIFIS1 and WIFIS2.

Dispersing Unit: Diffraction Gratings

Table 4.2 Summary of important parameters of three diffraction gratings used in WIFIS.

	$(z)J$	H	K
Groove Density (lines/mm)	500	400	300
Incident Angle (degrees)	34.7	35.5	35.5
Blaze Angle (degrees)	20.00	18.67	17.46
Blaze Wavelength (μm)	1.37	1.63	2.04
Application	WIFIS1, 2	WIFIS1, 2	WIFIS1

As described in Introduction, WIFIS1 and 2 are designed to satisfy $R \simeq 5,500$ for each of

JHK band (WIFIS1) and for $R \simeq 2,800$ for the *zJ* and *H* bands (WIFIS2). These conditions, together with the collimated beam sizes of 90 mm (WIFIS1) and 50 mm (WIFIS2), require 500, 400, and 300 lines/mm groove densities for the (*z*)*J*, *H*, and *K* bands, respectively. Note that the spectral resolving power is proportional to the total number of grating grooves illuminated by a collimated beam and also to the wavelength. The resulting anamorphic magnification (i.e., magnification ratio between the spectral and spatial directions) is approximately 1.2 for this set of gratings which are blazed at an angle between 17.46 and 20.00 degrees with a blazed wavelength of 1.37 (*J*), 1.63 (*H*), and 2.04 μm (*K*). Table 4.2 summarizes the key parameters of the WIFIS gratings. I use $m = 1$ dispersion mode which gives the maximum grating efficiencies. The gratings for (*z*)*J* and *H* bands were already fabricated by Richardson Grating Inc. using the material of zerodur and fused silica. Both the gratings are gold coated, and the (*z*)*J* band grating has been thoroughly tested at the University of Toronto laboratory.

Spectrograph Camera

Both the spectrograph cameras of WIFIS1 and 2 are composed of five spherical lenses and one aspherical lens whose surface is defined by six polynomial orders. The aspherical lens is the third lens for both WIFIS1 and 2. For a slit-based spectrograph, the spectrograph camera focal length (F_2) is related to the collimator focal length (F_1), grating anamorphic magnification (r), slit width (w), and the width (w') of a projected slit on the detector in the following manner:

$$F_2 = \frac{w' F_1 r}{w} \quad (4.4)$$

This gives the following focal ratio (f_1) of the spectrograph camera

$$f_2 = \frac{w' f_1 r}{w} \frac{d_1}{d_2} = \frac{w' f_1}{w} \quad (4.5)$$

using the relations of $F_1 = f_1 d_1$, $F_2 = f_2 d_2$ and $r = d_2/d_1$, where f_1 and f_2 are the focal ratios of the collimator and spectrograph camera, respectively; d_1 and d_2 are the diameter of the collimated and diffracted beams, respectively. For WIFIS1 and 2, the geometrical slit width provided by FISICA is 98 μm which is imaged on two detector pixels, or 36 μm for the H2RG with 18 μm pitch. Given the f/8 focal ratio of the collimator, this requires \simeq f/3 focal ratio for the spectrograph cameras of WIFIS1 and 2. Due to different collimated beam sizes used in WIFIS1 and 2, the corresponding focal lengths of the spectrograph camera are 320 mm and 180 mm, respectively.

In WIFIS1, all the six camera lenses are made of an achromatic pair of CaF2 and S-FTM16 to minimize chromatic aberrations. This gives three pairs of CaF2 and S-FTM16 for the six lenses, starting from CaF2 which is followed by S-FTM16. The first lens just next to the

grating is made of CaF₂. In WIFIS2, CaF₂ is replaced by S-FPL51, a glass material with similar properties to CaF₂ and also to S-FPL53 used in the collimator. The materials for the six lenses in the WIFIS2 spectrograph: S-FPL51, S-FTM16, S-FPL51, fused silica, S-FPL51 and fused silica (in the direction from the grating to the detector).

4.3 Nominal Performance of WIFIS1 and WIFIS2

4.3.1 Field of View

The WIFIS (both 1 and 2) integral field size is primarily determined by the size of the pseudo long-slit image (=100 mm × 0.098 mm) created by FISICA and also by the optical components following FISICA. As described in §4.2.2, WIFIS1 and 2 have the collimator focal lengths of 720 mm and 400 mm, respectively, while their spectrograph camera focal lengths are 320 mm (WIFIS1) and 180 mm (WIFIS2), resulting in a similar magnification of 0.45. This gives a projected slit length of 45 mm on the detector, which is greater than the H2RG array size of 36.86 mm. Thus, only ~ 80% of the total length of the pseudo long-slit can be covered by the detector, and the final integral FOV on a 10-m telescope is 12'' × 5'' which is a bit smaller than 12'' × 6'' that the FISICA optics can provide. This reduced field corresponds to 18 (out of 22) slices of FISICA. The pixel scale is 0''.1 on a 10-m telescope (or equivalently 0''.46 on a 2.3-m telescope).

4.3.2 Spectral Resolving Power

For a slit-based spectrograph using a diffraction grating as a dispersing unit, its spectral resolving power can be obtained in the following manner. First, the derivative of the grating equation gives the grating angular dispersion of

$$\frac{d\beta}{d\lambda} = \frac{m N_g}{\cos\beta} \quad (4.6)$$

where m and N_g represent the grating diffraction order and the groove density, respectively. Then the grating linear dispersion is

$$\frac{dl}{d\lambda} = \frac{d\beta}{d\lambda} d_2 f_2 \quad (4.7)$$

where β , d_2 and f_2 are the grating diffraction angle, diffracted beam diameter and the focal ratio of the spectrograph camera, respectively. Replacing dl and $d\lambda$ by the projected slit width (ω') and the spectral resolution element ($\delta\lambda$), one can obtain

$$\delta\lambda = \frac{\omega' \cos\beta}{m N_g d_2 f_2} \quad (4.8)$$

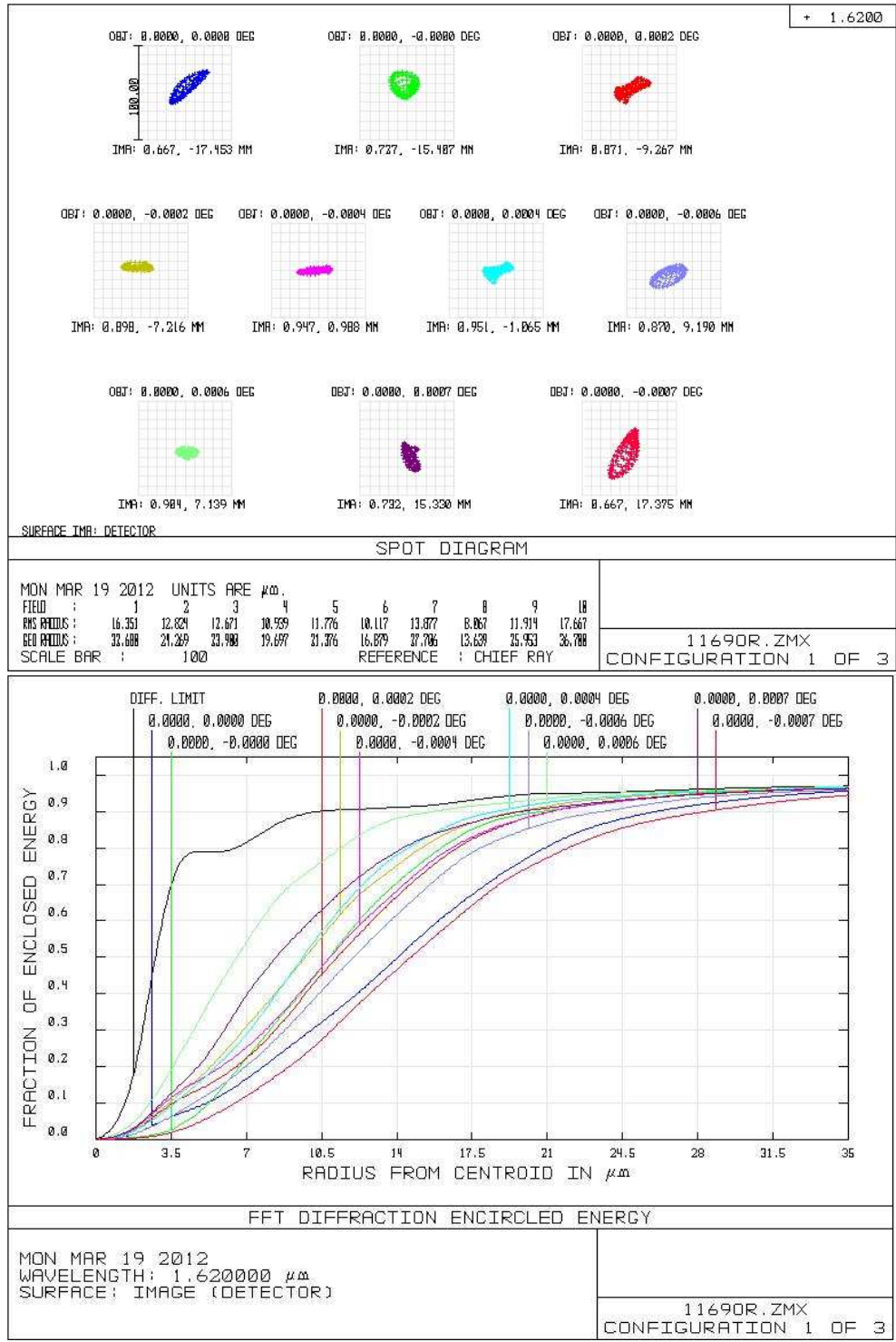


Figure 4.6 Top panel: a typical spot diagram at $\lambda = 1.62 \mu\text{m}$ of WIFIS1, different colors indicate rays from different fields. The average RMS spot radius is $\sim 12 \mu\text{m}$. Bottom panel: a typical encircled energy diagram at the same wavelength. The color definition is the same as the spot diagram. The encircled energy radii is $\sim 11 \mu\text{m}$ (at 50%) and $\sim 15 \mu\text{m}$ (at 80%).

Table 4.3 Summary of important system parameters and the theoretically calculated spectral resolving powers

Parameter	WIFIS1	WIFIS2
Projected slit width (ω')	36 (μm)	36 (μm)
Diffraction angle (β)	3.4° at $\lambda = 1.6 \mu\text{m}$	-2.1° at $\lambda = 1.1 \mu\text{m}$
Diffraction order (m)	1	1
Groove density (N_g)	400 (lines/mm)	500 (lines/mm)
Diffraction beam diameter (d_2)	108 (mm)	60 (mm)
Focal ratio of the camera (f_2)	~ 3	~ 3
Spectral resolving power (R)	$\sim 5,600$ at $\lambda = 1.6 \mu\text{m}$	$\sim 2,700$ at $\lambda = 1.1 \mu\text{m}$

which gives the spectral resolving power

$$R = \frac{\lambda}{\delta\lambda} = \frac{\lambda m N_g d_2 f_2}{\omega' \cos\beta}. \quad (4.9)$$

Table 4.3 lists relevant parameters needed in calculating the spectral resolving powers of WIFIS.

In practice, the real spectral resolving powers of WIFIS may differ from those calculated above due to other practical factors encountered in instrumentation, such as (a) optical aberrations; (b) seeing broadening effects; (c) fabrication and alignment errors; and (d) the instrument working environment. The first two factors, which are related to the optical design, are discussed here, whereas the later two, which are related to the fabrication and alignment of the optical components, are discussed in §4.4.

One common way of investigating into the effects of optical aberrations to the performance of a designed optical system is to analyze spot and encircled energy diagrams. Figure 4.6 shows a typical spot diagram and an encircled energy diagram of WIFIS1 at the center of H band ($\lambda = 1.6 \mu\text{m}$). The size of the spot diagram is $12 \mu\text{m}$, and the size of the encircled energy radii are $11 \mu\text{m}$ (at 50 %) and $15 \mu\text{m}$ (at 80 %), all of which are much smaller than the two detector pixel size of $36 \mu\text{m}$. In conclusion, the averaged root-mean-square (RMS) size of the spot diagram and the 80% encircled energy radius of both the WIFIS1 and 2 designs are smaller than the width (= two detector pixels) of the projected slit. This indicates that the optical aberration effect is negligible.

In addition to optical aberrations, the seeing broadening effect also needs to be taken into consideration because WIFIS operates under natural seeing conditions. To fully understand this, I conducted extensive simulations in Zemax by creating 2-D gaussian PSFs of $1''$ FWHM and subsequently analyzing the performances of the WIFIS optical designs when they were

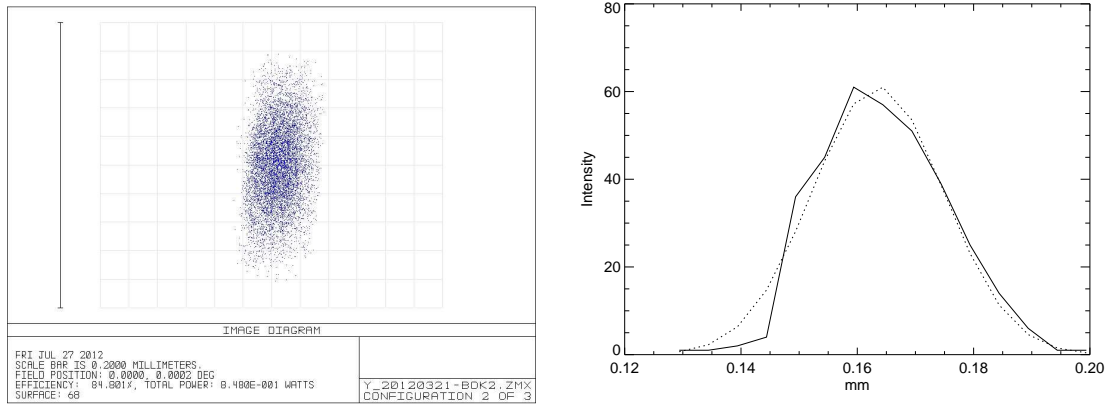


Figure 4.7 Left panel: an example of the seeing broadened projected pseudo slit image on the detector. A Gaussian function with a FWHM of $1''$ on the telescope focal plane was simulated and fed into WIFIS to show how the seeing PSF affects the width of the projected pseudo slit. The physical size of one grid on the panel represents $20 \mu\text{m}$. Right panel: intensity profile of the projected slit image shown in the left panel. The vertical axis has an arbitrary scale, which is determined by the number of rays used for the simulation. The dashed line represents the best-fit Gaussian function with a FWHM of 1.5 pixels ($\sim 30\mu\text{m}$).

fed with the created PSFs. One example of the simulations is given in Figure 4.7, where the projected slit width on the detector is fitted to be smaller than two detector pixels. The analyses of the seeing PSF simulations showed that the WIFIS spectral resolving powers were very similar to what were theoretically calculated, indicating that the degradation in the WIFIS performance caused by the seeing effect is insignificant. If we compare the effects of the optical aberrations and those of the seeing to the WIFIS performance, the latter is much more significant than the former, although both are within an acceptable level.

The effects of the geometrical optical aberrations to the WIFIS performance are small as shown above. However, this is not true for the case of the chromatic aberration resulting mainly from the wavelength dependence of the refractive index of the WIFIS lenses. In fact, the spectral resolving powers in K band of WIFIS1 and H band of WIFIS2 are $\sim 10\%$ and $\sim 30\%$ lower than the best spectral resolving powers obtainable at the wavelengths with the minimum chromatic aberrations. In conclusion, while WIFIS provides spectral resolving powers comparable to theoretically calculated ones in most of its operational wavebands, the resolving powers are degraded slightly for certain wavelength range due to increased chromatic aberrations.

4.3.3 Spectral Coverage

Spectral coverage is the wavelength range that can be obtained in a single exposure. This can be obtained by multiplying the spectral width of the spectral resolution element (see equation 4.8) by the number of the spectral resolution elements. Assuming the Nyquist sampling, the latter is $\sim 1,000$ for a row of 2K detector pixels. The expected spectral width of one spectral resolution element of WIFIS1 based on the equation 4.8 and Table 4.3 is $2.8 \times 10^{-4} \mu\text{m}$ in H band, resulting in $0.29 \mu\text{m}$ spectral coverage. Similarly, the WIFIS1 spectral coverage in J and K band is $0.23 \mu\text{m}$ and $0.38 \mu\text{m}$, respectively. For WIFIS2, the spectral coverage of zJ band and H band is $0.41 \mu\text{m}$ and $0.51 \mu\text{m}$, respectively. Table 4.4 summarizes the WIFIS spectral coverage in different wavebands.

Table 4.4 Expected spectral coverage for WIFIS1 and WIFIS2.

WIFIS1		WIFIS2	
Spectral Coverage (μm)		Spectral Coverage (μm)	
J	0.23 (1.14 – 1.37)	zJ	0.41 (0.89 – 1.30)
H	0.29 (1.47 – 1.76)	H	0.51 (1.30 – 1.81)
K	0.38 (1.98 – 2.36)	K	None

I also confirmed the theoretically calculated spectral coverages above using Zemax simulations. Figure 4.8 shows the spectral coverage in WIFIS1 H and WIFIS2 zJ bands. The WIFIS1 H band spectral coverage is $1.47 - 1.76 \mu\text{m}$; the WIFIS2 zJ band spectral coverage is $0.89 - 1.30 \mu\text{m}$. The spectral coverages in different wavebands obtained from Zemax simulations are also summarized in Table 4.4.

4.4 Expected System Performance of WIFIS1 and WIFIS2

4.4.1 Design Tolerance Analyses

In any type of optical design, one key process is robust and reliable tolerance analyses which can give a direct indication of the performance of the system when all the optical components are fabricated and put in place together. For the WIFIS1 and 2 designs, I performed rigorous tolerance analyses using the Zemax software and confirmed that the expected system performances are compatible with their design goals. I divided the optical components of WIFIS1, 2 into three groups for convenience in the tolerance analyses: (a) re-imaging unit; (b) collimator system; and (c) spectrograph camera. For each of these three groups, I assigned compensators

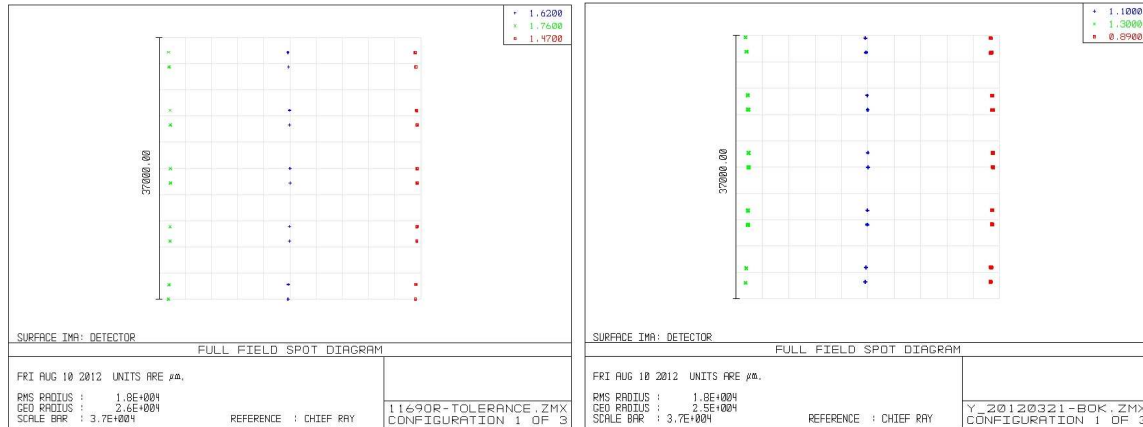


Figure 4.8 Spectral coverage of WIFIS1 H and WIFIS2 zJ band in left and right panel, respectively. Images of projected pseudo long-slit at different wavelengths on the detector surface are shown in different symbols and colors. The scale bar on the left hand side of each panel represents the physical size of the detector.

that can mitigate performance degradation caused by potential fabrication and alignment errors and help maximize the system performance. The compensators are: (a) the space between FM1 and OAP1 and tilt of OAP1 (WIFIS1,2) for the re-imaging unit; (b) the space between FM3 and the collimator mirror (WIFIS1,2) for the collimator system; (c) the space between the final lens and detector (WIFIS1), or the space between the fifth and sixth lenses (WIFIS2) for the spectrograph camera– see Figure 4.3 for the locations of these mirrors and lenses.

Table 4.5 Acceptable tolerances in WIFIS optical designs

Potential Fabrication and Alignment Errors	Tolerance
Surface Radius	0.1% or 0.05%
Air Space	0.1 (mm)
Thickness	0.1 or 0.05 (mm)
Element Decenter	0.05 (mm)
Element Tilt	0.025 (mm)
Element Wedge	0.025 (mm)
Surface Irregularity	0.5 or 1.0 (fringes)
Index of Refraction	0.01%

Table 4.5 summarizes the acceptable tolerances of the optical parameters of WIFIS1, 2.

Table 4.6 Summary of tolerance analyses results for WIFIS1 and WIFIS2

Potential Fabrication and Alignment Errors	Changes in Spot Radius (μm)					
	Re-imaging		Collimator		Spectrograph	
	Unit		System		Camera	
	WIFIS1/WIFIS2		WIFIS1/WIFIS2		WIFIS1/WIFIS2	
Surface Radius	0.92	0.62	3.57	2.08	1.85	1.53
Air Space	0.11	0.57	0.21	0.29	0.50	0.74
Thickness	-	-	0.88	0.46	0.55	1.12
Element Decenter	1.98	0.23	1.81	3.37	2.96	2.59
Element Tilt	1.01	0.60	0.66	3.29	1.22	1.59
Element Wedge	-	-	0.31	2.45	1.55	1.89
Surface Irregularity	0.41	0.48	1.87	2.09	0.60	1.46
Index of Refraction	-	-	1.04	0.28	0.77	0.64
RSS Total	2.50	1.16	4.70	6.10	4.19	4.47
Nominal Spot Radius	12.43 (WIFIS1)		12.50 (WIFIS2)			
RSS Degraded Spot Radius	14.15 (WIFIS1)		14.65 (WIFIS2)			

⁴ For the tolerances determined by manufacturing capabilities of companies (such as surface radius, thickness, surface irregularity, element wedge, and refractive index), we adopt the values provided by potential manufacturers. For the other tolerances related to the alignment of the optical system (such as element decenter and tilt), we use the Zemax software to estimate their acceptable limits.

Table 4.6 shows the corresponding changes in the spot radius for the given acceptable tolerances presented in Table 4.5. The change in spot radius reflects the susceptibility of each group to various fabrication and alignment errors. As shown in Table 4.6, the collimator system is the most sensitive part to small perturbations (and has the tightest tolerance), which has a $\sim 5 \mu\text{m}$ spot radius change for both the WIFIS1, 2 designs, corresponding to $\sim 35\%$ degradation of the spot radius. The spectrograph camera is second to the collimator system and the re-imaging unit is the most forgiving part. Among the potential fabrication and alignment errors, surface radius, element decenter and element tilt have the most substantial effects to the system performance. The changes in spot radius caused by the three main potential fabrication and

⁴The element tilt is in linear unit, which is the arc length defined by the element diameter and the tilt angle. The tilt angle varies from $0.5'$ to $\sim 4'$ depending on the size of the optics. The fringe number shown in the surface irregularities is defined by $\lambda = 633 \text{ nm}$.

alignment errors correspond to $\sim 20 - 30\%$ degradation of the spot radius.

After establishing the acceptable tolerances of the optical parameters (Table 4.5), I performed 100 Monte Carlo simulations of WIFIS1, 2 with all the optical components in place by randomly changing the parameters of the components within the tolerance range. In each simulation, the given optical system was optimized against the compensators. The overall performance of the simulated systems show little change from the ideal case.

The expected performance of the WIFIS designs can be obtained using the systems generated by the 100 Monte Carlo simulations based on the established tolerance ranges since the simulated systems can give a representative variation of the system performance if WIFIS is built within the tolerance ranges. Overall, our analyses show that the average performance of the Monte Carlo simulations is compatible with the nominal performance described in § 4.3. They have the same spectral coverage and FOV, and the major difference lies on the spot radius, which may result in a small degradation of the spectral resolving power. Figure 4.9 compares the spot radius of the nominal performance with that expected from the Monte Carlo simulations as a function of the wavelength for WIFIS1, 2, showing that the spot radius of the Monte Carlo simulation is $\sim 10\%$ larger than that of the nominal performance.

Although the above analyses give us the ‘averaged’ expected performance of WIFIS when it is built, it is occasionally the case that the real performance in practice is somewhat worse than what is expected in average. Hence, in order to conduct a rather conservative investigation into the expected system performance, I adopted the simulated system of which performance is worse than the average Monte Carlo performance by two standard deviations (or 95 % outlier). I call this system ‘as-built system’. Comparisons between the nominal and as-built performances show that a major difference again comes from the spot radius, showing 10 – 20 % degradations compared with the $\sim 10\%$ degradation of the average case (Figure 4.10). Notably, however, even with the 20 % increase in the spot radius, it is still smaller than (or similar to) the size of the two detector pixels for most of the integral field and the spectral range. This tells that it is in the end the seeing broadening, rather than the fabrication and alignment errors, that really determines the practical performance of WIFIS (see §4.3.2 for the seeing broadening effect).

Table 4.7 compares the spectral resolving powers, which are averaged over the entire integral field and also over the given waveband, of the nominal and as-built performances. As shown in Table 4.7, they have very similar performances, except for those of the as-built system in the K band of WIFIS 1 and H band of WIFIS2 caused by the chromatic aberrations of the refractive components (see § 4.3.2).

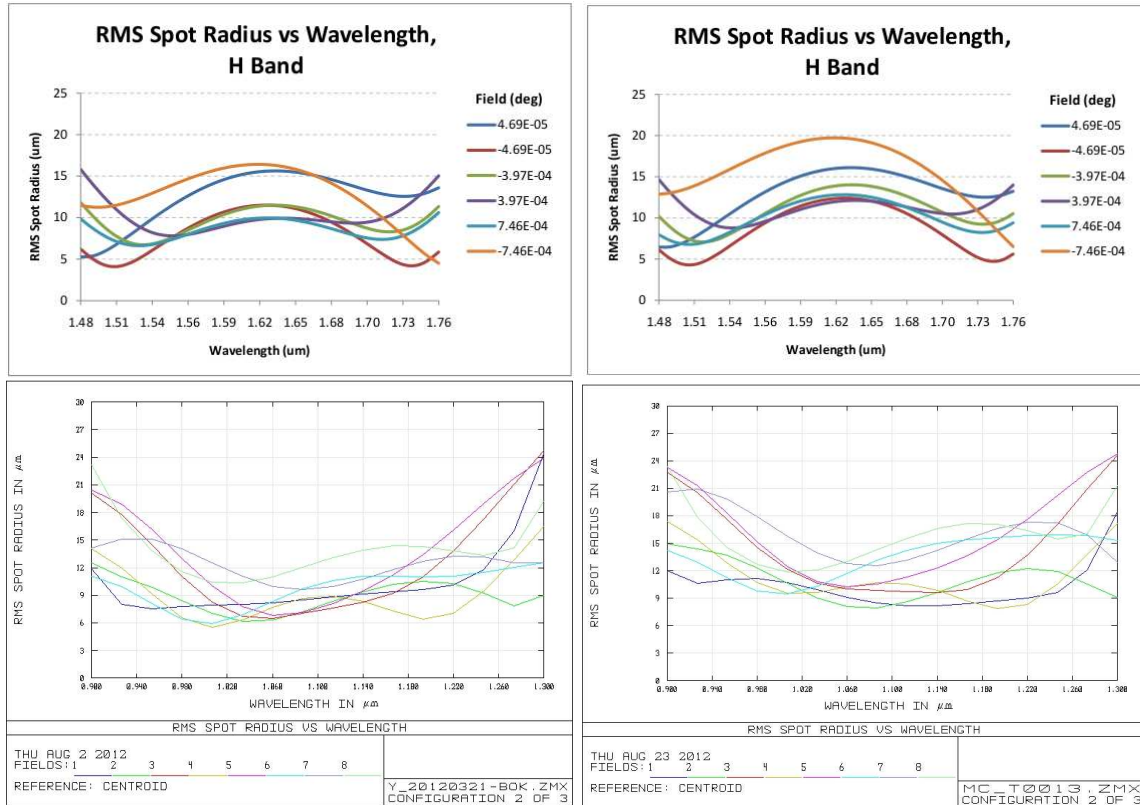


Figure 4.9 Nominal and average Monte Carlo performance in spot radius as a function of wavelength shown in left and right panels, respectively. The results for WIFIS1 and WIFIS2 are shown in the top and the bottom panels, respectively.

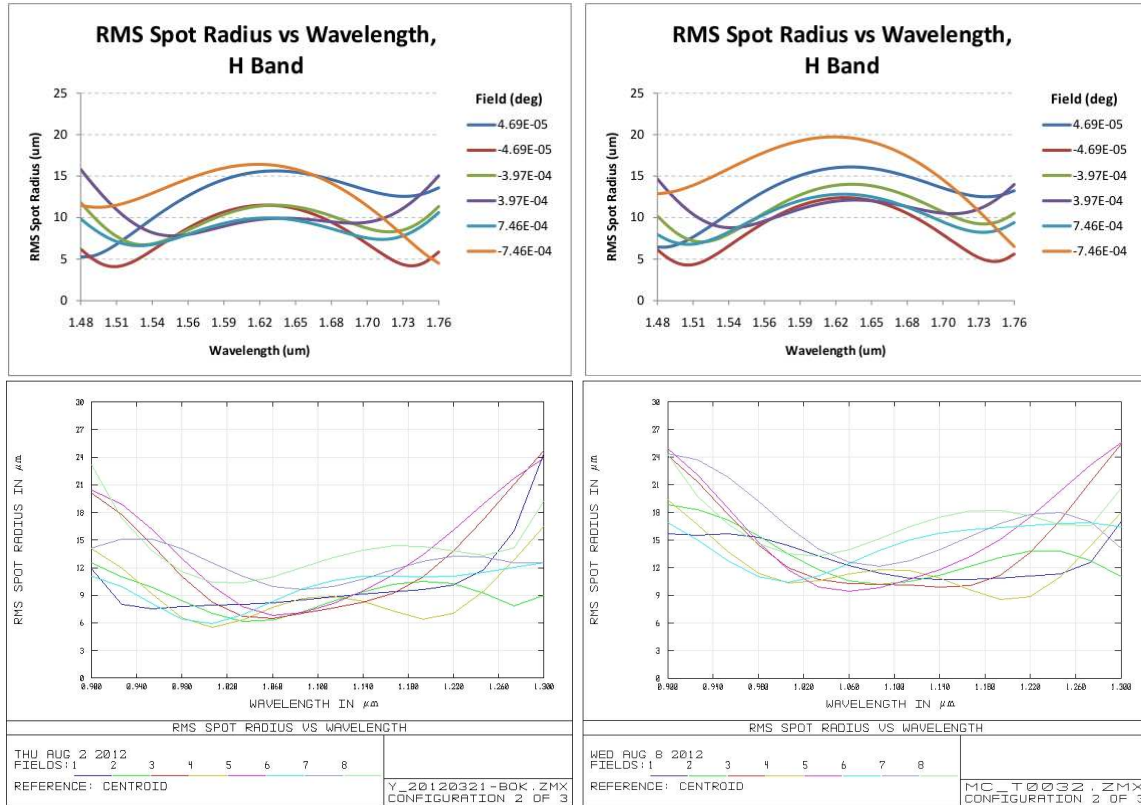


Figure 4.10 Nominal and as-built performance in spot radius as a function of wavelength shown in left and right panels, respectively. The results for WIFIS1 and WIFIS2 are shown in the top and the bottom panels, respectively.

Table 4.7 Expected spectral resolving power for WIFIS1 and WIFIS2.

WIFIS1			WIFIS2		
Spectral Resolving Power (Nominal, Expected)			Spectral Resolving Power (Nominal, Expected)		
<i>J</i>	5,400	5,200	<i>zJ</i>	2,700	2,700
<i>H</i>	5,600	5,500	<i>H</i>	3,000	2,000
<i>K</i>	5,700	5,000	<i>K</i>	None	None

4.4.2 Thermal Environmental Effects in WIFIS Designs

WIFIS1 covers the entire NIR *JHK* wavebands, whereas WIFIS2 is focused on the shorter bands of *zJ* (and *H*). This requires a fully cryogenic instrument for WIFIS1 due to thermal background radiation at longer wavelengths, especially in *K* band. While a fully cryogenic instrument always requires extensive instrumentation efforts, it nevertheless gives very stable performance because all the components of the instrument are operated at the same temperature. For WIFIS2, which is optimized for *zJ* band observations, on the other hand, the cryogenic requirement is less critical as long as the instrument is capable of removing the effects of the longer wavelength radiation in an efficient way. (Note that the WIFIS H2RG detector is sensitive up to $\lambda = 2.5 \mu\text{m}$.) One relatively easy way to effectively remove the thermal background radiation at longer wavelengths is to employ a thermal bandpass blocking filter which only accepts photons whose wavelength is shorter than the cut-off wavelength of the filter. Another aspect that needs to be considered for WIFIS2 in terms of the thermal environmental effect is the variation of the instrument performance as a function of the environmental temperature, given that it changes continuously over the observations. Below, we investigate into this effect and provide a feasible solution.

As mentioned above, the system performance of WIFIS2 is sensitive to the changes in thermal environment conditions because the parameters of each optical components (e.g., surface radius, thickness, etc.) are functions of environment temperature and pressure. Here only the change in temperature is considered because the change in pressure is relatively small. To better understand this temperature variation effect, an investigation was conducted by changing the WIFIS2 working temperature. The air space and the surface radius of all the components, along with their thickness and the index of refraction of refractive components, outside the detector dewar were set to vary as the temperature changes. The resulting changes in the system performance were examined by analyzing the spot diagrams at different temperatures, and one example is shown in Figure 4.11. Compared with the spot diagrams of $T = 20^\circ$ Celsius at

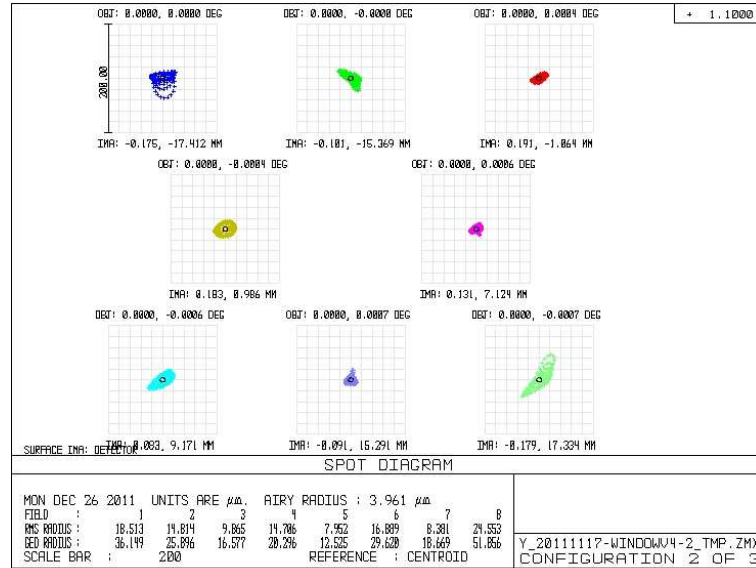


Figure 4.11 Spot diagram at $\lambda = 1.1 \mu\text{m}$ with the environment temperature $T = 30^\circ$ Celsius. Compared with the RMS spot radius at the optimized temperature $T = 20^\circ$ Celsius, the spot radius at $T = 30^\circ$ Celsius increases by roughly a factor of two.

which the WIFIS optical designs are optimized, the spot radius changes roughly by a factor of two for the given temperature variation $\Delta T = \pm 10^\circ$ Celsius. Both the variations in air space between the optical components and those in their surface radius are the dominant sources of the changes in the system performance.

The changes in the optical parameters are either monotonic increase or decrease as the temperature increases or decreases, which gives a monotonic shift of the spectrograph camera focal plane. A straightforward way to compensate the temperature variation is to change the detector position accordingly. However, a difficulty of applying this method lies on the implementation of a moving mechanism inside the detector dewar. An alternative way, which has a similar effect to moving the detector directly, is to move the detector dewar directly to compensate the temperature variation. According to the Zemax simulations that I conducted, given the temperature change of $\pm 10^\circ$, the dewar needs to be shifted by ± 0.1 mm to compensate the temperature variation. If the environment temperature is decreased to 0° (i.e., $\Delta T = 20^\circ$ Celsius), a shift of 0.15 mm in the dewar position is required for compensation. This can be managed in a practical way by employing an actuator of $50 \mu\text{m}$ accuracy to the detector dewar that can handle 200 pounds loading. Such an actuator is readily available.⁵

Another issue of implementing WIFIS2 as a non-cryogenic instrument is to reduce the

⁵For example: Osmtec (<http://www.osmtec.com/>).

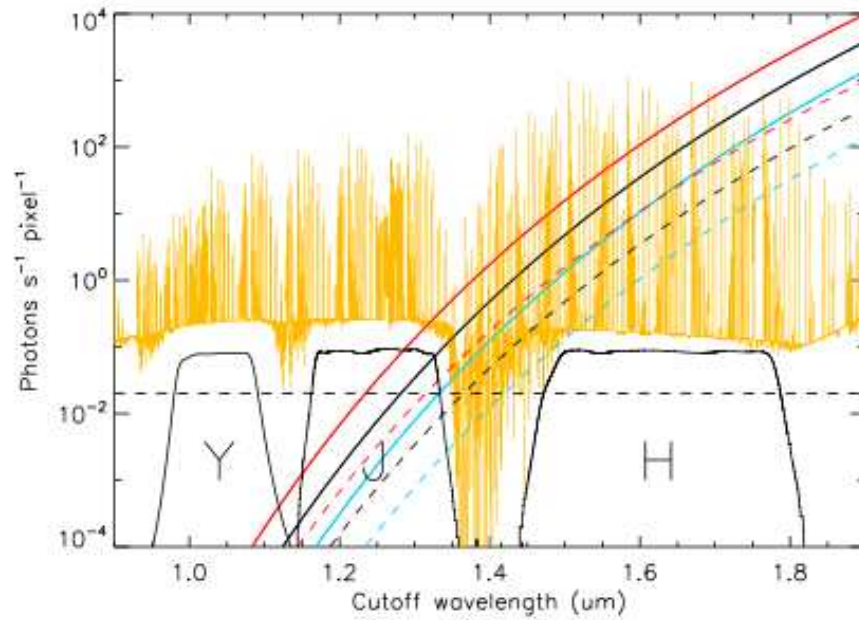


Figure 4.12 Expected photon flux per pixel from thermal radiation as a function of the cut-off wavelength of the thermal blocking filter used within instrument, taken from Sivanandam et al. 2012. The solid and dashed curves are thermal emission for a blackbody and a grey body with an emissivity of 0.1, respectively. The blue, black, and red curves represent thermal emission from 0° , 10° , 20° Celsius bodies, respectively. The orange curve is the model of the dispersed sky emission convolved to the spectral resolution of WIFIS. The common NIR filter bandpasses are shown for reference. The dashed horizontal line is the approximate dark current for an H2RG in photon units. Thermal light begins to dominate longward of J band and is the main source of background in H band.

thermal background radiation seen by the H2RG detector effectively at longer wavelengths. Unlike the sky background, the thermal background radiation may not be dispersed by the grating because the majority of it will come from the uncooled components of the instrument (e.g., spectrograph camera and WIFIS enclosure). The cut-off wavelength of the H2RG detector is $2.5 \mu\text{m}$, which implies there is significant amount of thermal background radiation produced by the uncooled components of the instrument that will be seen by the detector. As mentioned above, to combat this issue a custom made thermal bandpass blocking filter will be used to block out light redder than our operating wavelength range. A simulation was conducted to show the degree to which thermal light affects our observations. The results of this simulation are shown in Figure 4.12. The sky emission (orange curve) is taken from the Gemini Near-IR Sky Background and has been appropriately convolved to match our spectrograph resolution and multiplied by the end-to-end throughput of the telescope and the instrument. The solid and dashed curves show the photon flux that detector sees if there was a cut-off filter upstream that removed all light longward of the specified wavelength. A range of instrument emissivities and temperatures was tested: the dashed curves represent an optimistic emissivity of 0.1 whereas the solid curves are for the worst case where the instrument emissivity is 1. A range of temperatures normally expected at the observatories were also simulated and the results are shown in Figure 4.12 as color curves. It is clear from the simulations that even in the best case, the thermal flux becomes the dominant noise component longward of J band. Therefore, the spectrograph can achieve sky-limited performance only for wavelengths shorter than $1.3 \mu\text{m}$, provided there is a filter that blocks all light with wavelengths longer than $1.3 \mu\text{m}$. In H band, performance will be significantly degraded because the thermal light within the H band bandpass cannot be blocked. However, our goal has been to optimize the spectrograph performance in the $0.9 - 1.3 \mu\text{m}$ range and this issue is not of serious concern.

4.5 Predicted On-sky Characteristics

After exploring the thermal environmental effect of WIFIS designs, the predicted on-sky performance was estimated in the $0.9 - 1.3 \mu\text{m}$ range where the instrument sensitivity is not degraded by its own thermal light. Simulations were conducted for two different instrument destinations: (1) 2.3-m Steward Bok telescope at Kitt Peak, USA, and (2) 10-m GTC in the Canary Islands, Spain. These two possible destinations span the range of telescope aperture sizes that WIFIS can be used with and provide the upper and lower limits of WIFIS sensitivity.

End-to-end simulations were conducted that used realistic models of atmospheric transmission and background, throughput of the telescope and the instrument, and detector characteris-

tics were used to predict the final sensitivity of the instrument. For modelling the atmospheric transmission and background, we obtained the necessary files from the Gemini Near-IR Sky Background⁶ and Transmission⁷ websites. We chose the files representative of Manua Kea during fair conditions: water column = 3.0 mm and air mass = 1.5. The sky brightness was rescaled to match a more realistic estimate of the sky brightness in between the OH lines in the *J* band of 17.7 AB mag arcsec⁻².⁸ To estimate the instrument throughput, we took into account the reflectivity of the mirrors, the transmission of the lenses and dewar window, the blocking filter transmission, the average efficiency of the grating as a function of wavelength, and the detector quantum efficiency (QE). All mirrors including those within the IFU are gold coated. We assume a reflectivity of 0.98 for these mirrors. The lenses and the window are AR-coated to reflect less than 1.5% of their light and their internal transmission is close to 100% across the wavelengths of interest. We assume a lens/window transmission of 0.985. For the thermal blocking filter, we assume a throughput of 0.8. The grating efficiency was taken to be the values provided by Newport for the corresponding master grating. The QE of the detector used for simulations was given in its test report and we present the QE values in Table 4.8. The

Table 4.8 HAWAII 2RG Detector Parameters

Wavelength Range	0.8 – 2.5 μm
Number of Pixels	2048 \times 2048
Dark Current	$< 0.02\text{e}^- \text{s}^{-1} \text{pixel}^{-1}$
Read Noise	5 e^-
Full Well Depth	120,000 e^-
Quantum Efficiency	0.75 @ 0.8 μm 0.76 @ 1.0 μm 0.76 @ 1.2 μm 0.84 @ 2.0 μm

overall throughput of the instrument is shown in Figure 4.13. Because the blaze wavelength of the grating is approximately 1.35 μm , the throughput of the instrument is relatively low in the blue end, reaching 10%. However, on the red end where we are closer to the blaze wavelength of the grating, we reach a much higher throughput of 35%. Note that this does not include the telescope throughput, which needs to be included in the sensitivity calculations. For these calculations, we assumed the primary and secondary telescope mirrors were aluminum coated

⁶<http://www.gemini.edu/?q=node/10787>

⁷<http://www.gemini.edu/?q=node/10789>

⁸<http://irlab.astro.ucla.edu/mosre/MOSFIRE%20PDR%20Report%20v4.pdf>

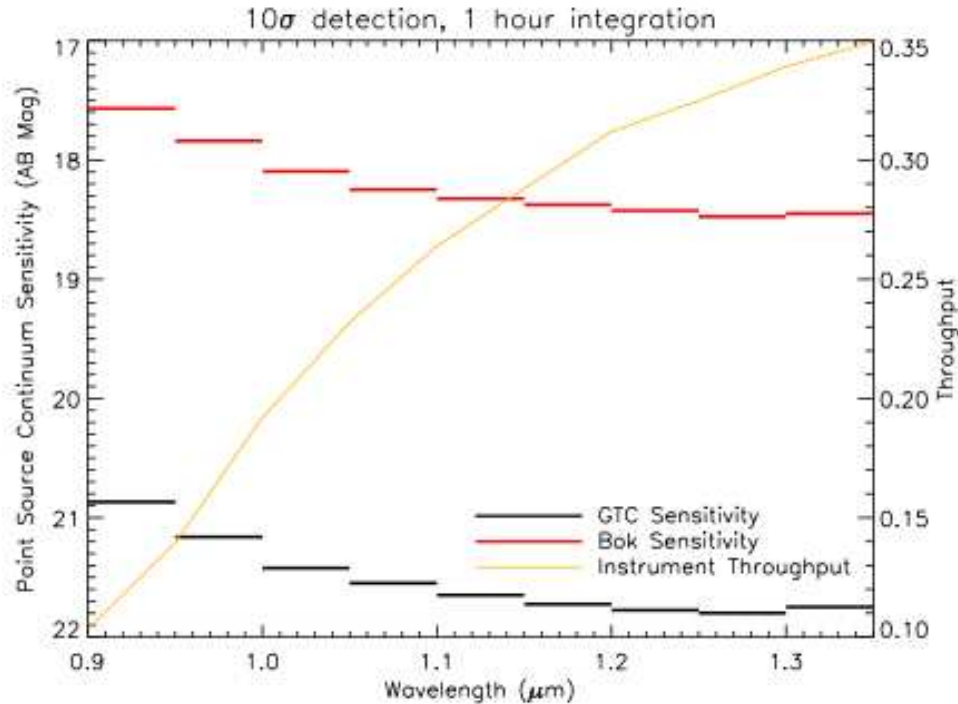


Figure 4.13 Expected point source continuum sensitivity at the GTC (black curve) and the Bok (red curve) telescopes and WIFIS instrument throughput (orange curve) as a function of wavelength, taken from Sivanandam et al. (2012). The plotted continuum sensitivity is for a 10σ detection after an hour of integration time. The darkest regions in between the OH lines and typical seeing conditions are used to compute the sensitivity. The instrument throughput is also plotted, but note that it does not include losses from the telescope.

and each had a reflectivity of 0.92.

The point source continuum sensitivity for the instrument at both the Bok and the GTC telescopes was estimated. The assumed detector noise characteristics are given in Table 4.8. The expected read noise can be achieved through 16 frame Fowler sampling. We assumed a thermal photon flux of $0.5 \text{ s}^{-1} \text{ pixel}^{-1}$, which is the most conservative estimate when using a filter that cuts off all light long ward of $1.35 \mu\text{m}$. The point source width was set to be $0''.5$ at the GTC and $2''$ at Bok, which are the typical seeing values at those sites. The predicted 10σ continuum sensitivity for an hour long integration are shown in Figures 4.13. The hour long integrations are taken as 10 six-minute exposures. We compare our sensitivities with a more complex seeing-limited, NIR, integral-eld spectrograph, KMOS, for the Very Large Telescope that will be commissioned later this year. The predicted 5σ point source continuum sensitivity for the KMOS instrument is 24 AB mag in $1.0 - 1.5 \mu\text{m}$ range for $R \sim 1,000$ (Sharples et al.,

2004). Rescaling to $R \sim 3,000$ and for 10σ detection, the KMOS sensitivity would then be 22 AB mag in $1.0 - 1.5 \mu\text{m}$ range. At $1.0 \mu\text{m}$ our sensitivity is approximately 0.5 mag worse, but at $1.3 \mu\text{m}$ our sensitivity is comparable. On the smaller aperture size end, the sensitivity of the TripleSpec NIR spectrograph at the 3.5-m Apache Point Observatory (APO) is a reasonable comparison. The measured 5σ continuum sensitivity for this spectrograph is 18 AB mag in J band. If we correct for the difference in aperture size between APO and Bok, we expect a 10σ sensitivity of 16.3 AB mag for TripleSpec. This is almost 1 – 2 mag worse than our predicted performance. This can be attributed to at least in part to the reduced throughput (< 0.1) of TripleSpec in J band (Herter et al., 2008). This difference in throughput could account for a 1.3 mag difference in sensitivities, but not 2 magnitudes. It may be possible that our expected performance at the Bok telescope is slightly optimistic, as the atmospheric transmission and background is likely worse at Kitt Peak.

4.6 Comparisons between WIFIS1 and WIFIS2

As described above, WIFIS1 and 2 are based on the same optical configuration consisting of re-imaging unit, IFU FISICA, collimator system, gratings and spectrograph camera. The individual components, however, have different optical properties in terms of the combination of materials and geometrical shapes (e.g., curvature, surface, size), resulting in the differences in the spectral resolving powers and coverage between the two designs. Here, I summarize the differences between the WIFIS1 and WIFIS2.

The most fundamental difference is the *physical size of the collimated beam*, which results in the difference in the spectral resolving power and the spectral coverage. As shown in Equation 4.9, the spectral resolving power is proportional to the diffracted beam size of the grating d_2 , which is proportional to the collimated beam size. The collimated beam diameter in WIFIS1 is ~ 90 mm, while that in WIFIS2 is reduced by 40% to ~ 50 mm. Therefore, the spectral resolving power is reduced from $R = 5,200$ (WIFIS1) to $R = 3,000$ (WIFIS2) by $\sim 40\%$ in the $(z)J$ band, and consequently the spectral coverage is increased from $0.23 \mu\text{m}$ (WIFIS1) to $0.4 \mu\text{m}$ (WIFIS2) by $\sim 40\%$. Since the size of the collimated beam in WIFIS2 is reduced, the overall size of the WIFIS2 system is also reduced. The WIFIS1 design has a dimension of $1.4 \text{ m} \times 0.8 \text{ m}$; WIFIS2 is $0.8 \text{ m} \times 0.8 \text{ m}$. The difference in the collimated beam size also results in the difference in the grating size between WIFIS1 and 2. The grating substrate size is $135 \text{ mm} \times 165 \text{ mm}$ for WIFIS1, while it is $110 \text{ mm} \times 110 \text{ mm}$ for WIFIS2.

The combination of lens material of WIFIS1 is very different from that of WIFIS2. While WIFIS1 is mainly based on CaF₂ and S-FTM16 pairs, WIFIS2 uses a combination of S-FPL51,

S-FPL53, S-FTM16 and fused silica. For WIFIS1, CaF2 and SFTM16, which is known to be an achromatic pair, give very small chromatic aberrations over a wide wavelength coverage due to their variations of the refractive indices (Martini et al., 2004; Eikenberry et al., 2006). As a result, WIFIS1 provides relatively uniform performances in the entire *JHK* NIR bands. However, this choice of the lens material has one important drawback – CaF2 is very difficult to manufacture and is also very expensive. For WIFIS2, in contrast, I chose the glass material S-FPL51 and S-FPL53 to form achromatic pairs with S-FTM16 and fused silica. The former are glass materials with very similar properties to CaF2, but are easier to manufacture and are also much cheaper. Both WIFIS1 and WIFIS2 use two lenses in the collimator system and six lenses in the spectrograph camera, with two even aspherical lenses, one in the collimator system and the other in the spectrograph camera. The lens sizes are different between WIFIS1 and 2; for example, the largest lens in WIFIS1 has a diameter of ~ 180 mm; it is ~ 170 mm in WIFIS2. The collimator mirror of WIFIS1 is an aspherical OAP; whereas in WIFIS2 the collimator is a simple spherical mirror.

There are two additional differences to be noted between WIFIS1 and 2. First, WIFIS1 has a larger distance between FM3 and the collimator mirror than WIFIS2 due to its larger beam size, and the tilt angle of the collimator mirror is increased from seven degrees (in WIFIS1) to eight degrees (in WIFIS2) to avoid any potential vignetting. Second, the dewar entrance window is the first optical component in WIFIS1 located at the telescope focal plane; it is located between the fifth and sixth lenses in WIFIS2. For WIFIS2, there is a thermal blocking filter located inside the dewar.

Both WIFIS1 and 2 are optimized for studying kinematics and chemistry of extended objects by maximizing the advantages of their integral field size combined with the good spectral resolving powers and coverages. One of the primary science targets of them is redshifted H_α line emission from merging galaxies or star-forming galaxies at the redshift ranges of $z \sim 1.5$ (for WIFIS1) and $0.4 < z < 1.0$ (for WIFIS2). WIFIS1 provides a spectral resolving power $R \sim 5,500$ (or an instrumental velocity resolution of 55 km s^{-1}) with a spectral coverage in each of *JHK* band in a single exposure. Therefore, it is ideal for detailed 2-D spectroscopic studies mainly focusing on redshifted H_α line emission from high- z (i.e., $z \sim 1.5$) galaxies or galaxy mergers. On the other hand, WIFIS2 has a slightly lower spectral resolving power ($R \sim 3,000$) but with wider spectral coverage in *zJ* band ($0.4 \mu\text{m}$) in a single exposure. This makes WIFIS2 better suited for conducting 2-D spectroscopic surveys of galaxies or galaxy mergers at smaller redshifts (e.g., $z \sim 0.5$), but with an increased range. In the nearby Universe, WIFIS observations towards resolved stellar populations in nearby galaxies can provide supplementary spectroscopic information in the NIR regime, which is helpful in modelling the

star formation histories (Förster Schreiber et al., 2001, 2003) and probing the stellar initial mass functions in other galaxies (van Dokkum & Conroy, 2012). WIFIS observations of galactic central kilo- or sub kilo-parsec regions can provide information of hot turbulent gas and broaden our understanding of gas fueling mechanisms for the central super massive black holes (Böker et al., 2008). This kinematic information is crucial to studies of active galactic nuclei and circumnuclear kilo-parsec size star formation rings. In addition to the extragalactic applications, WIFIS can benefit other astronomical questions in Galactic astronomy. Since these Galactic objects sustain relatively large angular sizes in the sky and tend to be bright, it will be ideal to take the advantage of small telescopes (i.e., 2–4 m class telescopes) to conduct 2-D spectroscopic observations using WIFIS. With a spectral coverage in the NIR regime, hydrogen lines ($[\text{Pa}_\alpha]$, $[\text{Pa}_\beta]$), He lines and iron lines ($[\text{Fe II}]$) are potential targets which can be used to understand the physical condition of the environment. In addition, studies of shock propagation and stellar outflows within star forming regions require detailed kinematic information, which can be obtained through prominent emission lines such as $[\text{Pa}_\beta]$ or $[\text{Fe II}]$ (Luhman et al., 1998; Moon et al., 2009).

4.7 Summary and Conclusion

WIFIS is an image slicer-based IFS which can provide an unprecedentedly large etendue with comparable spectral resolving powers among currently available NIR IFSs. Two versions of WIFIS optical designs, WIFIS1 and WIFIS2, were developed targeting at different science goals, providing a $12'' \times 5''$ integral FOV on a 10-m telescope, or equivalently $52'' \times 20''$ on a 2.3-m telescope. WIFIS1 provides spectral resolving powers $R \sim 5,500$ in each of JHK band within a single exposure; WIFIS2 does $R \sim 3,000$ in zJ ($0.9\text{--}1.3 \mu\text{m}$) and H ($1.3\text{--}1.8 \mu\text{m}$) bands. The expected system performance of the WIFIS designs are analyzed by considering the effects of the optical aberrations, seeing broadening, fabrication and alignment errors, and thermal environments. Our analyses show that both the WIFIS designs are expected to provide the system performances comparable with the design goals of the instrument in most of the covered wavelength range. The spectral resolving power of WIFIS1 in K band and that of WIFIS2 in H band are $\sim 10\%$ and $\sim 30\%$ lower than the design goals due to chromatic aberrations. The unrivalled combination of the size of the integral FOV, spectral resolving powers, and spectral coverage will be superb in investigating the dynamics and chemistry of extended astronomical objects. Potential scientific applications of WIFIS include 2-D spectroscopic studies of galaxy mergers, star-forming galaxies, local galaxies, Galactic star-forming regions and supernova remnants.

Chapter 5

Laboratorial Characterizations of WIFIS Integral Field Unit

5.1 INTRODUCTION

WIFIS is an IFS based on the FISICA image slicer provided by the University of Florida. Although the basic functionality of FISICA has already been confirmed in real observations with the FLAMINGOS spectrograph on the NOAO Kitt Peak 4-m telescope, it is imperative to perform thorough laboratory characterizations of FISICA, which will help WIFIS achieve the maximum efficiency. Here I present the results of the FISICA characterizations that I performed in a laboratory at the University of Toronto, focusing on how it maps an input 2-D field and also on the quality of the image that it delivers to the following collimator.

5.2 FISICA Characterization Configuration

5.2.1 Optical System for FISICA Characterization

As mentioned in §4.2.1, FISICA reduces the focal ratio of an input image from the re-imaging unit by half (e.g., $f/16$ to $f/8$) and reformats the input 2-D field into a long 1-D image which performs as a pseudo long-slit before the WIFIS collimator. The basic approach of the FISICA performance test is to illuminate it with an $f/16$ beam using a light source and to analyze its output image. Although FISICA is working in the NIR regime, I perform the test in the visible waveband since FISICA is purely composed of reflective surfaces. Figure 5.1 shows a block diagram of the test setup. The illumination assembly in the left, which houses a visible light-emitting diode (LED), acts as a light source that provides an image of an $f/16$ beam at the



Figure 5.1 Block diagram (top view) of the FISICA characterization test setup. The illumination assembly provides a uniformly illuminated integral field to FISICA. FISICA converts the input integral field and transfers it to an output pseudo long-slit. The camera unit images the output pseudo long-slit in series. The vertical arrow behind the camera unit indicates the degree of freedom in imaging the pseudo long-slit.

FISICA input plane. FISICA then transfers the input image from the illumination assembly into a pseudo long-slit, and the slit image is taken by the camera unit located after FISICA.

The illumination assembly, which has a unity magnification (i.e., the object size equals the image size), includes an object, an aperture stop and an achromatic doublet lens. The object is a light source with a size of $11 \text{ mm} \times 6 \text{ mm}$, which is designed to fully illuminate the FISICA input plane of $9.1 \text{ mm} \times 4.3 \text{ mm}$. The aperture stop is located at the focal point of the achromatic doublet and provides an $f/16$ output telecentric beam – the diameter of the aperture stop and focal length of the achromatic doublet are 52 mm and 3.2 mm , respectively. The telecentric nature of the output beam is helpful in verifying the focal ratio of the system (see § 5.2.2 for more information). The achromatic doublet, which mitigates the field curvature and distortion, focuses light after the aperture stop and forms an image of the object at the FISICA input plane.

I performed simulations using the Zemax software with the above optical components in order to finalize an optical system that can be used for laboratory FISICA characterizations. Figure 5.2 shows the resulting optical system, including the parameters of the optical components and the distances between them; Figure 5.3 shows spot diagrams (left panel) and the expected field curvature and distortion (right panel) obtained in Zemax for the final optical system. The RMS spot radius varies in the range of $8 - 25 \mu\text{m}$, which is a few times larger than the corresponding airy disk but is much smaller than the expected image size, showing that the effects of the optical aberrations are insignificant. This, together with the small field curvature and image distortion, suggests that the output image quality of the illumination assembly is

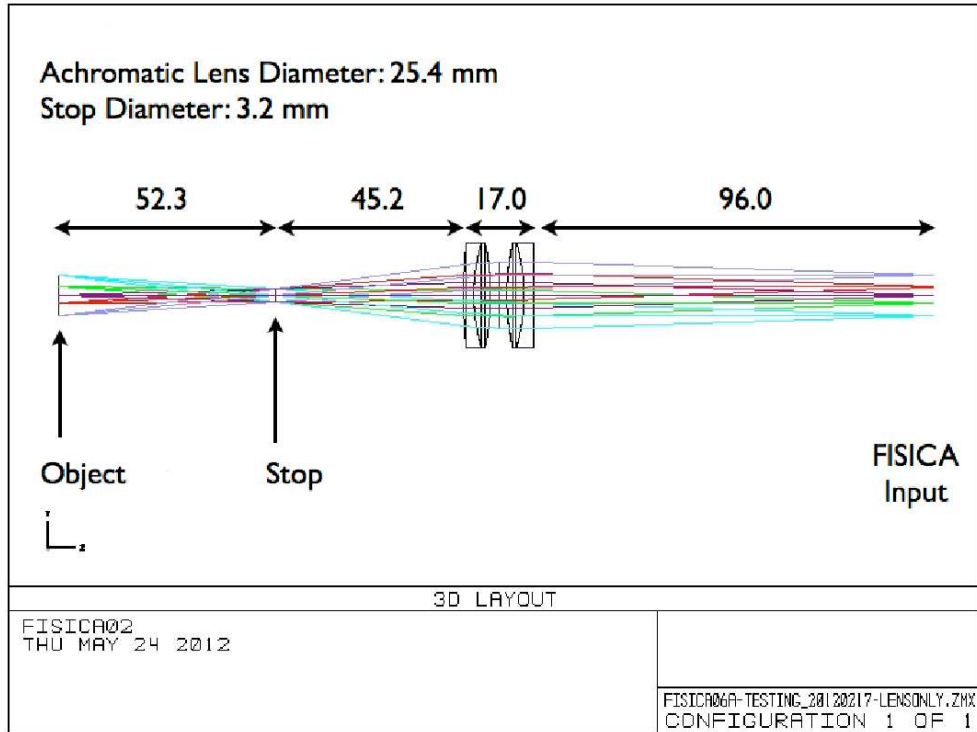


Figure 5.2 Side view of the optical layout of the illumination assembly for the FISICA characterization test. The illumination assembly, which has a unity magnification, is composed of an object, an aperture stop and an achromatic doublet. The object size in the Zemax simulation is set to be $11 \text{ mm} \times 6 \text{ mm}$, which is mean to fully illuminate the FISICA input plane of $9.1 \text{ mm} \times 4.3 \text{ mm}$.

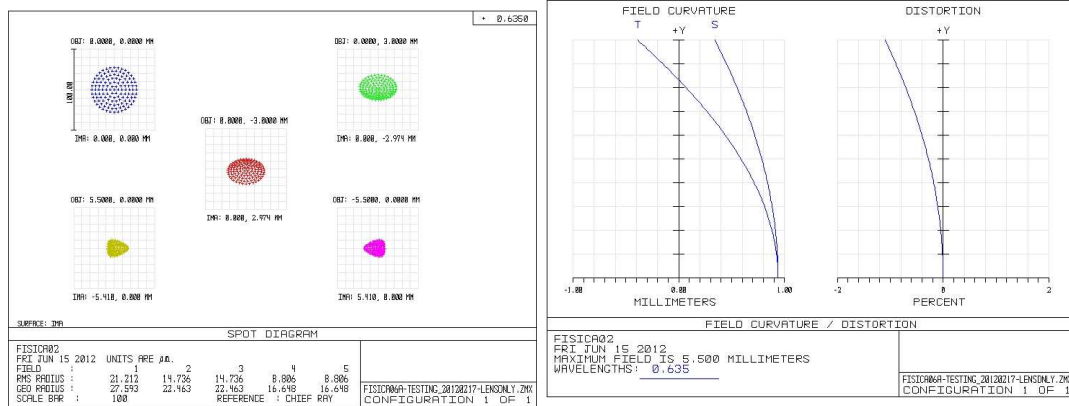


Figure 5.3 Left panel: Spot diagrams of the illumination assembly at the FISICA input plane. The full field size is $11 \text{ mm} \times 6 \text{ mm}$, which is slightly larger than the FISICA input plane of $9.1 \text{ mm} \times 4.3 \text{ mm}$. Field positions are defined at $(0,0)$, $(0,3)$, $(0,-3)$, $(5.5,0)$ and $(-5.5,0)$, respectively. The RMS spot radius ranges from $8 - 21 \text{ }\mu\text{m}$, which is a few times larger than the diffraction airy disk and much smaller than the output image size. This shows that the optical aberration of the illumination assembly is insignificant. Right panel: Field curvature and distortion of the illumination assembly output image. The field curvature is smaller than 0.4 mm and 1.0 mm in the sagittal and tangential directions. The image distortion is less than 1% . The low field curvature and image distortion show that the output image quality from the illumination assembly is sufficiently good for conducting the FISICA characterization test.

high enough for conducting the FISICA characterization test. The marginal ray angle (θ) at the FISICA input plane of the designed system is 1.76 degrees, which gives $\simeq 16.3$ working focal ratio ($\frac{1}{2 \sin \theta}$). This is consistent with the focal ratio of the input beam of FISICA for most cases of telescopic observations.

5.2.2 Laboratorial FISICA Characterization Setup

Figure 5.4 shows a photo of the real laboratory test setup that I used for the FISICA characterizations. In this setup, the illumination assembly consists of an engineered diffuser-based light source, an object location, an adjustable iris as a stop, and an achromatic doublet. The engineered diffuser-based light source, which is composed of a narrow angle LED and a 20 degree engineered diffuser followed by a piece of white paper, provides diffused, uniform illumination used in the test. The purpose of using the paper is to increase the diffusion of the light coming from the engineered diffuser. The object location is referred to a plane within the two-axes translational cage – I call it ‘object cage.’ The adjustable iris, which is located at the focal

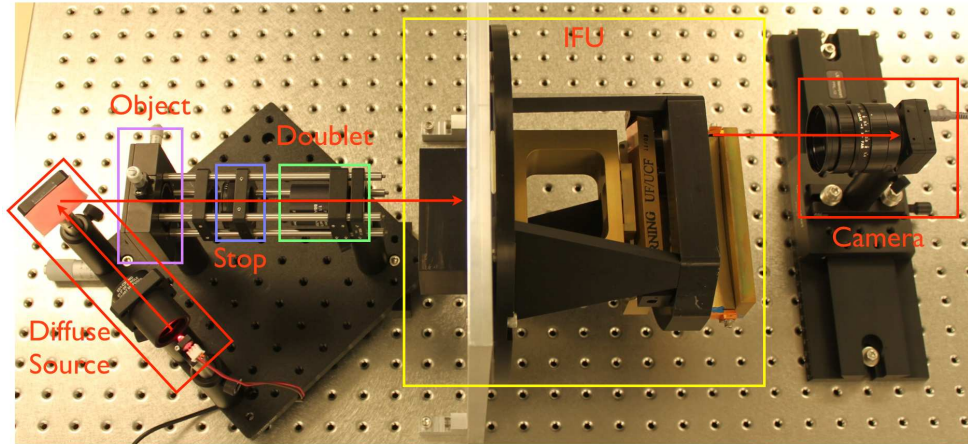


Figure 5.4 Configuration of the FISICA characterization setup (top view). The illumination assembly lies on the left hand side of the IFU FISICA provides an $f/16$ uniformly illuminated object image for FISICA. FISICA accepts an input 2-D image and creates an output 1-D pseudo long-slit. The camera unit behind FISICA takes images of the pseudo long-slit.

point of the achromatic doublet, serves as an aperture stop with an aperture size of 3.2 mm to provide telecentric beams. We use an off-the-shelf achromatic doublet available from the Thor Lab. to focus light at the FISICA input plane. The object cage, the adjustable iris and the achromatic doublet are all connected by four metal rods to ensure that they share the same optical axis. Overall, the distances between two adjacent components are carefully controlled at the millimeter precision level.

After the illumination assembly lies FISICA (§ 4.2.1) followed by the camera unit composed of a Fujinon C-mount camera lens and a Point Grey MP1.3 USB detector. The camera lens has a field of view of 10.0×7.5 degrees² and an adjustable focal ratio ranging from $f/1.4$ to $f/22$. The Point Grey detector has an array of 1296×964 pixels, corresponding to a physical size of $4.86 \text{ mm} \times 3.61 \text{ mm}$ for the given pixel size of $3.75 \mu\text{m}$. The camera lens and the Point Grey detector are installed on a 12" precision optical rail and a rail carrier which allows the camera unit to move along the horizontal direction of the pseudo long-slit to image the slit in series. The entire illumination assembly is mounted on an aluminum bread board, and two attached micrometer stages to the board provide the freedom of moving the assembly forward or backward.

One key feature of this test setup is the properties of the input beam from the illumination assembly – in other words, how closely can it represent a uniform $f/16$ beam? Figure 5.5 illustrates how we confirm the focal ratio of our test system by comparing focused (the small

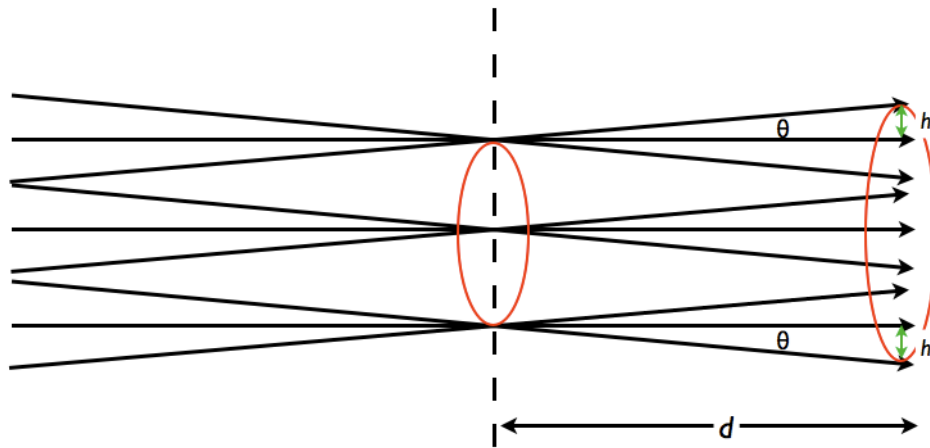


Figure 5.5 A schematic diagram illustrating how to measure the marginal ray angle (θ) of output beams, which is crucial to calculating its working focal ratio, on a telecentric optical system. The dashed line indicates the focal plane of the incoming beam and the small red circle in the middle represents the focused circular image. The larger red circle at a distance d away represents the defocused circular image. The marginal ray angle (θ) is a function of the distance (d) and the spread of the defocused image (h), which is indicated by green arrows. By measuring the values of h and d , the marginal angle θ can be derived using trigonometry functions.



Figure 5.6 Actual focused and defocused pinhole images taken by the camera unit. The defocused image is 7.7 mm away from the focused image plane.

red circle) and defocused (the large red circle) images of telecentric beams. As the distance (d) between the focused and defocused images increases, the defocused image gradually spreads out. For the telecentric incoming beams, the spread of the defocused image size (h , green arrows) is a function of d and the marginal ray angle (θ) as $\theta = \arctan(\frac{h}{d})$, and this gives an estimation of the working focal ratio.

Table 5.1 Centers and 3σ radii of focused and defocused pinhole images

	Center (pixel)	3σ Radii (μm)
Focused Image	(889, 572)	236
Defocused Image	(882, 567)	480

In practice, I placed a pinhole at the object location and took its focused and defocused images at two different locations separated by 7.7 mm. Figure 5.6 presents an example of the focused (left panel) and defocused (right panel) pinhole images; Table 5.1 summarizes their center coordinates and radii calculated by 2-D gaussian fittings. As in Table 5.1, there is an average offset of six pixels ($23 \mu\text{m}$) between the center coordinates of the focused and defocused pinhole images. This indicates that the focused and defocused pinhole images may not be concentric and subsequently that the output beams of the illumination assembly may not be perfectly telecentric. According to Zemax simulations, the offset of six pixels corresponds to 0.2 degrees deviation of the chief ray from the horizontal optical axis, which might have been caused by placing the aperture stop ~ 1 mm closer to the pinhole location. Also, the Zemax simulations show that the net effect of this 0.2 degrees offset is negligible in calculating the working focal ratio of the system as below. Given the distance $d = 7.7$ mm and the spread of

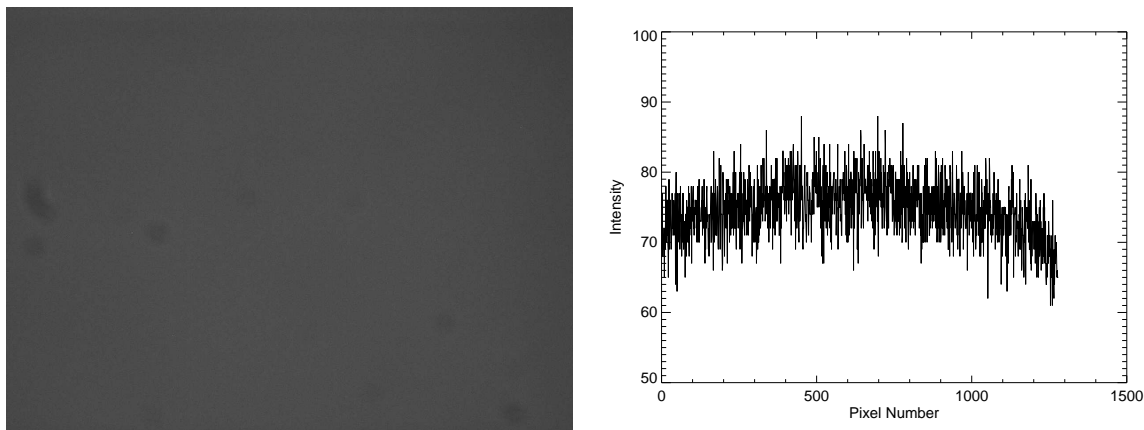


Figure 5.7 Left panel: image of the input integral field of FISICA provided by the illumination assembly. Right panel: the intensity profile obtained from a horizontal cut of the image shown in the left panel. The illumination provided by the illumination assembly is fairly uniform with an average data number of 75 ± 4 .

the defocused image $h = 244 \mu\text{m}$, the marginal ray angle is $\theta \simeq 1.81$ degrees. This results in a working focal ratio of $\simeq 16$, confirming that the focal ratio of the output beam of the test system is consistent with Zemax simulations and also with those of most of the FISICA input beam of expected real observations.

After the confirmation of the focal ratio of the output beam, the next step was to check the uniformity of the illumination. For this, the pinhole was removed from the object cage and the light from the diffuser light source directly illuminated the achromatic doublet. The image of roughly half of the input field of FISICA provided by the illumination assembly is shown in Figure 5.7 (left plane) – note that the detector size ($4.86 \text{ mm} \times 3.61 \text{ mm}$) is smaller than the FISICA input field size ($9.1 \text{ mm} \times 4.3 \text{ mm}$) – and Figure 5.7 (right panel) is the intensity profile of the image, showing that the intensity profile is quite uniform with the average data number of 75 ± 4 .

5.3 Results of Characterizations

There are three goals to achieve in the course of the FISICA characterizations: (a) to establish the mapping relation between the input 2-D field and the output 1-D pseudo long-slit and to validate the designed mapping relation (see below); (b) to confirm the magnification of FISICA; and (c) to evaluate the image quality of FISICA at the location of the pseudo long-slit.

21
19
17
15
13
11
9
7
5
3
1
2
4
6
8
10
12
14
16
18
20
22

22	21	20	19	18	17	16	15	14	13	12	11	10	9	8	7	6	5	4	3	2	1
----	----	----	----	----	----	----	----	----	----	----	----	----	---	---	---	---	---	---	---	---	---

Figure 5.8 The expected mapping relation between the input integral field and the output pseudo long-slit of FISICA. Note that the four shaded slices will not be used in WIFIS optical designs.

5.3.1 Mapping Relation

The first goal is to establish the mapping relation between the input 2-D field and the output 1-D pseudo long-slit and to validate that it is the same as the designed one. The method used to establish the mapping relation is to place a slit at the object location (which I call ‘object slit’) in the illumination assembly and to match the object slit in series to each of the slicer mirrors. By scanning through the slicer mirrors and recording the output locations of the pseudo long-slit, the mapping relation can be obtained. The width of the object slit was chosen to be $200 \mu\text{m}$ to match the angular width of each slicer mirror.

The designed mapping relation of FISICA originally from the University of Florida is presented in Figure 5.8. There are 22 stacked slicer mirrors (which appear as simple long rectangles for simplicity) labeled from 1 to 22, and these mirrors form the FISICA slicer array. The pseudo long-slit shown in the bottom of Figure 5.8 also consists of 22 segments which correspond to the 22 slicer mirrors. The center of the input field is mapped by the slicer mirrors 1 and 2 to the rightmost end of the pseudo long-slit; the top and bottom edges of the input field are mapped

by the slicer mirrors 21 and 22 to the leftmost end of the pseudo long-slit.

My laboratory establishment of the FISICA mapping relation started from illuminating the bottom of the FISICA input field (i.e., slicer mirror 22) and then moved to the adjacent fields by recording the locations of all the output fields. The result shows that the established mapping relation is the same as the designed one, which verifies the mapping relation of FISICA between the input 2-D field and the output 1-D pseudo long-slit.

5.3.2 Magnification of FISICA

FISICA is designed to accept $f/16$ beams and to create $f/8$ output beams, giving the magnification of 0.5. This expected magnification of 0.5 can be verified by comparing the width of the output pseudo long-slit to that of the input object slit. Figure 5.9, which is an image of the object slit recorded by the detector in the camera unit (see Figure 5.1), shows an example of our test of measuring the FISICA magnification. In Figure 5.9, the bright slit image near the center is the image of the object slit corresponding to one of the slicer mirrors. The other two faint slit images on the FISICA field array mirrors (i.e., circular mirrors in the background) are scattered light from the adjacent slicer mirrors. The diameter of this field mirror was manufactured to be 3 mm which amounts to 159 detector pixels in Figure 5.9, giving an $18.86 \mu\text{m}$ pixel scale. The object slit is $200 \mu\text{m}$ in size, whereas it spreads over five detector pixels on the pseudo long-slit, confirming the FISICA magnification of 0.5 as expected.

5.3.3 Image Quality of FISICA

The quality of the image made by FISICA at the location of the pseudo long-slit is important because it significantly affects the overall performance of the WIFIS instrument. Note that the main function of the WIFIS optical components is to disperse this image made by FISICA for spectroscopic information. Figure 5.10 shows our measurements of the width of each segment on the pseudo long-slit from each field of the slicer mirrors. In the bottom of Figure 5.10 lies the images of the whole 22 slices aligned in parallel by putting the images taken by the camera unit together. Figure 5.10 (top) presents the results of the analyses of these slit images: the black dots for the FWHM of the slit images and the red dots for the 80% encircled energy (here after EE80) radii. The slices of 1 – 10 show smaller widths compared with those of slices 11 – 22, implying that the center of the input field performs better than the edges of the input field. Overall, the average FWHM ($85 \mu\text{m}$) and the EE80 radius ($116 \mu\text{m}$) is more or less comparable to the expected slit width of $100 \mu\text{m}$ (i.e., object slit width times the FISICA magnification). The average EE80 radius is $\sim 20\%$ larger than the expected slit width, which is most likely due

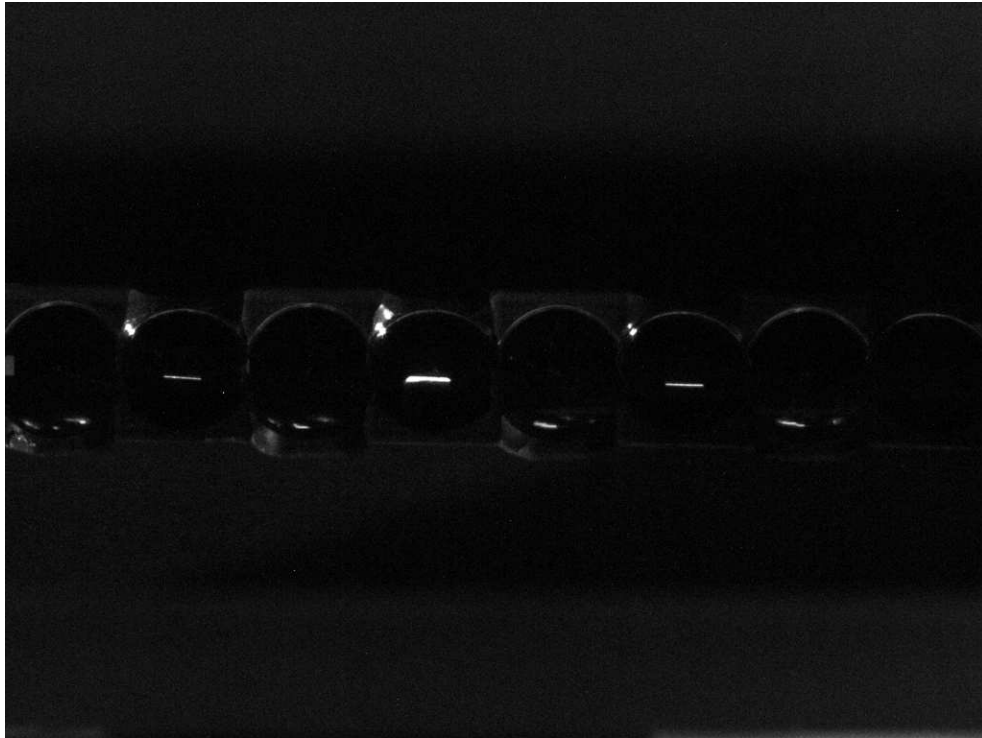


Figure 5.9 An image taken by the detector in the camera unit showing a single slicer mirror being illuminated. The circular mirrors in the background are images of FISICA field array mirrors. The bright slit image in the center corresponds to the slicer mirror being illuminated, and the other two dimmer slit images appear on the field mirrors are scattered light from the adjacent slicer mirrors. The pixel scale is obtained using the images of field array mirrors. The diameter of a field mirror is 3 mm, which corresponds to 159 pixels in the image and this gives a pixel scale of $18.86 \mu\text{m}$ per pixel. The slit width in this picture is 5 pixels or equivalent to $94 \mu\text{m}$, yielding a magnification of $\simeq 0.5$. Thus, the experimental FISICA magnification is consistent with the designed value.

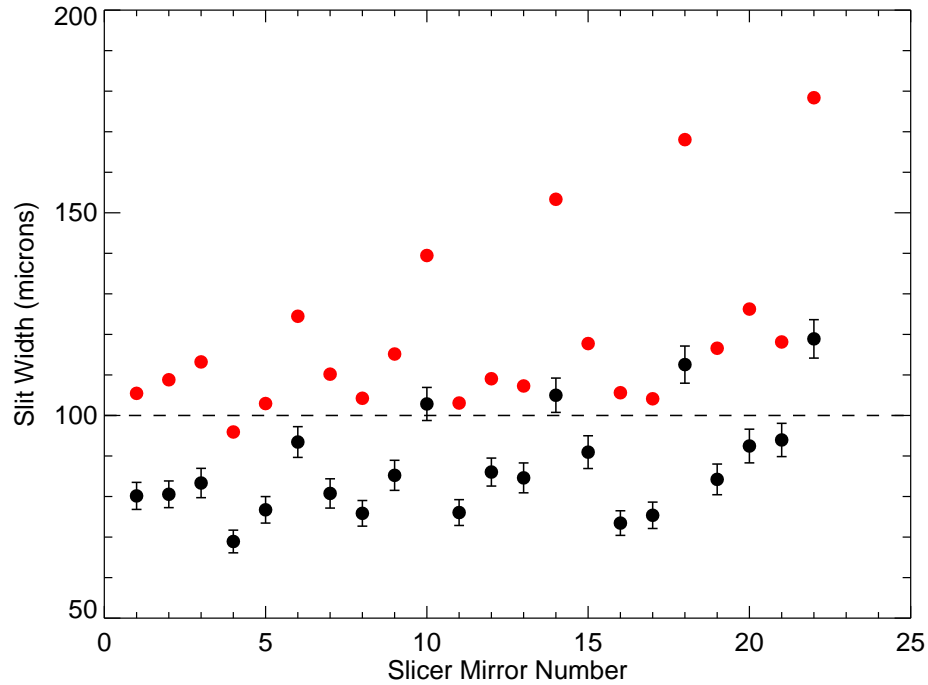


Figure 5.10 Top panel: FWHM (in black dots) and EE80 (in red dots) slit width along the pseudo long-slit. The dashed line represents the expected slit width ($100 \mu\text{m}$) provided by FISICA. The average FWHM and EE80 slit width is $85 \mu\text{m}$ and $116 \mu\text{m}$, respectively. Bottom panel: actual image of the output pseudo long-slit. The direction of the pseudo long-slit image is aligned to the horizontal axis of the top panel.

to the scattering of FISICA optics.

5.4 Summary and Conclusion

FISICA is an image slicer based IFU and is the heart of WIFIS. The main function of FISICA is to accept an input integral field (for example, $12'' \times 6''$ on a 10-meter telescope) and to transfer it to an output pseudo long-slit ($264'' \times 0''.27$ on a 10-meter telescope). We validate the designed mapping relation of FISICA by experimentally mapping an input integral field to an output pseudo long-slit for all of the 22 mirrors on the slicer array. The magnification made by FISICA was also experimentally measured to be 0.5, which is consistent with its designed goal. We also estimated the image quality of FISICA at the location of the pseudo long-slit as follows. The average FWHM ($85 \mu\text{m}$) and EE80 ($116 \mu\text{m}$) of the slit width are approximately consistent with the expected value of $100 \mu\text{m}$, and the FISICA image quality at the location of the pseudo long-slit is better at the center of the input field and it gets worse at the edges of the input field.

Chapter 6

Conclusions & Future Prospects

This thesis presents new results in the subjects of galaxy merger studies and the developments of NIR IFS. The merger studies provide clues to how star formation is triggered and quenched during galaxy-galaxy merging processes; the instrument developments give optical designs of a wide integral field infrared spectrograph that provides an unprecedented combination of etendue and spectral resolving power, as well as characterization results of some of the key components of the spectrograph.

6.1 Thesis Summary

This section summarizes the conclusions of each chapter.

Chapter 2:

- I constrain the space density evolution of so called ‘wet’ and ‘dry’ mergers up to $z \sim 0.7$ using the 1298 merging galaxies presented in Bridge et al. (2010). These mergers are selected based on clear tidal features and are believed to be mergers at late merging stages. Although the space density of total mergers shows a mild evolution, wet and dry merging populations show different evolutionary trends.
- The present space density of massive galaxy mergers is already similar (within a factor of three) to that of *existing* massive elliptical galaxies. This suggests that not all of the massive major mergers will end up with massive early-type galaxies, unless the merging timescale is much longer than expected. On the other hand, low stellar mass elliptical galaxies ($M_{\text{stellar}} < 10^{10.5} M_{\odot}$) have a space density consistent with hierarchical formation via mergers.

Chapter 3:

- I constrain the rate of dry mergers at medium redshift using ~ 2800 spectra of close pair galaxy candidates with $0.1 < z < 1.2$ identified from CFHTLS fields. These candidate pairs are systems most likely to be seen at early merging stages. After data reduction, 148 close pair candidates (296 galaxies) were obtained with confident redshift measurements for both pair members. Physical pairs were selected from these candidate pairs based on the corresponding virial radii of each system, and around 1/5 of our candidate pairs (30 pairs) are likely to be physically associated and share a common dark matter halo. These pairs are divided into red-red, blue-red and blue-blue systems based on rest-frame $g' - i'$ colors, using the classification method introduced in Chou et al. (2011).
- The fraction of blue-blue pairs is significantly greater than that of red-red and blue-red pairs after correcting for known selection effects. Given fairly liberal rest-frame color selection criteria in selecting red galaxies, red-red pairs are almost entirely absent from our sample, suggesting that red early-phase mergers are rare at $z \sim 0.5$. This result supports models with a short merging timescale (< 0.5 Gyr) in which star-formation is enhanced in the early phase of mergers, but quenched in the late phase of mergers. Hot halo models may explain this behavior if virial shocks that heat gas are inefficient until mergers are nearly complete.

Chapter 4:

- I developed optical designs of a Wide Integral Field Infrared Spectrograph which can provide the largest etendue with comparable spectral resolving powers among currently available NIR IFs. The two versions of the WIFIS optical designs, WIFIS1 and WIFIS2, were developed for different science goals, providing a $12'' \times 5''$ integral FOV on a 10-m telescope, or equivalently a $52'' \times 20''$ FOV on a 2.3-m telescope.
- WIFIS1 provides a spectral resolving power $R \sim 5,500$ in each of JHK bands in a single exposure; WIFIS2 does $R \sim 3,000$ in zJ ($0.9 - 1.3 \mu\text{m}$) and H bands ($1.3 - 1.8 \mu\text{m}$).
- The expected system performance of the WIFIS designs are investigated based on the effects of the optical aberrations, seeing broadening, fabrication and alignment errors, and thermal environments. Our analyses show that both the WIFIS designs can provide system performances comparable with the instrument designed goals in most of the covered wavelength range except for the 10% and 30% lower spectral resolving power of WIFIS1 in K band and WIFIS2 in H band, respectively.

- Potential scientific applications of WIFIS include 2-D spectroscopic studies of galaxy mergers, star-forming galaxies, local galaxies, Galactic star-forming regions and supernova remnants.

Chapter 5:

- FISICA is an image slicer-based integral field unit and is the heart of WIFIS. The main function of FISICA is to accept an input integral field (for example, $12'' \times 6''$ on a 10-meter telescope) and to transfer it to an output pseudo long-slit ($264 \times 0''.27$ on a 10-m telescope).
- I validate the designed mapping relation of FISICA by experimentally mapping an input integral field into an output pseudo long-slit for all of the 22 mirrors of FISICA slicer array. The magnification of FISICA is also experimentally measured to be 0.5, which is consistent with its design goal.
- I also estimate the image quality of FISICA at the location of the pseudo long-slit. The image quality of the pseudo long-slit is quantified by calculating the Gaussian FWHM and EE80 slit width along the entire pseudo long-slit. The average FWHM ($\simeq 85 \mu\text{m}$) and EE80 ($\simeq 116 \mu\text{m}$) of the slit width are approximately consistent with the expected value of $100 \mu\text{m}$. The FISICA image quality at the location of the pseudo long-slit is better at the center of the input field, and becomes worse at the edge of the input field.

6.2 Future Work

This section briefly outlines my immediate future research plans based on the work presented in this thesis. First, I plan to continuously participate in the development of WIFIS to the completion of the instrument and to commission WIFIS on the Bok 2.3-m telescope in summer 2013. Secondly, once WIFIS is commissioned, I plan to conduct a NIR 2-D spectroscopic survey of galaxy mergers at medium redshifts ($z \sim 0.5$) to investigate their star formation histories and kinematic properties.

6.2.1 Completion of WIFIS

Here I give a list of important steps which are necessary in the completion of WIFIS. First, all the remaining WIFIS optical components need to be fabricated and tested. Secondly, many of the mechanical components (e.g., lens and mirror holders, cryostats) need to be designed and manufactured. Thirdly, the ongoing H2RG detector test needs to be finished. We plan to

develop WIFIS based on WIFIS2 design first which will be followed by WIFIS1-based spectrograph in a few years.

Among all these steps, the first step is to have all the remaining WIFIS optical components fabricated and tested. Currently some of the WIFIS components (e.g., IFU FISICA, gratings and mirrors) have been fully manufactured and delivered, except for the WIFIS lenses. The WIFIS lenses are being fabricated, and we expect its delivery in October 2012. I have been involved in the characterizations of the manufactured optical components conducted in the laboratory of the University of Toronto and expect to finish the characterizations of all the WIFIS optical components by the end of 2012.

The second step is to have the mechanical components designed and fabricated. I have been intensively working together with the company PulseRay for design and fabrication details of the mechanical components. I expect the mechanical components to be fully fabricated under our supervision and guidance in early 2013.

The H2RG detector has also been intensively characterized in the laboratory. We have established the cooling and warming procedures of the detector, satisfying the temperature gradient requirements specified by the vendor of the detector (i.e., Teledyne Inc.). I expect the characterization of the H2RG detector to be completed by the end of 2012.

The final step will be the assembly of all WIFIS2-based WIFIS components and subsequent laboratory tests of the system performance. I will participate in the assembly process as well as the system performance tests, and expect to commission WIFIS on the Bok telescope in Arizona to have first light in summer/fall 2013.

6.2.2 A 2-D NIR Spectroscopic Survey of Medium-Redshift Merging Galaxies

One of the best ways to study the star formation histories of extended sources like galaxy mergers is through 2-D spectra obtained by integral-field spectroscopy observations. By modelling the star formation histories of different resolved stellar populations (see Fig. 6.1 for an example) using stellar population synthesis codes (e.g., Bruzual & Charlot 03), such one can investigate how star formation was triggered by the latest merging process. Stellar population modelling can also yield good constraints on galaxy merging timescales, which are notoriously poorly understood yet a major source of uncertainty in studying merger rate density evolution. If the development of WIFIS proceeds smoothly, I will propose a NIR spectroscopic survey mainly targeting at the rest-frame H_α line emission for lower redshift galaxy mergers (i.e., $0.4 < z < 0.6$). Since these low- z mergers are tend to be brighter and sustain larger angular areas

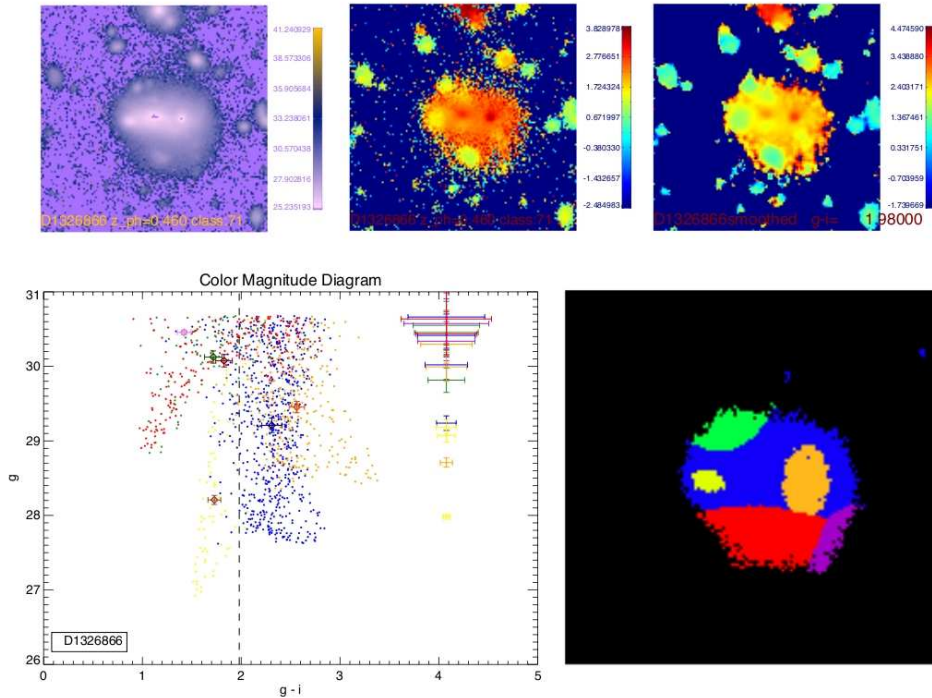


Figure 6.1 Resolved pixel-by-pixel colors of one typical galaxy merger (D1326866) in our CFHTLS sample. The top left, middle and right panel shows the CFHTLS i' band image, the $g' - i'$ and $g' - i'$ smoothed (2 pixels) color maps, respectively. The physical size of each top panel map is 100×100 kpc. In the bottom right panel, this merger is divided into several segments based on the $g' - i'$ color discontinuity between stellar populations. In the bottom left panel, data points of the merger are plotted on a color magnitude diagram (CMD). Different colors on the CMD correspond to the color-coded segments of the galaxy. The error bars on the right hand side show the color coded errors of the corresponding data points on CMD with respect to g' band magnitudes. The dashed line on the CMD is the color bimodality line that divides the pixels within the merger into blue and red categories. Note that the photo- z of the merger is 0.46, which implies that the galaxy merger extends $\sim 10''$ on the sky. With the integral-field of view ($52'' \times 20''$) provided by the WIFIS-Bok 2.3-m telescope combination, the galaxy merger can be fully covered in a single pointing and the stellar populations isolated chromatically can be studied spectroscopically.

in the sky, these are more suitable for spectroscopic observations conducted by small telescopes. Afterwards WIFIS will be commissioned on the 10-m Gran Telescopio Canarias (GTC), and I plan to continue the survey to study galaxy mergers at higher redshift ranges ($0.6 < z < 1.0$). Based on the expected WIFIS sensitivity mentioned in §4.5 and the z' band photometry from the CFHTLS Deep survey, the WIFIS-Bok combination could detect the bright galaxy mergers within the redshift range $z = 0.4 - 0.6$, while the WIFIS-GTC combination are sensitive enough to detect most of the galaxy mergers presented in the CFHTLS merger catalog (see §2.2) out to $z = 1.0$.

Bibliography

- Abraham, R. G., Glazebrook, K., McCarthy, P. J., Crampton, D., Murowinski, R., Jørgensen, I., Roth, K., Hook, I. M., Savaglio, S., Chen, H.-W., Marzke, R. O., & Carlberg, R. G. 2004, *AJ*, 127, 2455
- Abraham, R. G., Nair, P., McCarthy, P. J., Glazebrook, K., Mentuch, E., Yan, H., Savaglio, S., Crampton, D., Murowinski, R., Juneau, S., Le Borgne, D., Carlberg, R. G., Jørgensen, I., Roth, K., Chen, H.-W., & Marzke, R. O. 2007, *ApJ*, 669, 184
- Abraham, R. G., Tanvir, N. R., Santiago, B. X., Ellis, R. S., Glazebrook, K., & van den Bergh, S. 1996, *MNRAS*, 279, L47
- Abraham, R. G., Valdes, F., Yee, H. K. C., & van den Bergh, S. 1994, *ApJ*, 432, 75
- Abraham, R. G., van den Bergh, S., & Nair, P. 2003, *ApJ*, 588, 218
- Allington-Smith, J. & Content, R. 1998, *PASP*, 110, 1216
- Allington-Smith, J. R., Content, R., Haynes, R., & Lewis, I. J. 1997, in Presented at the Society of Photo-Optical Instrumentation Engineers (SPIE) Conference, Vol. 2871, Society of Photo-Optical Instrumentation Engineers (SPIE) Conference Series, ed. A. L. Ardeberg, 1284–1294
- Bacon, R., Adam, G., Baranne, A., Courtes, G., Dubet, D., Dubois, J. P., Emsellem, E., Ferruit, P., Georgelin, Y., Monnet, G., Pecontal, E., Rousset, A., & Say, F. 1995, *A&AS*, 113, 347
- Baldry, I. K., Glazebrook, K., Brinkmann, J., Ivezić, Ž., Lupton, R. H., Nichol, R. C., & Szalay, A. S. 2004, *ApJ*, 600, 681
- Ball, N. M., Loveday, J., Brunner, R. J., Baldry, I. K., & Brinkmann, J. 2006, *MNRAS*, 373, 845
- Balogh, M. L., Baldry, I. K., Nichol, R., Miller, C., Bower, R., & Glazebrook, K. 2004, *ApJ*, 615, L101

- Barden, S. C. & Wade, R. A. 1988, in *Astronomical Society of the Pacific Conference Series*, Vol. 3, *Fiber Optics in Astronomy*, ed. S. C. Barden, 113–124
- Barton, E. J., Geller, M. J., & Kenyon, S. J. 2000, *ApJ*, 530, 660
- Bell, E. F., Naab, T., McIntosh, D. H., Somerville, R. S., Caldwell, J. A. R., Barden, M., Wolf, C., Rix, H., Beckwith, S. V., Borch, A., Häussler, B., Heymans, C., Jahnke, K., Jogee, S., Kopolov, S., Meisenheimer, K., Peng, C. Y., Sanchez, S. F., & Wisotzki, L. 2006, *ApJ*, 640, 241
- Bell, E. F., Wolf, C., Meisenheimer, K., Rix, H.-W., Borch, A., Dye, S., Kleinheinrich, M., Wisotzki, L., & McIntosh, D. H. 2004, *ApJ*, 608, 752
- Bell, E. F., Zheng, X. Z., Papovich, C., Borch, A., Wolf, C., & Meisenheimer, K. 2007, *ApJ*, 663, 834
- Bershady, M. A., Jangren, A., & Conselice, C. J. 2000, *AJ*, 119, 2645
- Bertin, E. & Arnouts, S. 1996, *A&AS*, 117, 393
- Bielby, R., Hudelot, P., McCracken, H. J., Ilbert, O., Daddi, E., Le Fèvre, O., Gonzalez-Perez, V., Kneib, J.-P., Marmo, C., Mellier, Y., Salvato, M., Sanders, D. B., & Willott, C. J. 2011, *ArXiv e-prints*
- Birnboim, Y. & Dekel, A. 2003, *MNRAS*, 345, 349
- Birnboim, Y., Dekel, A., & Neistein, E. 2007, *MNRAS*, 380, 339
- Blanton, M. R. 2006, *ApJ*, 648, 268
- Blanton, M. R., Hogg, D. W., Bahcall, N. A., Baldry, I. K., Brinkmann, J., Csabai, I., Eisenstein, D., Fukugita, M., Gunn, J. E., Ivezić, Ž., Lamb, D. Q., Lupton, R. H., Loveday, J., Munn, J. A., Nichol, R. C., Okamura, S., Schlegel, D. J., Shimasaku, K., Strauss, M. A., Vogeley, M. S., & Weinberg, D. H. 2003, *ApJ*, 594, 186
- Bluck, A. F. L., Conselice, C. J., Buitrago, F., Grützbauch, R., Hoyos, C., Mortlock, A., & Bauer, A. E. 2012, *ApJ*, 747, 34
- Blumenthal, G. R., Faber, S. M., Primack, J. R., & Rees, M. J. 1984, *Nature*, 311, 517
- Bohlin, R. C., Colina, L., & Finley, D. S. 1995, *AJ*, 110, 1316
- Böker, T., Falcón-Barroso, J., Schinnerer, E., Knapen, J. H., & Ryder, S. 2008, *AJ*, 135, 479

- Bolzonella, M., Miralles, J., & Pelló, R. 2000, *A&A*, 363, 476
- Bouché, N., Dekel, A., Genzel, R., Genel, S., Cresci, G., Förster Schreiber, N. M., Shapiro, K. L., Davies, R. I., & Tacconi, L. 2010, *ApJ*, 718, 1001
- Boulade, O., Charlot, X., Abbon, P., Aune, S., Borgeaud, P., Carton, P.-H., Carty, M., Da Costa, J., Deschamps, H., Desforge, D., Eppellé, D., Gallais, P., Gosset, L., Granelli, R., Gros, M., de Kat, J., Loiseau, D., Ritou, J.-., Roussé, J. Y., Starzynski, P., Vignal, N., & Vigroux, L. G. 2003, in *Society of Photo-Optical Instrumentation Engineers (SPIE) Conference Series*, Vol. 4841, *Society of Photo-Optical Instrumentation Engineers (SPIE) Conference Series*, ed. M. Iye & A. F. M. Moorwood, 72–81
- Bournaud, F., Dekel, A., Teyssier, R., Cacciato, M., Daddi, E., Juneau, S., & Shankar, F. 2011, *ApJ*, 741, L33
- Bowen, I. S. 1938, *ApJ*, 88, 113
- Brammer, G. B., Whitaker, K. E., van Dokkum, P. G., Marchesini, D., Franx, M., Kriek, M., Labbé, I., Lee, K.-S., Muzzin, A., Quadri, R. F., Rudnick, G., & Williams, R. 2011, *ApJ*, 739, 24
- Bridge, C. R., Appleton, P. N., Conselice, C. J., Choi, P. I., Armus, L., Fadda, D., Laine, S., Marleau, F. R., Carlberg, R. G., Helou, G., & Yan, L. 2007, *ApJ*, 659, 931
- Bridge, C. R., Carlberg, R. G., & Sullivan, M. 2010, *ApJ*, 709, 1067
- Brinchmann, J., Abraham, R., Schade, D., Tresse, L., Ellis, R. S., Lilly, S., Le Fevre, O., Glazebrook, K., Hammer, F., Colless, M., Crampton, D., & Broadhurst, T. 1998, *ApJ*, 499, 112
- Bronder, T. J., Hook, I. M., Astier, P., Balam, D., Balland, C., Basa, S., Carlberg, R. G., Conley, A., Fouchez, D., Guy, J., Howell, D. A., Neill, J. D., Pain, R., Perrett, K., Pritchet, C. J., Regnault, N., Sullivan, M., Baumont, S., Fabbro, S., Filliol, M., Perlmutter, S., & Ripoche, P. 2008, *A&A*, 477, 717
- Brooks, A. M., Governato, F., Quinn, T., Brook, C. B., & Wadsley, J. 2009, *ApJ*, 694, 396
- Brown, M. J. I., Dey, A., Jannuzi, B. T., Brand, K., Benson, A. J., Brodwin, M., Croton, D. J., & Eisenhardt, P. R. 2007, *ApJ*, 654, 858
- Brown, W. R., Epps, H. W., & Fabricant, D. G. 2004, *PASP*, 116, 833
- Bruzual, G. & Charlot, S. 2003, *MNRAS*, 344, 1000

- Bundy, K., Ellis, R. S., & Conselice, C. J. 2005, *ApJ*, 625, 621
- Bundy, K., Fukugita, M., Ellis, R. S., Kodama, T., & Conselice, C. J. 2004, *ApJ*, 601, L123
- Bundy, K., Fukugita, M., Ellis, R. S., Targett, T. A., Belli, S., & Kodama, T. 2009, *ApJ*, 697, 1369
- Bundy, K., Scarlata, C., Carollo, C. M., Ellis, R. S., Drory, N., Hopkins, P., Salvato, M., Leauthaud, A., Koekemoer, A. M., Murray, N., Ilbert, O., Oesch, P., Ma, C.-P., Capak, P., Pozzetti, L., & Scoville, N. 2010, *ApJ*, 719, 1969
- Cassata, P., Cimatti, A., Franceschini, A., Daddi, E., Pignatelli, E., Fasano, G., Rodighiero, G., Pozzetti, L., Mignoli, M., & Renzini, A. 2005, *MNRAS*, 357, 903
- Cattaneo, A., Dekel, A., Devriendt, J., Guiderdoni, B., & Blaizot, J. 2006, *MNRAS*, 370, 1651
- Ceverino, D. & Klypin, A. 2009, *ApJ*, 695, 292
- Chester, C. & Roberts, M. S. 1964, *AJ*, 69, 635
- Chou, R. C. Y., Bridge, C. R., & Abraham, R. G. 2011, *AJ*, 141, 87
- Cole, S., Helly, J., Frenk, C. S., & Parkinson, H. 2008, *MNRAS*, 383, 546
- Conroy, C., Wechsler, R. H., & Kravtsov, A. V. 2007, *ApJ*, 668, 826
- Conselice, C. J. 2003, *ApJS*, 147, 1
- . 2006, *ApJ*, 638, 686
- Conselice, C. J., Bershadsky, M. A., Dickinson, M., & Papovich, C. 2003, *AJ*, 126, 1183
- Conselice, C. J., Bershadsky, M. A., & Jangren, A. 2000, *ApJ*, 529, 886
- Conselice, C. J., Bluck, A. F. L., Buitrago, F., Bauer, A. E., Grützbauch, R., Bouwens, R. J., Bevan, S., Mortlock, A., Dickinson, M., Daddi, E., Yan, H., Scott, D., Chapman, S. C., Chary, R.-R., Ferguson, H. C., Giavalisco, M., Grogin, N., Illingworth, G., Jogee, S., Koekemoer, A. M., Lucas, R. A., Mobasher, B., Moustakas, L., Papovich, C., Ravindranath, S., Siana, B., Teplitz, H., Trujillo, I., Urry, M., & Weinzierl, T. 2011, *MNRAS*, 413, 80
- Conselice, C. J., Rajgor, S., & Myers, R. 2008, *MNRAS*, 386, 909
- Content, R. 1997, in *Society of Photo-Optical Instrumentation Engineers (SPIE) Conference Series*, Vol. 2871, *Society of Photo-Optical Instrumentation Engineers (SPIE) Conference Series*, ed. A. L. Ardeberg, 1295–1305

- Coppa, G., Mignoli, M., Zamorani, G., Bardelli, S., Lilly, S. J., Bolzonella, M., Scodreggio, M., Vergani, D., Nair, P., Pozzetti, L., Cimatti, A., Zucca, E., Carollo, C. M., Contini, T., Le Fèvre, O., Renzini, A., Mainieri, V., Bongiorno, A., Caputi, K. I., Cucciati, O., de la Torre, S., de Ravel, L., Franzetti, P., Garilli, B., Memeo, P., Iovino, A., Kampczyk, P., Kneib, J.-P., Knobel, C., Koekemoer, A. M., Kovač, K., Lamareille, F., Le Borgne, J.-F., Le Brun, V., Maier, C., Pellò, R., Peng, Y., Perez-Montero, E., Ricciardelli, E., Scarlata, C., Silverman, J. D., Tanaka, M., Tasca, L., Tresse, L., Abbas, U., Bottini, D., Capak, P., Cappi, A., Cassata, P., Fumana, M., Guzzo, L., Leauthaud, A., Maccagni, D., Marinoni, C., Meneux, B., Oesch, P., Porciani, C., Scaramella, R., & Scoville, N. 2011, *A&A*, 535, A10
- Cowie, L. L. & Barger, A. J. 2008, *ApJ*, 686, 72
- Cox, T. J., Jonsson, P., Primack, J. R., & Somerville, R. S. 2006, *MNRAS*, 373, 1013
- Crocker, A., Krips, M., Bureau, M., Young, L. M., Davis, T. A., Bayet, E., Alatalo, K., Blitz, L., Bois, M., Bournaud, F., Cappellari, M., Davies, R. L., de Zeeuw, P. T., Duc, P.-A., Emsellem, E., Khochfar, S., Krajnović, D., Kuntschner, H., Lablanche, P.-Y., McDermid, R. M., Morganti, R., Naab, T., Oosterloo, T., Sarzi, M., Scott, N., Serra, P., & Weijmans, A.-M. 2012, *MNRAS*, 2291
- Croton, D. J., Springel, V., White, S. D. M., De Lucia, G., Frenk, C. S., Gao, L., Jenkins, A., Kauffmann, G., Navarro, J. F., & Yoshida, N. 2006, *MNRAS*, 365, 11
- da Costa, L. N., Willmer, C. N. A., Pellegrini, P. S., Chaves, O. L., Rité, C., Maia, M. A. G., Geller, M. J., Latham, D. W., Kurtz, M. J., Huchra, J. P., Ramella, M., Fairall, A. P., Smith, C., & Lípári, S. 1998a, *AJ*, 116, 1
- . 1998b, *AJ*, 116, 1
- Dasyra, K. M., Tacconi, L. J., Davies, R. I., Naab, T., Genzel, R., Lutz, D., Sturm, E., Baker, A. J., Veilleux, S., Sanders, D. B., & Burkert, A. 2006, *ApJ*, 651, 835
- Davis, M., Efstathiou, G., Frenk, C. S., & White, S. D. M. 1985, *ApJ*, 292, 371
- Davis, M., Faber, S. M., Newman, J., Phillips, A. C., Ellis, R. S., Steidel, C. C., Conselice, C., Coil, A. L., Finkbeiner, D. P., Koo, D. C., Guhathakurta, P., Weiner, B., Schiavon, R., Willmer, C., Kaiser, N., Luppino, G. A., Wirth, G., Connolly, A., Eisenhardt, P., Cooper, M., & Gerke, B. 2003, in Presented at the Society of Photo-Optical Instrumentation Engineers (SPIE) Conference, Vol. 4834, Society of Photo-Optical Instrumentation Engineers (SPIE) Conference Series, ed. P. Guhathakurta, 161–172

- De Propriis, R., Conselice, C. J., Liske, J., Driver, S. P., Patton, D. R., Graham, A. W., & Allen, P. D. 2007, *ApJ*, 666, 212
- De Propriis, R., Driver, S. P., Colless, M. M., Drinkwater, M. J., Ross, N. P., Bland-Hawthorn, J., York, D. G., & Pimbblet, K. 2010, *ArXiv e-prints*
- de Ravel, L., Le Fèvre, O., Tresse, L., Bottini, D., Garilli, B., Le Brun, V., Maccagni, D., Scaramella, R., Scodreggio, M., Vettolani, G., Zanichelli, A., Adami, C., Arnouts, S., Bardelli, S., Bolzonella, M., Cappi, A., Charlot, S., Ciliegi, P., Contini, T., Foucaud, S., Franzetti, P., Gavignaud, I., Guzzo, L., Ilbert, O., Iovino, A., Lamareille, F., McCracken, H. J., Marano, B., Marinoni, C., Mazure, A., Meneux, B., Merighi, R., Paltani, S., Pellò, R., Pollo, A., Pozzetti, L., Radovich, M., Vergani, D., Zamorani, G., Zucca, E., Bondi, M., Bongiorno, A., Brinchmann, J., Cucciati, O., de La Torre, S., Gregorini, L., Memeo, P., Perez-Montero, E., Mellier, Y., Merluzzi, P., & Tempurin, S. 2009, *A&A*, 498, 379
- de Vaucouleurs, G., de Vaucouleurs, A., Corwin, Jr., H. G., Buta, R. J., Paturel, G., & Fouque, P. 1991, *Third Reference Catalogue of Bright Galaxies*
- de Vaucouleurs, G., de Vaucouleurs, A., & Corwin, J. R. 1976a, in *Second reference catalogue of bright galaxies, 1976*, Austin: University of Texas Press., 0
- de Vaucouleurs, G., de Vaucouleurs, A., & Corwin, J. R. 1976b, in *Second reference catalogue of bright galaxies, 1976*, Austin: University of Texas Press., 0–+
- Dekel, A. & Birnboim, Y. 2006, *MNRAS*, 368, 2
- Dekel, A., Sari, R., & Ceverino, D. 2009, *ApJ*, 703, 785
- Desai, V., Dey, A., Cohen, E., Le Floch, E., & Soifer, B. T. 2011, *ApJ*, 730, 130
- Di Matteo, P., Bournaud, F., Martig, M., Combes, F., Melchior, A., & Semelin, B. 2008, *A&A*, 492, 31
- Di Matteo, P., Combes, F., Melchior, A.-L., & Semelin, B. 2007, *A&A*, 468, 61
- Di Matteo, T., Springel, V., & Hernquist, L. 2005, *Nature*, 433, 604
- Diego, F. 1993, *Appl.Optics*, 32, 6284
- Doi, M., Fukugita, M., & Okamura, S. 1993, *MNRAS*, 264, 832
- Driver, S. P., Allen, P. D., Graham, A. W., Cameron, E., Liske, J., Ellis, S. C., Cross, N. J. G., De Propriis, R., Phillipps, S., & Couch, W. J. 2006, *MNRAS*, 368, 414

- Driver, S. P., Liske, J., Cross, N. J. G., De Propriis, R., & Allen, P. D. 2005, *MNRAS*, 360, 81
- Eggen, O. J., Lynden-Bell, D., & Sandage, A. R. 1962, *ApJ*, 136, 748
- Eikenberry, S., Elston, R., Raines, S. N., Julian, J., Hanna, K., Hon, D., Julian, R., Bandyopadhyay, R., Bennett, J. G., Bessoff, A., Branch, M., Corley, R., Eriksen, J.-D., Frommeyer, S., Gonzalez, A., Herlevich, M., Marin-Franch, A., Marti, J., Murphey, C., Rashkin, D., Warner, C., Leckie, B., Gardhouse, W. R., Fletcher, M., Dunn, J., Wooff, R., & Hardy, T. 2006, in *Society of Photo-Optical Instrumentation Engineers (SPIE) Conference Series*, Vol. 6269, *Society of Photo-Optical Instrumentation Engineers (SPIE) Conference Series*
- Eikenberry, S. S., Elston, R., Guzman, R., Julian, J., Raines, S. N., Gruel, N., Boreman, G., Glenn, P. E., Hull-Allen, C. G., Hoffman, J., Rodgers, M., Thompson, K., Flint, S., Comstock, L., & Myrick, B. 2004, in *Presented at the Society of Photo-Optical Instrumentation Engineers (SPIE) Conference*, Vol. 5492, *Society of Photo-Optical Instrumentation Engineers (SPIE) Conference Series*, ed. A. F. M. Moorwood & M. Iye, 1264–1273
- Ellison, S. L., Patton, D. R., Mendel, J. T., & Scudder, J. M. 2011, *MNRAS*, 418, 2043
- Elmegreen, D. M., Elmegreen, B. G., Ravindranath, S., & Coe, D. A. 2007, *ApJ*, 658, 763
- Elmegreen, D. M., Elmegreen, B. G., & Sheets, C. M. 2004, *ApJ*, 603, 74
- Faber, S. M., Willmer, C. N. A., Wolf, C., Koo, D. C., Weiner, B. J., Newman, J. A., Im, M., Coil, A. L., Conroy, C., Cooper, M. C., Davis, M., Finkbeiner, D. P., Gerke, B. F., Gebhardt, K., Groth, E. J., Guhathakurta, P., Harker, J., Kaiser, N., Kassin, S., Kleinheinrich, M., Konidaris, N. P., Kron, R. G., Lin, L., Luppino, G., Madgwick, D. S., Meisenheimer, K., Noeske, K. G., Phillips, A. C., Sarajedini, V. L., Schiavon, R. P., Simard, L., Szalay, A. S., Vogt, N. P., & Yan, R. 2007, *ApJ*, 665, 265
- Felten, J. E. 1977, *AJ*, 82, 861
- Fioc, M. & Rocca-Volmerange, B. 1997, *A&A*, 326, 950
- Förster Schreiber, N. M., Genzel, R., Bouché, N., Cresci, G., Davies, R., Buschkamp, P., Shapiro, K., Tacconi, L. J., Hicks, E. K. S., Genel, S., Shapley, A. E., Erb, D. K., Steidel, C. C., Lutz, D., Eisenhauer, F., Gillessen, S., Sternberg, A., Renzini, A., Cimatti, A., Daddi, E., Kurk, J., Lilly, S., Kong, X., Lehnert, M. D., Nesvadba, N., Verma, A., McCracken, H., Arimoto, N., Mignoli, M., & Onodera, M. 2009, *ApJ*, 706, 1364
- Förster Schreiber, N. M., Genzel, R., Lehnert, M. D., Bouché, N., Verma, A., Erb, D. K., Shapley, A. E., Steidel, C. C., Davies, R., Lutz, D., Nesvadba, N., Tacconi, L. J., Eisenhauer, F., Abuter, R., Gilbert, A., Gillessen, S., & Sternberg, A. 2006, *ApJ*, 645, 1062

- Förster Schreiber, N. M., Genzel, R., Lutz, D., Kunze, D., & Sternberg, A. 2001, *ApJ*, 552, 544
- Förster Schreiber, N. M., Genzel, R., Lutz, D., & Sternberg, A. 2003, *ApJ*, 599, 193
- Gabor, J. M. & Davé, R. 2012, ArXiv e-prints
- Gabor, J. M., Davé, R., Finlator, K., & Oppenheimer, B. D. 2010, *MNRAS*, 407, 749
- Gavazzi, R. & Soucaïl, G. 2007, *A&A*, 462, 459
- Genzel, R., Burkert, A., Bouché, N., Cresci, G., Förster Schreiber, N. M., Shapley, A., Shapiro, K., Tacconi, L. J., Buschkamp, P., Cimatti, A., Daddi, E., Davies, R., Eisenhauer, F., Erb, D. K., Genel, S., Gerhard, O., Hicks, E., Lutz, D., Naab, T., Ott, T., Rabien, S., Renzini, A., Steidel, C. C., Sternberg, A., & Lilly, S. J. 2008, *ApJ*, 687, 59
- Genzel, R., Tacconi, L. J., Eisenhauer, F., Förster Schreiber, N. M., Cimatti, A., Daddi, E., Bouché, N., Davies, R., Lehnert, M. D., Lutz, D., Nesvadba, N., Verma, A., Abuter, R., Shapiro, K., Sternberg, A., Renzini, A., Kong, X., Arimoto, N., & Mignoli, M. 2006, *Nature*, 442, 786
- Genzel, R., Tacconi, L. J., Rigopoulou, D., Lutz, D., & Tecza, M. 2001, *ApJ*, 563, 527
- Ghez, A. M., Salim, S., Weinberg, N. N., Lu, J. R., Do, T., Dunn, J. K., Matthews, K., Morris, M. R., Yelda, S., Becklin, E. E., Kremenek, T., Milosavljevic, M., & Naiman, J. 2008, *ApJ*, 689, 1044
- Gillessen, S., Eisenhauer, F., Trippe, S., Alexander, T., Genzel, R., Martins, F., & Ott, T. 2009, *ApJ*, 692, 1075
- Giodini, S., Pierini, D., Finoguenov, A., Pratt, G. W., Boehringer, H., Leauthaud, A., Guzzo, L., Aussel, H., Bolzonella, M., Capak, P., Elvis, M., Hasinger, G., Ilbert, O., Kartaltepe, J. S., Koekemoer, A. M., Lilly, S. J., Massey, R., McCracken, H. J., Rhodes, J., Salvato, M., Sanders, D. B., Scoville, N. Z., Sasaki, S., Smolcic, V., Taniguchi, Y., Thompson, D., & the COSMOS Collaboration. 2009, *ApJ*, 703, 982
- Glasser, G. J. 1962, *Amer. Stat. Assoc.*, 57, 648
- Gonzalez, A. H., Zaritsky, D., & Zabludoff, A. I. 2007, *ApJ*, 666, 147
- Governato, F., Brook, C. B., Brooks, A. M., Mayer, L., Willman, B., Jonsson, P., Stilp, A. M., Pope, L., Christensen, C., Wadsley, J., & Quinn, T. 2009, *MNRAS*, 398, 312
- Graham, A. W., Driver, S. P., Petrosian, V., Conselice, C. J., Bershady, M. A., Crawford, S. M., & Goto, T. 2005, *AJ*, 130, 1535

- Graham, A. W., Trujillo, I., & Caon, N. 2001, *AJ*, 122, 1707
- Guo, Q. & White, S. D. M. 2008, *MNRAS*, 384, 2
- Hamuy, M., Suntzeff, N. B., Heathcote, S. R., Walker, A. R., Gigoux, P., & Phillips, M. M. 1994, *PASP*, 106, 566
- Hamuy, M., Walker, A. R., Suntzeff, N. B., Gigoux, P., Heathcote, S. R., & Phillips, M. M. 1992, *PASP*, 104, 533
- Herter, T. L., Henderson, C. P., Wilson, J. C., Matthews, K. Y., Rahmer, G., Bonati, M., Muirhead, P. S., Adams, J. D., Lloyd, J. P., Skrutskie, M. F., Moon, D.-S., Parshley, S. C., Nelson, M. J., Martinache, F., & Gull, G. E. 2008, in *Society of Photo-Optical Instrumentation Engineers (SPIE) Conference Series*, Vol. 7014, *Society of Photo-Optical Instrumentation Engineers (SPIE) Conference Series*
- Heymans, C., Bell, E. F., Rix, H.-W., Barden, M., Borch, A., Caldwell, J. A. R., McIntosh, D. H., Meisenheimer, K., Peng, C. Y., Wolf, C., Beckwith, S. V. W., Häußler, B., Jahnke, K., Jogee, S., Sánchez, S. F., Somerville, R., & Wisotzki, L. 2006, *MNRAS*, 371, L60
- Hopkins, A. M. & Beacom, J. F. 2006, *ApJ*, 651, 142
- Hopkins, P. F., Bundy, K., Croton, D., Hernquist, L., Keres, D., Khochfar, S., Stewart, K., Wetzel, A., & Younger, J. D. 2010, *ApJ*, 715, 202
- Hopkins, P. F. & Hernquist, L. 2006, *ApJS*, 166, 1
- Hopkins, P. F., Hernquist, L., Cox, T. J., Di Matteo, T., Robertson, B., & Springel, V. 2006a, *ApJS*, 163, 1
- Hopkins, P. F., Somerville, R. S., Hernquist, L., Cox, T. J., Robertson, B., & Li, Y. 2006b, *ApJ*, 652, 864
- Howell, D. A., Sullivan, M., Perrett, K., Bronder, T. J., Hook, I. M., Astier, P., Aubourg, E., Balam, D., Basa, S., Carlberg, R. G., Fabbro, S., Fouchez, D., Guy, J., Lafoux, H., Neill, J. D., Pain, R., Palanque-Delabrouille, N., Pritchet, C. J., Regnault, N., Rich, J., Taillet, R., Knop, R., McMahon, R. G., Perlmutter, S., & Walton, N. A. 2005, *ApJ*, 634, 1190
- Hubble, E. P. 1926, *ApJ*, 64, 321
- . 1936, *Realm of the Nebulae*
- Hughes, T. M. & Cortese, L. 2009, *MNRAS*, 396, L41

- Jogee, S., Miller, S. H., Penner, K., Skelton, R. E., Conselice, C. J., Somerville, R. S., Bell, E. F., Zheng, X. Z., Rix, H., Robaina, A. R., Barazza, F. D., Barden, M., Borch, A., Beckwith, S. V. W., Caldwell, J. A. R., Peng, C. Y., Heymans, C., McIntosh, D. H., Häußler, B., Jahnke, K., Meisenheimer, K., Sanchez, S. F., Wisotzki, L., Wolf, C., & Papovich, C. 2009, *ApJ*, 697, 1971
- Kannappan, S. J., Guie, J. M., & Baker, A. J. 2009, *AJ*, 138, 579
- Karachentsev, I. D., Karachentseva, V. E., Huchtmeier, W. K., & Makarov, D. I. 2004, *AJ*, 127, 2031
- Kartalpepe, J. S., Sanders, D. B., Scoville, N. Z., Calzetti, D., Capak, P., Koekemoer, A., Mobasher, B., Murayama, T., Salvato, M., Sasaki, S. S., & Taniguchi, Y. 2007, *ApJS*, 172, 320
- Kauffmann, G. 1996, *MNRAS*, 281, 487
- Kauffmann, G., Heckman, T. M., White, S. D. M., Charlot, S., Tremonti, C., Brinchmann, J., Bruzual, G., Peng, E. W., Seibert, M., Bernardi, M., Blanton, M., Brinkmann, J., Castander, F., Csábai, I., Fukugita, M., Ivezić, Z., Munn, J. A., Nichol, R. C., Padmanabhan, N., Thakar, A. R., Weinberg, D. H., & York, D. 2003, *MNRAS*, 341, 33
- Kauffmann, G., White, S. D. M., & Guiderdoni, B. 1993, *MNRAS*, 264, 201
- Kennicutt, Jr., R. C., Roettiger, K. A., Keel, W. C., van der Hulst, J. M., & Hummel, E. 1987, *AJ*, 93, 1011
- Kereš, D., Katz, N., Fardal, M., Davé, R., & Weinberg, D. H. 2009, *MNRAS*, 395, 160
- Khochfar, S. & Burkert, A. 2003, *ApJ*, 597, L117
- Khochfar, S. & Silk, J. 2009, *MNRAS*, 397, 506
- Lambas, D. G., Alonso, S., Mesa, V., & O'Mill, A. L. 2012, *A&A*, 539, A45
- Le Borgne, D. & Rocca-Volmerange, B. 2002, *A&A*, 386, 446
- Le Borgne, D., Rocca-Volmerange, B., Prugniel, P., Lançon, A., Fioc, M., & Soubiran, C. 2004, *A&A*, 425, 881
- Le Fèvre, O., Abraham, R., Lilly, S. J., Ellis, R. S., Brinchmann, J., Schade, D., Tresse, L., Colless, M., Crampton, D., Glazebrook, K., Hammer, F., & Broadhurst, T. 2000, *MNRAS*, 311, 565

- Leauthaud, A., Finoguenov, A., Kneib, J.-P., Taylor, J. E., Massey, R., Rhodes, J., Ilbert, O., Bundy, K., Tinker, J., George, M. R., Capak, P., Koekemoer, A. M., Johnston, D. E., Zhang, Y.-Y., Cappelluti, N., Ellis, R. S., Elvis, M., Giodini, S., Heymans, C., Le Fèvre, O., Lilly, S., McCracken, H. J., Mellier, Y., Réfrégier, A., Salvato, M., Scoville, N., Smoot, G., Tanaka, M., Van Waerbeke, L., & Wolk, M. 2010, *ApJ*, 709, 97
- Leauthaud, A., George, M. R., Behroozi, P. S., Bundy, K., Tinker, J., Wechsler, R. H., Conroy, C., Finoguenov, A., & Tanaka, M. 2011, *ArXiv e-prints*
- Lilly, S. J., Le Fevre, O., Hammer, F., & Crampton, D. 1996, *ApJ*, 460, L1
- Lilly, S. J., Le Fèvre, O., Renzini, A., Zamorani, G., Scodreggio, M., Contini, T., Carollo, C. M., Hasinger, G., Kneib, J., Iovino, A., Le Brun, V., Maier, C., Mainieri, V., Mignoli, M., Silverman, J., Tasca, L. A. M., Bolzonella, M., Bongiorno, A., Bottini, D., Capak, P., Caputi, K., Cimatti, A., Cucciati, O., Daddi, E., Feldmann, R., Franzetti, P., Garilli, B., Guzzo, L., Ilbert, O., Kampczyk, P., Kovac, K., Lamareille, F., Leauthaud, A., Borgne, J., McCracken, H. J., Marinoni, C., Pello, R., Ricciardelli, E., Scarlata, C., Vergani, D., Sanders, D. B., Schinnerer, E., Scoville, N., Taniguchi, Y., Arnouts, S., Aussel, H., Bardelli, S., Brusa, M., Cappi, A., Ciliegi, P., Finoguenov, A., Foucaud, S., Franceschini, R., Halliday, C., Impey, C., Knobel, C., Koekemoer, A., Kurk, J., Maccagni, D., Maddox, S., Marano, B., Marconi, G., Meneux, B., Mobasher, B., Moreau, C., Peacock, J. A., Porciani, C., Pozzetti, L., Scaramella, R., Schiminovich, D., Shopbell, P., Smail, I., Thompson, D., Tresse, L., Vettolani, G., Zanichelli, A., & Zucca, E. 2007, *ApJS*, 172, 70
- Lin, L., Koo, D. C., Weiner, B. J., Chiueh, T., Coil, A. L., Lotz, J., Conselice, C. J., Willner, S. P., Smith, H. A., Guhathakurta, P., Huang, J., Le Floch, E., Noeske, K. G., Willmer, C. N. A., Cooper, M. C., & Phillips, A. C. 2007, *ApJ*, 660, L51
- Lin, L., Koo, D. C., Willmer, C. N. A., Patton, D. R., Conselice, C. J., Yan, R., Coil, A. L., Cooper, M. C., Davis, M., Faber, S. M., Gerke, B. F., Guhathakurta, P., & Newman, J. A. 2004a, *ApJ*, 617, L9
- Lin, L., Patton, D. R., Koo, D. C., Casteels, K., Conselice, C. J., Faber, S. M., Lotz, J., Willmer, C. N. A., Hsieh, B. C., Chiueh, T., Newman, J. A., Novak, G. S., Weiner, B. J., & Cooper, M. C. 2008, *ApJ*, 681, 232
- Lin, Y.-T., Mohr, J. J., & Stanford, S. A. 2004b, *ApJ*, 610, 745
- Liske, J., Lemon, D. J., Driver, S. P., Cross, N. J. G., & Couch, W. J. 2003, *MNRAS*, 344, 307

- López-Sanjuan, C., Balcells, M., García-Dabó, C. E., Prieto, M., Cristóbal-Hornillos, D., Eliche-Moral, M. C., Abreu, D., Erwin, P., & Guzmán, R. 2009, *ApJ*, 694, 643
- López-Sanjuan, C., Balcells, M., Pérez-González, P. G., Barro, G., Gallego, J., & Zamorano, J. 2010, *A&A*, 518, A20
- Lorenz, M. O. 1905, *Amer. Stat. Assoc.*, 9, 209
- Lotz, J. M., Davis, M., Faber, S. M., Guhathakurta, P., Gwyn, S., Huang, J., Koo, D. C., Le Floch, E., Lin, L., Newman, J., Noeske, K., Papovich, C., Willmer, C. N. A., Coil, A., Conselice, C. J., Cooper, M., Hopkins, A. M., Metevier, A., Primack, J., Rieke, G., & Weiner, B. J. 2008a, *ApJ*, 672, 177
- Lotz, J. M., Jonsson, P., Cox, T. J., & Primack, J. R. 2008b, *MNRAS*, 391, 1137
- . 2009a, ArXiv e-prints
- . 2009b, ArXiv e-prints
- . 2010a, *MNRAS*, 404, 590
- . 2010b, *MNRAS*, 404, 575
- Lotz, J. M., Primack, J., & Madau, P. 2004, *AJ*, 128, 163
- Luhman, K. L., Engelbracht, C. W., & Luhman, M. L. 1998, *ApJ*, 499, 799
- Madau, P., Pozzetti, L., & Dickinson, M. 1998, *ApJ*, 498, 106
- Magnier, E. A. & Cuillandre, J. 2004, *PASP*, 116, 449
- Mandelbaum, R., Seljak, U., Kauffmann, G., Hirata, C. M., & Brinkmann, J. 2006, *MNRAS*, 368, 715
- Martin, D. C., Wyder, T. K., Schiminovich, D., Barlow, T. A., Forster, K., Friedman, P. G., Morrissey, P., Neff, S. G., Seibert, M., Small, T., Welsh, B. Y., Bianchi, L., Donas, J., Heckman, T. M., Lee, Y.-W., Madore, B. F., Milliard, B., Rich, R. M., Szalay, A. S., & Yi, S. K. 2007, *ApJS*, 173, 342
- Martini, P., Persson, S. E., Murphy, D. C., Birk, C., Shectman, S. A., Gunnels, S. M., & Koch, E. 2004, in *Society of Photo-Optical Instrumentation Engineers (SPIE) Conference Series*, Vol. 5492, *Society of Photo-Optical Instrumentation Engineers (SPIE) Conference Series*, ed. A. F. M. Moorwood & M. Iye, 1653–1660

- Mihos, J. C. & Hernquist, L. 1994, *ApJ*, 431, L9
- Miner, J., Rose, J. A., & Cecil, G. 2011, *ApJ*, 727, L15
- Moon, D., Koo, B., Lee, H., Matthews, K., Lee, J., Pyo, T., Seok, J. Y., & Hayashi, M. 2009, *ApJL*, 703, L81
- Morgan, W. W. 1971, *AJ*, 76, 1000
- Morgan, W. W. 1972, in *IAU Symposium, Vol. 44, External Galaxies and Quasi-Stellar Objects*, ed. D. S. Evans, D. Wills, & B. J. Wills, 97
- Nair, P. B. & Abraham, R. G. 2010, *ApJS*, 186, 427
- Neistein, E. & Dekel, A. 2008, *MNRAS*, 388, 1792
- Olsen, L. F., Benoist, C., Cappi, A., Maurogordato, S., Mazure, A., Slezak, E., Adami, C., Ferrari, C., & Martel, F. 2007, *A&A*, 461, 81
- Overzier, R. A., Heckman, T. M., Kauffmann, G., Seibert, M., Rich, R. M., Basu-Zych, A., Lotz, J., Aloisi, A., Charlot, S., Hoopes, C., Martin, D. C., Schiminovich, D., & Madore, B. 2008, *ApJ*, 677, 37
- Panuzzo, P., Rampazzo, R., Bressan, A., Vega, O., Annibali, F., Buson, L. M., Clemens, M. S., & Zeilinger, W. W. 2011, *A&A*, 528, A10
- Patton, D. R., Carlberg, R. G., Marzke, R. O., Pritchett, C. J., da Costa, L. N., & Pellegrini, P. S. 2000, *ApJ*, 536, 153
- Patton, D. R., Pritchett, C. J., Carlberg, R. G., Marzke, R. O., Yee, H. K. C., Hall, P. B., Lin, H., Morris, S. L., Sawicki, M., Shepherd, C. W., & Wirth, G. D. 2002, *ApJ*, 565, 208
- Pozzetti, L., Bolzonella, M., Zucca, E., Zamorani, G., Lilly, S., Renzini, A., Moresco, M., Mignoli, M., Cassata, P., Tasca, L., Lamareille, F., Maier, C., Meneux, B., Halliday, C., Oesch, P., Vergani, D., Caputi, K., Kovač, K., Cimatti, A., Cucciati, O., Iovino, A., Peng, Y., Carollo, M., Contini, T., Kneib, J.-P., Le Fèvre, O., Mainieri, V., Scodreggio, M., Bardelli, S., Bongiorno, A., Coppa, G., de la Torre, S., de Ravel, L., Franzetti, P., Garilli, B., Kampczyk, P., Knobel, C., Le Borgne, J.-F., Le Brun, V., Pellò, R., Perez Montero, E., Ricciardelli, E., Silverman, J. D., Tanaka, M., Tresse, L., Abbas, U., Bottini, D., Cappi, A., Guzzo, L., Koekemoer, A. M., Leauthaud, A., Maccagni, D., Marinoni, C., McCracken, H. J., Memeo, P., Porciani, C., Scaramella, R., Scarlata, C., & Scoville, N. 2010, *A&A*, 523, A13+

- Rampazzo, R., Annibali, F., Bressan, A., Longhetti, M., Padoan, F., & Zeilinger, W. W. 2005, *A&A*, 433, 497
- Reid, M. J. 1993, *ARA&A*, 31, 345
- Rix, H., Barden, M., Beckwith, S. V. W., Bell, E. F., Borch, A., Caldwell, J. A. R., Häussler, B., Jahnke, K., Jogee, S., McIntosh, D. H., Meisenheimer, K., Peng, C. Y., Sanchez, S. F., Somerville, R. S., Wisotzki, L., & Wolf, C. 2004, *ApJS*, 152, 163
- Robertson, B. E. & Bullock, J. S. 2008, *ApJ*, 685, L27
- Robitaille, T. P. & Whitney, B. A. 2010, *ApJ*, 710, L11
- Rodríguez Zaurín, J., Tadhunter, C. N., & Delgado, R. M. G. 2010, *MNRAS*, 310
- Rubin, V. C., Burstein, D., Ford, Jr., W. K., & Thonnard, N. 1985, *ApJ*, 289, 81
- Sanders, D. B. & Mirabel, I. F. 1996, *ARA&A*, 34, 749
- Sanders, D. B., Soifer, B. T., Elias, J. H., Madore, B. F., Matthews, K., Neugebauer, G., & Scoville, N. Z. 1988, *ApJ*, 325, 74
- Scarlata, C., Carollo, C. M., Lilly, S. J., Feldmann, R., Kampczyk, P., Renzini, A., Cimatti, A., Halliday, C., Daddi, E., Sargent, M. T., Koekemoer, A., Scoville, N., Kneib, J., Leauthaud, A., Massey, R., Rhodes, J., Tasca, L., Capak, P., McCracken, H. J., Mobasher, B., Taniguchi, Y., Thompson, D., Ajiki, M., Aussel, H., Murayama, T., Sanders, D. B., Sasaki, S., Shioya, Y., & Takahashi, M. 2007, *ApJS*, 172, 494
- Schmidt, M. 1968, *ApJ*, 151, 393
- Schweizer, F. 1982, *ApJ*, 252, 455
- Scoville, N., Aussel, H., Brusa, M., Capak, P., Carollo, C. M., Elvis, M., Giavalisco, M., Guzzo, L., Hasinger, G., Impey, C., Kneib, J., LeFevre, O., Lilly, S. J., Mobasher, B., Renzini, A., Rich, R. M., Sanders, D. B., Schinnerer, E., Schminovich, D., Shopbell, P., Taniguchi, Y., & Tyson, N. D. 2007, *ApJS*, 172, 1
- Semboloni, E., Mellier, Y., van Waerbeke, L., Hoekstra, H., Tereno, I., Benabed, K., Gwyn, S. D. J., Fu, L., Hudson, M. J., Maoli, R., & Parker, L. C. 2006, *A&A*, 452, 51
- Shapiro, K. L., Falcón-Barroso, J., van de Ven, G., de Zeeuw, P. T., Sarzi, M., Bacon, R., Bolatto, A., Cappellari, M., Croton, D., Davies, R. L., Emsellem, E., Fakhouri, O., Krajnović, D., Kuntschner, H., McDermid, R. M., Peletier, R. F., van den Bosch, R. C. E., & van der Wolk, G. 2010, *MNRAS*, 402, 2140

- Sharples, R. M., Bender, R., Lehnert, M. D., Ramsay Howat, S. K., Bremer, M. N., Davies, R. L., Genzel, R., Hofmann, R., Ivison, R. J., Saglia, R., & Thatte, N. A. 2004, in Society of Photo-Optical Instrumentation Engineers (SPIE) Conference Series, Vol. 5492, Society of Photo-Optical Instrumentation Engineers (SPIE) Conference Series, ed. A. F. M. Moorwood & M. Iye, 1179–1186
- Sivanandam, S., Chou, R. C. Y., Moon, D.-S., Ma, K., Millar-Blanchaer, M., Eikenberry, S. S., Chun, M.-Y., Kim, S. C., Raines, S. N., & Eisner, J. 2012, ArXiv e-prints
- Somerville, R. S., Primack, J. R., & Faber, S. M. 2001, MNRAS, 320, 504
- Spitler, L. R., Forbes, D. A., Strader, J., Brodie, J. P., & Gallagher, J. S. 2008, MNRAS, 385, 361
- Springel, V., Di Matteo, T., & Hernquist, L. 2005, ApJ, 620, L79
- Stark, D. P., Swinbank, A. M., Ellis, R. S., Dye, S., Smail, I. R., & Richard, J. 2008, Nature, 455, 775
- Stewart, K. R., Bullock, J. S., Wechsler, R. H., Maller, A. H., & Zentner, A. R. 2008, ApJ, 683, 597
- Stoughton, C., Lupton, R. H., Bernardi, M., Blanton, M. R., Burles, S., Castander, F. J., Connolly, A. J., Eisenstein, D. J., Frieman, J. A., Hennessy, G. S., Hindsley, R. B., Ivezić, Ž., Kent, S., Kunszt, P. Z., Lee, B. C., Meiksin, A., Munn, J. A., Newberg, H. J., Nichol, R. C., Nicinski, T., Pier, J. R., Richards, G. T., Richmond, M. W., Schlegel, D. J., Smith, J. A., Strauss, M. A., SubbaRao, M., Szalay, A. S., Thakar, A. R., Tucker, D. L., Vanden Berk, D. E., Yanny, B., Adelman, J. K., Anderson, Jr., J. E., Anderson, S. F., Annis, J., Bahcall, N. A., Bakken, J. A., Bartelmann, M., Bastian, S., Bauer, A., Berman, E., Böhringer, H., Boroski, W. N., Bracker, S., Briegel, C., Briggs, J. W., Brinkmann, J., Brunner, R., Carey, L., Carr, M. A., Chen, B., Christian, D., Colestock, P. L., Crocker, J. H., Csabai, I., Czarapata, P. C., Dalcanton, J., Davidsen, A. F., Davis, J. E., Dehnen, W., Dodelson, S., Doi, M., Dombeck, T., Donahue, M., Ellman, N., Elms, B. R., Evans, M. L., Eyer, L., Fan, X., Federwitz, G. R., Friedman, S., Fukugita, M., Gal, R., Gillespie, B., Glazebrook, K., Gray, J., Grebel, E. K., Greenawalt, B., Greene, G., Gunn, J. E., de Haas, E., Haiman, Z., Haldeman, M., Hall, P. B., Hamabe, M., Hansen, B., Harris, F. H., Harris, H., Harvanek, M., Hawley, S. L., Hayes, J. J. E., Heckman, T. M., Helmi, A., Henden, A., Hogan, C. J., Hogg, D. W., Holmgren, D. J., Holtzman, J., Huang, C., Hull, C., Ichikawa, S., Ichikawa, T., Johnston, D. E., Kauffmann, G., Kim, R. S. J., Kimball, T., Kinney, E., Klaene, M., Kleinman, S. J., Klypin, A., Knapp, G. R., Korienek, J., Krolik, J., Kron, R. G., Krzesiński,

- J., Lamb, D. Q., Leger, R. F., Limmongkol, S., Lindenmeyer, C., Long, D. C., Loomis, C., Loveday, J., MacKinnon, B., Mannery, E. J., Mantsch, P. M., Margon, B., McGehee, P., McKay, T. A., McLean, B., Menou, K., Merelli, A., Mo, H. J., Monet, D. G., Nakamura, O., Narayanan, V. K., Nash, T., Neilsen, Jr., E. H., Newman, P. R., Nitta, A., Odenkirchen, M., Okada, N., Okamura, S., Ostriker, J. P., Owen, R., Pauls, A. G., Peoples, J., Peterson, R. S., Petravick, D., Pope, A., Pordes, R., Postman, M., Prosapio, A., Quinn, T. R., Rechenmacher, R., Rivetta, C. H., Rix, H., Rockosi, C. M., Rosner, R., Ruthmansdorfer, K., Sandford, D., Schneider, D. P., Scranton, R., Sekiguchi, M., Sergey, G., Sheth, R., Shimasaku, K., Smee, S., Snedden, S. A., Stebbins, A., Stubbs, C., Szapudi, I., Szkody, P., Szokoly, G. P., Tabachnik, S., Tsvetanov, Z., Uomoto, A., Vogeley, M. S., Voges, W., Waddell, P., Walterbos, R., Wang, S., Watanabe, M., Weinberg, D. H., White, R. L., White, S. D. M., Wilhite, B., Wolfe, D., Yasuda, N., York, D. G., Zehavi, I., & Zheng, W. 2002, *AJ*, 123, 485
- Strateva, I., Ivezić, Ž., Knapp, G. R., Narayanan, V. K., Strauss, M. A., Gunn, J. E., Lupton, R. H., Schlegel, D., Bahcall, N. A., Brinkmann, J., Brunner, R. J., Budavári, T., Csabai, I., Castander, F. J., Doi, M., Fukugita, M., Győry, Z., Hamabe, M., Hennessy, G., Ichikawa, T., Kunszt, P. Z., Lamb, D. Q., McKay, T. A., Okamura, S., Racusin, J., Sekiguchi, M., Schneider, D. P., Shimasaku, K., & York, D. 2001, *AJ*, 122, 1861
- Sullivan, M., Howell, D. A., Perrett, K., Nugent, P. E., Astier, P., Aubourg, E., Balam, D., Basa, S., Carlberg, R. G., Conley, A., Fabbro, S., Fouchez, D., Guy, J., Hook, I., Lafoux, H., Neill, J. D., Pain, R., Palanque-Delabrouille, N., Pritchett, C. J., Regnault, N., Rich, J., Taillet, R., Aldering, G., Baumont, S., Bronder, J., Filiol, M., Knop, R. A., Perlmutter, S., & Tao, C. 2006a, *AJ*, 131, 960
- Sullivan, M., Le Borgne, D., Pritchett, C. J., Hodsmann, A., Neill, J. D., Howell, D. A., Carlberg, R. G., Astier, P., Aubourg, E., Balam, D., Basa, S., Conley, A., Fabbro, S., Fouchez, D., Guy, J., Hook, I., Pain, R., Palanque-Delabrouille, N., Perrett, K., Regnault, N., Rich, J., Taillet, R., Baumont, S., Bronder, J., Ellis, R. S., Filiol, M., Luset, V., Perlmutter, S., Ripoche, P., & Tao, C. 2006b, *ApJ*, 648, 868
- Tinsley, B. M. & Larson, D. Campbell, R. B. G., eds. 1977, *Evolution of galaxies and stellar populations*
- Toomre, A. 1977, in *Evolution of Galaxies and Stellar Populations*, ed. B. M. Tinsley & R. B. Larson, 401–+
- Toomre, A. & Toomre, J. 1972, *ApJ*, 178, 623
- Totani, T. & Yoshii, Y. 1998, *ApJ*, 501, L177+

- Tully, R. B. & Fisher, J. R. 1977, *A&A*, 54, 661
- Tully, R. B., Mould, J. R., & Aaronson, M. 1982, *ApJ*, 257, 527
- van den Bergh, S. 1999, *A&A Rev.*, 9, 273
- van Dokkum, P. & Conroy, C. 2012, ArXiv e-prints
- van Dokkum, P. G. 2005, *AJ*, 130, 2647
- van Dokkum, P. G., Franx, M., Fabricant, D., Illingworth, G. D., & Kelson, D. D. 2000, *ApJ*, 541, 95
- Visvanathan, N. 1981, *A&A*, 100, L20
- Visvanathan, N. & Griensmith, D. 1977, *A&A*, 59, 317
- Williams, D. M., Thompson, C. L., Rieke, G. H., & Montgomery, E. F. 1993, in *Society of Photo-Optical Instrumentation Engineers (SPIE) Conference Series*, Vol. 1946, *Society of Photo-Optical Instrumentation Engineers (SPIE) Conference Series*, ed. A. M. Fowler, 482–489
- Williams, R. E., Blacker, B., Dickinson, M., Dixon, W. V. D., Ferguson, H. C., Fruchter, A. S., Giavalisco, M., Gilliland, R. L., Heyer, I., Katsanis, R., Levay, Z., Lucas, R. A., McElroy, D. B., Petro, L., Postman, M., Adorf, H.-M., & Hook, R. 1996, *AJ*, 112, 1335
- Willmer, C. N. A., Faber, S. M., Koo, D. C., Weiner, B. J., Newman, J. A., Coil, A. L., Connolly, A. J., Conroy, C., Cooper, M. C., Davis, M., Finkbeiner, D. P., Gerke, B. F., Guhathakurta, P., Harker, J., Kaiser, N., Kassin, S., Konidaris, N. P., Lin, L., Luppino, G., Madgwick, D. S., Noeske, K. G., Phillips, A. C., & Yan, R. 2006, *ApJ*, 647, 853
- Wirth, G. D., Willmer, C. N. A., Amico, P., Chaffee, F. H., Goodrich, R. W., Kwok, S., Lyke, J. E., Mader, J. A., Tran, H. D., Barger, A. J., Cowie, L. L., Capak, P., Coil, A. L., Cooper, M. C., Conrad, A., Davis, M., Faber, S. M., Hu, E. M., Koo, D. C., Le Mignant, D., Newman, J. A., & Songaila, A. 2004, *AJ*, 127, 3121
- Wolf, C., Bell, E. F., McIntosh, D. H., Rix, H.-W., Barden, M., Beckwith, S. V. W., Borch, A., Caldwell, J. A. R., Häussler, B., Heymans, C., Jahnke, K., Jogee, S., Meisenheimer, K., Peng, C. Y., Sánchez, S. F., Somerville, R. S., & Wisotzki, L. 2005, *ApJ*, 630, 771
- Wolf, C., Meisenheimer, K., Kleinheinrich, M., Borch, A., Dye, S., Gray, M., Wisotzki, L., Bell, E. F., Rix, H., Cimatti, A., Hasinger, G., & Szokoly, G. 2004, *A&A*, 421, 913

Xu, C. & Sulentic, J. W. 1991, *ApJ*, 374, 407

Xu, C. K., Sun, Y. C., & He, X. T. 2004, *ApJ*, 603, L73

Yee, H. K. C., Morris, S. L., Lin, H., Carlberg, R. G., Hall, P. B., Sawicki, M., Patton, D. R., Wirth, G. D., Ellingson, E., & Shepherd, C. W. 2000, *ApJS*, 129, 475

York, D. G., Adelman, J., Anderson, Jr., J. E., Anderson, S. F., Annis, J., Bahcall, N. A., Bakken, J. A., Barkhouser, R., Bastian, S., Berman, E., Boroski, W. N., Bracker, S., Briegel, C., Briggs, J. W., Brinkmann, J., Brunner, R., Burles, S., Carey, L., Carr, M. A., Castander, F. J., Chen, B., Colestock, P. L., Connolly, A. J., Crocker, J. H., Csabai, I., Czarapata, P. C., Davis, J. E., Doi, M., Dombeck, T., Eisenstein, D., Ellman, N., Elms, B. R., Evans, M. L., Fan, X., Federwitz, G. R., Fiscelli, L., Friedman, S., Frieman, J. A., Fukugita, M., Gillespie, B., Gunn, J. E., Gurbani, V. K., de Haas, E., Haldeman, M., Harris, F. H., Hayes, J., Heckman, T. M., Hennessy, G. S., Hindsley, R. B., Holm, S., Holmgren, D. J., Huang, C.-h., Hull, C., Husby, D., Ichikawa, S.-I., Ichikawa, T., Ivezić, Ž., Kent, S., Kim, R. S. J., Kinney, E., Klaene, M., Kleinman, A. N., Kleinman, S., Knapp, G. R., Korienek, J., Kron, R. G., Kunszt, P. Z., Lamb, D. Q., Lee, B., Leger, R. F., Limmongkol, S., Lindenmeyer, C., Long, D. C., Loomis, C., Loveday, J., Lucinio, R., Lupton, R. H., MacKinnon, B., Mannery, E. J., Mantsch, P. M., Margon, B., McGehee, P., McKay, T. A., Meiksin, A., Merelli, A., Monet, D. G., Munn, J. A., Narayanan, V. K., Nash, T., Neilsen, E., Neswold, R., Newberg, H. J., Nichol, R. C., Nicinski, T., Nonino, M., Okada, N., Okamura, S., Ostriker, J. P., Owen, R., Pauls, A. G., Peoples, J., Peterson, R. L., Petravick, D., Pier, J. R., Pope, A., Pordes, R., Prosapio, A., Rechenmacher, R., Quinn, T. R., Richards, G. T., Richmond, M. W., Rivetta, C. H., Rockosi, C. M., Ruthmansdorfer, K., Sandford, D., Schlegel, D. J., Schneider, D. P., Sekiguchi, M., Sergey, G., Shimasaku, K., Siegmund, W. A., Smee, S., Smith, J. A., Snedden, S., Stone, R., Stoughton, C., Strauss, M. A., Stubbs, C., SubbaRao, M., Szalay, A. S., Szapudi, I., Szokoly, G. P., Thakar, A. R., Tremonti, C., Tucker, D. L., Uomoto, A., Vanden Berk, D., Vogeley, M. S., Waddell, P., Wang, S.-i., Watanabe, M., Weinberg, D. H., Yanny, B., Yasuda, N., & SDSS Collaboration. 2000, *AJ*, 120, 1579